Correlated p-N Pairs from ^{4}He Photodisintegration with Tagged Photons from 80 to 131 MeV

by

Sean Michael Doran

Presented as a Thesis for the Degree of

Doctor of Philosophy

to the University of Glasgow,

September 1992.

ProQuest LLC.
789 East Eisenhower Parkway
P.O. Box 1346
Ann Arbor, MI 48106 – 1346

Abstract

Results are presented for measurements of the photodisintegation of ^{4}He using tagged photons in the energy range 80-131 MeV. In this energy region, the dominant photon absorption process is thought to be the quasideuteron mechanism of Levinger[1]. The data are compared with the predictions of this model and with phase space calculations. Considerable agreement with the quasi-deuteron model is demonstrated. Two detector arrays were used in this measurement, one for the detection and identification of protons, and the other for the detection and identification of protons and neutrons. This allows separation of the ^{4}He (γ,pn) events from ^{4}He (γ,pp) events. Furthermore, the energy resolution is sufficiently good to enable separation of the ^{4}He (γ,pn)d and ^{4}He (γ,pn)pn decay channels, on the basis of their differing missing energies.

The experiment, at the 180 MeV CW electron microtron MAMI-A [2], was performed using the Glasgow tagged photon spectrometer [3] at the University of Mainz Institut für Kernphysik. Protons were detected in a large solid angle (0.9 sr) position sensitive plastic scintillator telescope [4], having an energy resolution of 5% and an angular resolution of 3°. The correlated neutrons were detected on the opposite side of the target by a time-of-flight array of 24 scintillator detectors [5] placed 3 metres from the target with an energy resolution of 6 MeV, each subtending an angle of 4°. The vertical angular resolution was 0.6°. A cryogenic liquid helium target was used, with a thickness of 2.573×10^{24} nuclei/cm^2. No previous measurement has been carried out with such good photon energy resolution.

Cross-sections are presented for the (γ,pn)d and (γ,pn)pn channels. The general features of the data are a high σ[^{4}He (γ,pn)d] / σ[^{4}He (γ,pn)pn] cross-section ratio, and a significant degree of angular correlation of the p-n pair in the (γ,pn)

channel. The recoil momentum distribution is also examined, as this is sensitive to the photon reaction mechanism. The missing energy and recoil momentum spectra give good agreement with predictions from the quasi-deuteron model for the (γ,pn)d case. In the (γ,pp) case, missing energy and recoil momentum have also been investigated, however the distributions from this reaction are not in agreement with the quasideuteron model.

Declaration

The data presented was obtained through a collaboration between the nuclear structure groups at Glasgow, Edinburgh and Mainz Universities, in which I played a major rôle. I took part in the development and testing of the cryogenic targets, in preparation for the helium photo-disintegration experiments. The analysis of experimental data is all my own work. This thesis is my own composition.

Sean Michael Doran

Acknowledgements

I would like to thank Dr. Douglas MacGregor, my supervisor, for his help and encouragement during the experiment and data analysis and for his many helpful comments in the course of writing this thesis.

I am indebted to Prof. R. Owens, the director of the Kelvin Laboratory, for his help and guidance, particularly in the interpretation of the data, and for affording me the use of the Kelvin Laboratory facilities.

I owe my thanks to Profs. H. Ehrenberg and B. Schoch at the University of Mainz, who afforded me the use of the accelerator facilities. Professor Schoch also helped in the running of the experiment.

I would like to thank J. Kellie, S. Hall, G. I. Crawford and J. Annand without whom this experiment would not have taken place. J. Kellie and S. Hall put much effort into the preparation of the target.

I would like to thank H. Schmieden, S. Klein, R. Beck, R. Gothe and J. Vogt who made themselves available in the event of technical hitches during the run. H. Schmieden also worked on the target, both before and during the experiment.

I would like to thank I. Anthony and A. Sibbald for their willingness to help when I encountered problems with the computer. I wish also to thank C. McGeorge for his valuable help and advice both during the experiment and in the writing of this

thesis. I thank also E. Taylor for the careful preparation of diagrams for my thesis, and to the technical staff at the Kelvin Lab for their work in producing the detector systems and targets.

I would like to thank the S.E.R.C. for their financial support and Profs. R. Ferrier and I. Hughes, and the I.O.P. for providing funding to attend the summer schools.

My warm thanks to G. Miller, S. Dancer, S. Salem, P. Wallace, V. Holliday, G. Cross, R. Crawford, B. Oussena, A. Ghazarian, P. Harty and D. Sinclair for their humour and moral support.

Finally I give my thanks to my parents, John and Isobel, and to Catriona for their encouragement and moral support in the preparation of this thesis.

Contents

Chapter 1

Introduction

1.1 The Nucleus

One of the principal objectives of nuclear physics is to understand the structure and the dynamics of complex systems comprising of strongly interacting hadrons. The study of such systems has led to a picture of nuclei being composed of nucleons, and mesons which are exchanged between them. The mesons, being massive particles, constitute a force of finite range, which is of the order of a few fm. This mesonic force between baryons is known to be attractive at average internucleon distances, but strongly repulsive for distances of less than $\sim$0.5 fm. At relatively large distances, the interaction between nucleons is normally best described by the exchange of a single virtual pion. This virtual meson may transfer both quantum numbers and momentum between nucleons and may lead to the formation of (virtual) Δ-resonances. At smaller separations, on the other hand, the strong force is less well understood, but to a remarkably good approximation the interaction between p-n pairs at short range appears to be similar to the force between the nucleons within a deuteron.

At short internucleon distances, the basic hadronic structure is thought to come into play, therefore it is more natural to think of nucleon-nucleon interactions as

interactions between their six constituent quarks. Indeed there is tentative evidence of long-lived resonant six quark structures called *dibaryon resonances.* However the theoretical justification for such narrow structures is lacking and the interaction of nucleons at short distances is one of the least understood areas in the whole of nuclear physics.

The nucleus, being in general a many body system, does not readily lend itself to simple exact descriptions. The current state of nuclear theory therefore requires model descriptions which are inherently inexact, where the optimum model for description depends largely upon the nuclear reaction and on the nucleus under study. I shall now describe one such model which has had some degree of success in the field of photonuclear reactions, with which the present work is concerned.

The Quasi-Deuteron Description

The simplest stable configuration of nucleons is the deuteron. This structure is the easiest to understand fully because it is within this nucleus that the mutual interaction between two baryons alone may be studied in isolation from any other strongly interacting bodies. The deuteron system is studied experimentally, and the results compared with those on heavier nuclei in order to learn how the N-N force is altered by surrounding nucleons.

A first step to understanding heavier nuclei might be obtained by extending the N-N force in the deuteron to act between all possible N-N pairs in the nucleus, where it is assumed that the force between an N-N pair is in essence unaltered by the presence of other nucleons. The quasi-deuteron (QD) model of photon absorption assumes that the photon is absorbed on p-n pairs which are in mutual proximity. It is assumed that the force between the proton and the neutron is in essence similar

to the force in the real deuteron. The surrounding nucleons mainly serve to do no more than enhance the overall interaction cross-section.

At a more fundamental level, photonuclear reactions at intermediate photon energies are thought to be sensitive to the details of the short range correlations, which the quasideuteron model attempts to account for in this semi-phenomenological way by relating the photon absorption cross-section to the cross-section for the photodisintegration of deuterium. Quasi-deuteron models constructed in this way have been reasonably successful in explaining electronuclear, photonuclear and pion-nuclear reaction cross-sections.

The success of the quasideuteron picture is somewhat surprising given that a quasideuteron inside a nucleus is by no means an isolated system and may have interactions with other nucleons. For instance, the quasideuterons consist of nucleons of different quantum numbers, and each nucleon-nucleon pair must separately observe the Pauli exclusion principle. The nucleons follow shell model "orbits" determined by the nucleon quantum numbers and it is only where the nucleons are in mutual proximity that quasideuteron interactions are likely to take place. The deuterium nucleus itself has a low density compared to other light nuclei, a factor which leads to an enhancement of the quasideuteron cross-section in heavier nuclei when compared with the cross-section of the real deuteron.

Another way in which the N-N interaction differs from that in deuterium is that three-nucleon interactions are possible, where three nucleons are in relative proximity. Such three-nucleon contributions to experimental cross-sections cannot be described by a quasideuteron mechanism and would require quasi-^{3}He or quasi-^{3}H models. The magnitudes of some of the effects due to 3-body forces have been estimated in reference [6]. The magnitude of these effects may be observed by

looking at reactions under kinematic conditions where the effects of the 2-body force are suppressed. One such reaction is the ^{3}He (γ,pp)n reaction, which is discussed in detail in reference [7].

For photonuclear reactions at intermediate energies, the quasideuteron model seems to be the most successful way of describing the photon interaction within nuclei for $A > 4$. It remains to be seen if such a description is appropriate for ^{4}He, and it is hoped that the present measurement will help to clarify this.

The remainder of this chapter will be devoted to a general overview of existing experimental and theoretical work. In chapter 2 I shall develop the theoretical aspects of this work in more detail. Chapter 3 contains a description of the apparatus which was used during the measurement. Chapter 4 discusses the analysis of the experimental data which was obtained, and chapter 5 presents the experimental results. Finally chapter 6 contains pertinent comments and concluding remarks on the results.

1.2 Nuclear Probes

In experimental physics, the internal structure of the nucleus may be examined using either high energy hadronic probes or electromagnetic probes. Both of these are limited in the aspects of the nucleus which they can be used to explore.

A strongly interacting probe, such as a proton or a pion, has a short mean free path in the target nucleus. Reactions with strong probes therefore have high cross-sections but are only useful in exploring the surface of the nucleus. Being a strong interaction, the resultant perturbation suffered by the nucleus is large, therefore little information about the initial nuclear state may be derived. In addition,

the information which is derived is limited by the fact that the interaction at the fundamental level is not fully understood.

In contrast, the fundamental electromagnetic interaction is well understood, allowing a theoretical understanding of the reaction under study. Electrons and photons interact with a much lower coupling strength than strongly interacting probes, so that the perturbation to the nucleus is small. This allows one to probe the complete volume of the nucleus, in its ground state, thereby obtaining information on the distribution of currents and charges within the nucleus and allowing parameters such as rms charge radii to be evaluated. The nuclear charges are carried both by baryons, such as protons and virtual delta resonances, and by virtual exchange mesons. The electron interacts with charges and currents through virtual photons, which have both transverse and longitudinal components and in an electron beam experiment the effects of these two components may be observed separately through the use of a Rosenbluth separation.

Real photons, on the other hand, possess only a transverse component and due to their zero rest mass impart to the nucleus a substantial quantity of energy accompanied by relatively little momentum. This latter property renders the photon especially sensitive to certain aspects of the nuclear wavefunction as described below: If a photon is to be completely absorbed by a nucleon, the nucleon must have either a high initial momentum or the photon's energy and momentum must be shared between more than one nucleon. The former situation, discussed in section 2.1, is thought to be observed in the (γ,p) reaction for relatively high mismatch momenta between the incoming photon and the ejected proton. In the latter situation, the photon interacts either directly or indirectly with a charged exchange meson, and often leads to the ejection of correlated N-N pairs. Both of these properties will be

discussed in chapter 2.

However, the photon has two distinct disadvantages as a probe:-

1. It has previously proved difficult to produce photon beams of known energy and intensity.

2. Photonuclear cross-sections are generally low, requiring long measurement times to give reasonable statistical accuracy.

The first of these disadvantages is overcome in the present experiment by using a technique called photon tagging. This technique offers high photon energy resolution combined with good cross-section normalisation. For photon flux measurements, the photon tagging method is self-normalising, requiring only an overall correction for the efficiency with which photons can be tagged. The experiment will enable observation of the dependence of reaction cross-sections for each channel, on the photon energy, where the photon energy is determined to a previously unequalled precision.

Tagged photon experiments do however have some difficulties. Coincidence experiments are generally very susceptible to background radiation. The beam intensity is limited by the rate at which the apparatus is capable of detecting and momentum analysing individual photons and the ratio of real to random coincidences must be kept to within acceptable bounds. The tagged photon beam intensity must be weak, in this case, less than 3×10^7 photons per second. This, coupled with the fact that photonuclear cross-sections are generally low, implies that experiments of this nature require a considerable quantity of beam time. It is necessary to have a beam duty-cycle close to 100% in order to produce a feasible experiment with a low random coincidence rate. It is only recently that it has become possible to produce

such high duty-factor electron beams.

1.3 The ^{4}He Nucleus

^{4}He has an extremely high density compared with other light nuclei. It has a charge rms radius [8], r, of 1.68 fm, which is considerably smaller than that of the ^{2}H nucleus, of 2.10 fm. For a spherical nucleus of nucleon number A, the nucleon matter density, ρ, is given by

$$\rho \sim \frac{A}{\frac{4}{3}\pi r^3}$$

The nucleon density for ^{4}He is therefore 0.20 nucleons/fm^3. The fact that ^{4}He is of such high density indicates that nucleonic correlations are likely to be very important. A 100 MeV photon interacting with such a correlated nucleon cluster would be most likely to share its energy between the nucleons concerned, giving little energy to the remaining spectator nucleon(s). It is therefore possible, by observing how many nucleons are released with substantial energy, to deduce whether a 2-N or 3-N correlation is involved. Both types of correlations are likely to contribute significantly to the photonuclear cross-section, as ^{4}He has four distinct p-n pairs, and four distinct sets of 3 nucleons. A 2-N correlation would be expected to lead to two nucleons of high kinetic energy and two nucleons of lower kinetic energy. The two non-participating nucleons would be expected to retain their initial Fermi momentum, and the trajectories of the participating nucleons would be in roughly opposite directions. For the case of a 3-nucleon correlation, no such correlation in direction would be expected and such 3-N correlations would probably be characterised by high double arm missing energies, described in appendix A.2. Therefore by examining the directions and energies of the ejected nuclei, the relative contributions due to both types of correlations may be deduced.

Due to the weak coupling of the photon, initial state interactions can be neglected in photonuclear reactions, however the effects of final state interactions (FSI) should be considered. FSI can have an effect on the energies, distributions and numbers of decay particles. They are also important for heavy nuclei, where absorption of outgoing nucleons and the slight 'refraction' of nucleons as they leave the nuclear 'surface' (thereby partly washing out angular correlations) both have an effect on the results. The treatment of both of these phenomena are discussed in Gottfried's paper [9].

The two effects mentioned, however, are not likely to be important in very light nuclei such as ^{4}He, but for quasideuteron photon interactions, FSI between the relatively slow-moving 'spectator' nucleons is more likely to be significant. FSI may well produce an angular correlation between these nucleons leading to binding of the p-n pair, thereby enhancing the (γ,pn)d yield relative to the (γ,pn)pn yield. In contrast, FSI involving the fast p-n pair should be relatively unimportant in light nuclei and such effects have therefore been neglected in the present analysis. In the ^{12}C(γ,pn) reaction it has been shown that at similar energies [10], the attenuation of the outgoing nucleons is less than 20% and it is likely that a smaller nucleus such as ^{4}He will be even less affected by such FSI.

The (γ,pp) strength is experimentally known to be much less than the (γ,pn) strength (less than 1% of (γ,pn) in the ^{3}He case [11],[12]) and it is therefore likely that effects much weaker than the quasideuteron effect may dominate (γ,pp) contributions. Direct absorption by a p-p pair is strongly suppressed in the case of real photons since absorption requires coupling to the quadrupole moment of the p-p pair. However final state interactions following a (γ,pn) reaction and 3-body interactions may contribute to the (γ,pp) channel.

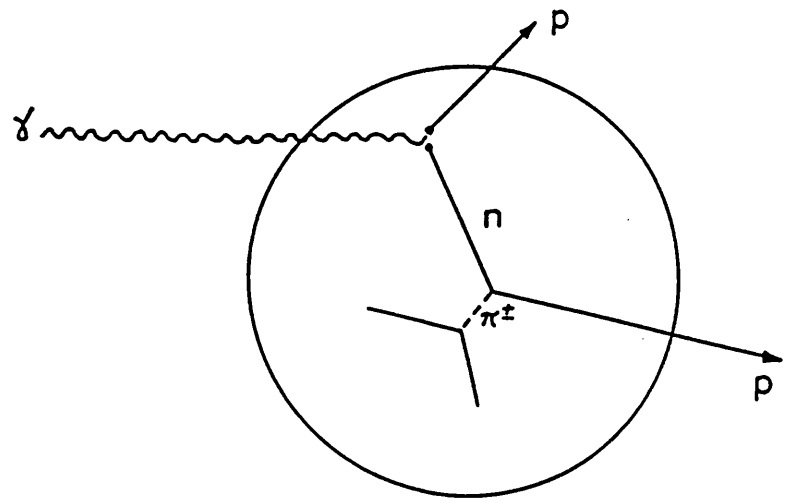

Figure 1.1: (γ,pp) Strength Arising From Final State Interactions

These last two effects can be distinguished to some extent, since three-body effects will not produce p-p angular correlations, whereas in the case of photon absorption on a p-n pair followed by FSI, the angular correlations are not expected to be totally washed out. It is likely that these two effects will dominate the (γ,pp) cross-section since direct absorption on p-p pairs is expected to be very weak indeed. If a 2-nucleon correlation picture is assumed, the (γ,pp) contribution should have little strength in the absence of FSI. On the other hand, if 3-N absorption is significant, this could lead to enhancement of the (γ,pp) strength. Thus this channel may provide some indication as to the significance of 3-N correlations.

^{4}He clearly presents a considerable challenge to experimental measurement, as we shall see later, but its investigation is rewarding. Being a relatively simple nucleus it is a good testing ground for nuclear models. In addition to this, the number of possible distinct final states is small owing to the small number of nucleons. It is possible, by measuring the excitation energy of the residual state, to identify individual reaction channels. The breakup channels may be written explicitly in the

following list:

- Two-body breakup:

  1. (γ,p) ^{3}H, Q-value = 19.3 MeV, which may be identified by observing the single arm missing energy as described in appendix A. This decay mode is studied in detail in ref. [13]. As shown in appendix A, data from this channel are used for energy calibrations of the experimental apparatus.

  2. (γ,n) ^{3}He, Q-value = 20.6 MeV, this channel is not seen by the present measurement owing to the detector configuration used.

  3. (γ,d)d, Q-value = 22.9 MeV, this channel would be expected to have a low cross-section, and may be observed by examining the (γ,d) missing energy, however data on this channel have not been analysed.

- Three-body breakup: (γ,npd), which may be seen as the (γ,pn)d, (γ,pd)n or (γ,d)pn channels. The Q-value for this reaction is 26.1 MeV. Data from the (γ,pn)d channel are reported here.

- Four-body breakup: (γ,npnp), which is observed through both the (γ,pp)nn and the (γ,pn)pn channels. The Q-value for this reaction is 28.3 MeV.

Of these final state particles, only ^{3}He or ^{3}H may have excited states. This compares favourably with the situation for heavy nuclei, where the number of possible final states is large.

1.4 General Considerations

1.4.1 Photon Absorption

When a photon interacts with the nucleus, the photon may interact in any one of the following ways:-

1. Single nucleon knockout: The photon may couple to the charge of a single proton, which may subsequently be ejected with the residual nucleus recoiling to balance momentum. From energy-momentum conservation laws, the proton absorbs almost all of the energy available, but may only do this if it has a large initial momentum.

2. Two-nucleon absorption: If two nucleons are in proximity at the time of interaction, one or both of the nucleons or a meson exchanged between them may initially absorb the photon. The nucleons can absorb the photon's energy and still conserve energy and momentum if the nucleons leave more or less back to back. This mechanism would be favoured over single nucleon knockout for high photon energies.

3. Three-nucleon absorption: Three nucleons may exist in proximity giving additional scope for nucleons being ejected with high relative momenta. Such correlations have been thought improbable by some theorists, but are possibly less so in such a high density nucleus. As already discussed, there is certainly evidence that 3-N absorption is significant in particular parts of the final state phase space.

Previous theoretical work suggests [14, 15] that of these three processes, two-nucleon absorption is the most significant for intermediate energies for ^{4}He, since the

emission of N-N pairs dominates. This would imply that the 2-N absorption model should account for most of the cross-section present. However, it remains to be seen whether or not the quasi-deuteron model is ideally suited to ^{4}He. Because the recoil nucleus would have a significant kinetic energy in a reaction, the recoil nucleus is not acting as a passive spectator as it would for heavier nuclei. In particular, the momentum distribution of the residual nucleus may not be the same as the average distribution in the ^{4}He ground state.

1.4.2 Single Particle Wavefunctions

Some of the simplest models to explain the motions of nucleons within the nucleus are those in which the strong interactions between individual nucleons are averaged, so that a given nucleon is considered to move in a specific effective potential well. Such models are known as independent particle models, and in these models the nuclear wavefunction is directly related to the single nucleon wavefunctions. By virtue of the Pauli exclusion principle, this nuclear wavefunction must be antisymmetric, and therefore takes the form of a Slater determinant.

$$\psi(1,2,...,A) = \frac{1}{\sqrt{A!}} \begin{vmatrix} \psi_{\alpha 1}(1) & \psi_{\alpha 1}(2) & ... & \psi_{\alpha 1}(A) \\ \psi_{\alpha 2}(1) & \psi_{\alpha 2}(2) & ... & \psi_{\alpha 2}(A) \\ \cdot & & & \\ \cdot & & & \\ \cdot & & & \\ \psi_{\alpha A}(1) & \psi_{\alpha A}(2) & ... & \psi_{\alpha A}(A) \end{vmatrix}$$

The single particle wavefunctions each satisfy the Schrödinger equation for their designated effective potential well, V,

$$\left(-\frac{\hbar^2}{2m}\nabla^2 + V(r) - \varepsilon_\alpha\right)\psi_\alpha(\mathbf{r}) = 0$$

where the ε_α are the energies of the nucleon states, where $1 \leq \alpha \leq A$.

1.4.3 The Shell Model

This picture of single nucleons moving independently from one another has led to the shell model picture, where the nucleon hamiltonian is generally expressed in the form

$$H = T + V(r) + \eta(\mathbf{S} \cdot \mathbf{L})$$

where T is the nucleon kinetic energy, $V(r)$ is the nucleon potential energy at a distance r from the nuclear centre and $\mathbf{S} \cdot \mathbf{L}$ describes the spin-orbit coupling. This potential well is often approximated to a simple harmonic oscillator well, whose dimensions are adjusted to fit the nuclear rms charge radius which is derived from electron scattering data.

More realistic potentials such as the Woods-Saxon potential may be used to calculate nucleon wavefunctions [16]. This potential well shape is based on the shape of the nuclear density distribution. It is assumed that because the nuclear density is relatively uniform except at the edges, the force is of finite range. Because the force is of limited range, nucleons will generally interact only with near neighbours. Thus the potential well will be flat, except at the edges of the nucleus. This potential is constructed to allow for the force having finite range and takes the form

$$V(r) = \frac{V_0}{1 + \exp(\frac{r - R_0}{a})}$$

which is closely related to the nucleon density. This model differs from the harmonic oscillator wavefunction in that the tails of the wavefunctions differ considerably. The wavefunctions may be more spread out in the Saxon-Woods case. This model has been successful for closed shell nuclei [16] but still contains the inherent limitations of independent single particle models which are discussed below. Wavefunctions calculated numerically from this potential are reasonably successful in describing

the nucleus [16]. However, the independent particle shell model cannot explain (γ,p) experimental results without including short range residual interactions [17].

1.4.4 Nucleon Pair Correlations

Single particle wavefunction models have a limited degree of success in describing photo-nuclear reactions. In particular they fail to predict properly the highest mismatch momentum components for (γ,p) reactions. Agreement may be improved by including a factor to account for the interactions between individual pairs of nucleons at close range. Such nucleon pair correlations modify the single particle wavefunctions at short range. In this situation, a second nucleon also takes part albeit indirectly in the interaction. This second nucleon may transfer momentum to the interacting proton, but without this nucleon changing state. Alternatively both nucleons may take energy and momentum from the interaction, leading to the emission of N-N pairs. The total cross-section of the two nucleon photo-emission is shown to be directly related to the Fourier transform of the nuclear correlation function [18]. Such 2-nucleon absorption models will be described in detail in chapter 2. In the case of the second nucleon being a neutron, this model is called the quasideuteron model, which is explained in more detail in section 2.2.

The quasideuteron picture has been successful in describing photonuclear reactions on nuclei heavier than ^{4}He, such as ^{12}C [19], ^{6}Li[20] and ^{16}O [21]. This fact would suggest that the quasideuteron model may be appropriate also for ^{4}He. ^{4}He however has some significant differences from other light nuclei.

- ^{4}Heis of much higher density, a fact that favours both 2-N and 3-N correlations.
- Since it is a small nucleus, the protons and neutrons will tend to have high initial momenta.

- Being a light nucleus, the recoil particles will be of high velocity to balance the momenta of the beam photon and the ejected nucleons.

Thus, although the quasi-deuteron picture may well be successful for many light nuclei with low nucleon densities, it very much remains to be seen how best the photonuclear reaction on ^{4}He can be described. The dominant reaction mechanism may be different for each reaction channel and in the (γ,pp) case, the reaction may arise from a number of different mechanisms: photoabsorption on p-p pairs, photoabsorption on 3-N clusters and p-n absorption followed by a FSI on the neutron. Indeed experiments at energies below the real pion threshold show larger (γ,pp) cross-sections than expected, and this may indeed be due in part to FSI's feeding off the dominant p-n absorption mechanism. The (γ,pp) channel is in some ways more interesting than (γ,pn) since it is expected to show a stronger dependence on short range correlations than (γ,pn) [22]

3-N correlations are thought to play only a minor rôle in most nuclei, as photonuclear reactions mainly lead to the ejection of pairs of nucleons through interacting with their electric dipole moment. Such 3-N correlations are also difficult to include in reaction models, since data on $A = 3$ nuclei are scarce.

2-N and 3-N models have many uncertainties and a considerable amount of work has been devoted to exact theoretical treatments on the very lightest nuclei. Full microscopic analyses of nuclear systems only exist for the very lightest nuclei. Recent calculations by Laget [23] [7] for the ^{3}He case, using (exact) three body wavefunctions permit a complete microscopic description of the reaction, including final state interactions. However no such exact treatment exists for ^{4}He as yet, and therefore a more phenomenological model description must be applied.

1.5 Review of Past Work

1.5.1 Experimental Techniques

In the field of photonuclear research, where a beam of photons has been used to initiate the disintegration of target nuclei, there have been two major obstacles which have beset experiments.

1. Photonuclear reactions, being electromagnetic in nature, tend to have low cross-sections.

2. It is difficult to produce a beam of monochromatic photons.

These problems have tended to compound one another, but have recently been addressed through the development of a number of techniques, listed below.

The Photon Difference Method

In the photon difference method, the measurement is carried out twice using bremsstrahlung from electron beams of slightly different energies. The data corresponding to the lower beam energy are appropriately normalised and subtracted from the data for higher beam energy. Unfortunately the subtraction is imperfect since it always includes a small "tail" of lower energy photons, leading to ambiguities in the data analysis. One of the major problems with this technique, therefore, is that it is difficult to observe precisely the photon energy dependence of the cross-section. This has meant that earlier data, which was largely dependent on this technique, was much less reliable than it might have been hoped. In addition, the analysis involved essentially calculating the difference between two large but similar numbers in order

to obtain the relatively much smaller magnitude of the bremsstrahlung difference peak.

Positron Annihilation

A similar technique utilises the process of positron annihilation, which exploits the charge independence of bremsstrahlung in the following way. The experiment uses the photons resulting from positrons interacting with a low-Z material such as beryllium [24] to produce bremsstrahlung plus a peak corresponding to e^+, e^- annihilation giving two photons whose average energy is determined by the initial positron beam energy. The measurement is repeated with an electron beam to produce the bremsstrahlung tail alone, and this dataset is subtracted from the positron dataset. The result is effectively a broad peak of photons of roughly the same energy. Positron annihilation-in-flight can also be used in conjunction with photon tagging when a beam of positrons interacts with a low-Z material. The annihilation process produces two photons. The energy, time and angle of one of the two photons (the photon of lower energy in the lab frame) is measured in order to tag the energy of the other photon, which interacts with the nuclear target.

Laser Backscattering

A further method that is used is that of laser backscattering, using inverse compton scattering from a powerful laser beam. The photon beam resulting is fairly monochromatic, but very low in intensity. In the case of the experimental facility LEGS, the recoil electrons are detected in a tagging spectrometer and backscattered tagged photon beam rates of 1.3×10^7 per second have been achieved.

The Present Method of Photon Tagging

The present work avoids many of the previous difficulties which have been encountered in the past, since it uses the long known but only recently exploited tagged photon technique. This yields a useful beam flux, gives a good measure of beam intensity ($\sim 2 \times 10^7$), and wholly dispenses with the problem of monochromaticity. This technique uses a CW electron beam of precisely determined energy, which interacts with a thin sheet of material to produce bremsstrahlung. The emerging electrons are momentum analysed for each event. From the energy losses suffered by the electrons, the energies of the bremsstrahlung photons may be deduced. In the present measurement, a photon energy resolution of 0.5 MeV is achieved. This compares favourably with the energy resolutions for detection of the reaction products, these being typically ~3-5 MeV. In addition, the design of the tagger allows measurements over a broad photon energy range, which should enable the photon energy dependence of the reaction yield to be much more accurately determined than was previously possible.

1.5.2 Previous Reaction Measurements

This section reports on previous experimental work which has been undertaken to gain a better understanding of the nucleus, and in particular, nucleonic correlations. The complementary theoretical developments which have arisen from these experiments are described in chapter 2.

Proton Capture

In the past it has been widely thought that the (p,γ) reaction was more practicable for studying the nucleus than photonuclear reactions. This reaction avoided the complications of achieving a monochromatic photon beam and therefore could be carried out with greater precision. Through the principle of detailed balance, reactions leaving the residual nucleus in its ground state could measure the same matrix elements as the (γ,p) reaction. Reactions leaving the residual nucleus in an excited state could moreover measure matrix elements inaccessible to (γ,p) reactions. However the problems of obtaining effective monochromatic photon beams have been overcome and photonuclear reactions now offer a more versatile method of probing the nucleus than (p,γ) reactions which are restricted to a single proton energy.

Pion Induced Reactions

Pion induced reactions are similar in many ways to photon induced reactions, and it is to be expected that some of the features which characterise pion reactions will also be important in photoreactions. The pion, being of small mass compared to the nucleon ($\sim$140 MeV/c^2) can supply a large quantity of energy accompanied by almost no momentum. This makes the pion in theory suited to the study of N-N correlations. Data on π^- absorption on ^{6}Li show that 70 % of the absorption cross-section proceeds by the emission of n-n pairs [26], and both the (π^+,pp) and (π^-,nn) reactions show significant angular correlations. In the case of ^{4}He, Steinacher *et.al.* [27] studied charged pion absorption in the energy range 65-165 MeV. The (π,NN) results were consistent with an N-N pair absorption mechanism. In the particular case of the (π^+,pp)pn reaction, results were consistent with absorption on a p-n pair involving a Δ-N intermediate state and the shapes of the angular

distributions were in very good agreement with absorption on a quasideuteron.

The evidence for absorption on 3-N clusters in which only one nucleon acts as spectator has also been established in a separate study [28]. The evidence suggests that total cross-sections cannot be explained without including significant absorption on 3-N clusters.

However at the most fundamental level, the interaction beteen pions and nucleons is less well understood than the electromagnetic interaction between photons and nucleons or meson exchange currents and it appears difficult to distinguish between π-N interactions and N-N interactions. In addition, the study of pion absorption on N-N pairs or clusters is complicated by initial state interactions which in contrast, are absent in photonuclear reactions, with which the present work is concerned.

Photonuclear Experiments

As discussed above, experiments involving the absorption of protons or pions yield useful information about the nucleus, and in the latter case, are useful in the study of nucleonic correlations. However both reactions are significantly affected by initial state interactions. The present work, however, uses a photon beam to probe the nucleus, and initial state interactions can therefore be safely neglected. Much experimental work has been carried out in photonuclear reactions, and the remainder of this section is devoted to describing experimental evidence in this field.

Experimental work at intermediate energies has shown [29, 30, 31, 32, 33, 34] that photonuclear reactions yield predominantly correlated proton-neutron (p-n) pairs. The p-n pairs depart from the nucleus almost back to back, suggesting that the photon interacts with the pair, which has a separation of less than $\sim$1fm, leaving the remainder of the nucleus largely undisturbed. Furthermore, at these photon

energies, it is likely that the initial separation distance is small, with the p-n pair perhaps exchanging charged virtual mesons. Therefore a study of the (γ,pn) reaction should help in understanding p-n pair correlations.

Levinger in 1951 [1] was the first to propose that the photodisintegration of complex nuclei by photons more energetic than those in the giant dipole resonance region proceeded by the absorption of the photon on a proton-neutron pair known as a quasideuteron. Early work on photoprotons [35, 36] ejected by photons in the 100-300 MeV region suggested such a mechanism qualitatively but quantitative proof was lacking. Correlated pairs were observed [37, 38, 29] but this work did not reveal the degree to which photoprotons were accompanied by photoneutrons. Barton and Smith [31] tried to test quantitatively the Levinger model on helium and lithium using 280 MeV bremsstrahlung detecting protons and neutrons in the energy range 50-150 MeV using scintillator detectors and concluded that nearly all high energy photodisintegrations leading to the emission of a high energy proton proceed by the interaction of a photon with a proton-neutron pair.

Reid and Lalovic [39] studied photonuclear reactions on ^{4}He and observed 24 events in an expansion cloud chamber experiment with a 330 MeV synchrotron beam and concluded that these events were due to the ^{4}He (γ,pd)n and ^{4}He (γ,pp)nn reactions. However this experiment was limited by the fact that only protons of energy above 80 MeV were recorded. Investigations of the neutron angles showed that for a given proton angle, the neutron angular distribution was spread around the unique direction in which neutrons would have been emitted had the experiment been carried out on deuterium. This gives further credence to the picture of a quasi-deuteron moving within the nucleus, interacting with the photon while the rest of the nucleus acts largely as a spectator.

Gorbunov and Spiridonov [40],[41] studied the 3- and 4-body breakup of ^{4}He using a cloud chamber with a bremsstrahlung beam of 170 MeV. They analysed 91 ^{4}He (γ,pd)n events to obtain cross-sections, angular distributions and correlations for the ^{4}He (γ,pd)n channel. They noted that the proton and neutron angular distributions for (γ,pn) were very similar to those for deuterium. The reaction cross-section showed a resonance peak of $\sim$170μb at 50 MeV falling to $\sim$40μb above 100 MeV. For photon energies below 75 MeV the cross-sections for 3- and 4-body breakup channels was reported as less than 10% of the total cross-section, but for the 75-170 MeV range, these channels contributed about 30% of the total. Through observing angular distributions they concluded that the (γ,pn) reaction proceeded via a quasideuteron mechanism, whereas the 2-body breakup reactions were attributed to single nucleon knockout. For the ^{4}He (γ,pp)nn channel, the cross-section was found to be relatively constant for photon energies above $\sim$35 MeV. They concluded that the reaction proceeded via photon absorption on 2 correlated nucleons. However (γ,p)t and (γ,^{3}He) were characterised by single nucleon knockout. The total integrated cross-section for photoabsorption in the energy range studied was found to be $\sim$95 MeVmb which was in good agreement with the sum rule calculations for electric dipole absorption by Rustgi and Levinger [42] which predicted a figure of 89 MeVmb.

Arkatov *et.al.* [43] carried out a similar experiment with 120 MeV bremsstrahlung. In this experiment 2320 events were analysed, a significant improvement on previous experiments. They obtained a slightly higher ^{4}He (γ,pd)n/(γ,pp)nn cross-section ratio which was probably due to difficulties in separating the contributions from the two breakup modes.

Balestra *et.al.* [44, 45] used a diffusion cloud chamber with a 100 MeV syn-

chrotron beam to study the photodisintegration of ^{4}He. They discovered that the 3- and 4-body breakup cross-sections were a factor of ~10 lower than the 2-body breakup contribution. By observing the angular distribution and the energies of the emitted particles they concluded that for photon energies of less than ~60 MeV the main mechanism for the 3-body breakup mode was absorption on N-N pairs. The 4-body breakup showed a large angle on average between the two protons, suggesting a direct reaction mechanism. They proposed that the photon was effectively absorbed on one quasideuteron, correlated to a second quasideuteron, both of which then disintegrated. The cross-sections measured for 50-70 MeV were 120μb for 3-body and ~70μb for 4-body breakup.

The ^{4}He (γ,ppn)n channel has been studied more recently in the Δ-resonance region by Emura *et.al.* [46, 47] using tagged photons in the range 135-455 MeV. The cross-sections were observed to rise from negligible at the lowest photon energies up to ~45 μb for the higher energies. The momentum distribution of the detected nucleons at photon energies close to the Δ-resonance could not be described adequately by quasideuteron absorption of the photon. The data at these energies in fact favoured absorption on p-p pairs or on p-p-n clusters.

Summing up

For the energies with which the present work is concerned, single nucleon knockout reactions are expected to be strongly suppressed, as such a reaction requires the initial nucleon momentum to be very high for complete photon absorption. Photon rescattering would in theory permit single nucleons to absorb more of the photon energy, but such reactions tend to have minute cross-sections due to the weak coupling strengths present. The photon's high energy coupled with low momentum would

not however suppress reactions between the photon and groups of two or more nucleons. Indeed such reactions dominate at photon energies above 50 MeV. The quasi-deuteron model of Levinger has been successful in describing photonuclear interactions on some light nuclei ^{12}C [19],[49] ^{16}O [21] and ^{6}Li [20] and has been shown to give a much better agreement with experiment than single particle models or phase space models.

1.6 Aims of the Current Work

This thesis describes a photonuclear measurement which was carried out on the ^{4}He nucleus, using the tagged photon facility available at the University of Mainz. This experiment was designed to detect two ejected particles from the $\gamma + \alpha$ reaction in coincidence with the incident photon of known energy. The detector arrays were position and energy sensitive, and in addition could be used to identify protons, neutrons and deuterons. Two separate runs were carried out, in February and August of 1987. The present analysis deals with the decay channels leading to p-p and p-n angular correlations. The (γ,p) channel is also of interest, and this channel is studied in detail in reference [13], using the same data. The channels which may be studied using the present data are listed in full in section 1.3 on page 10. The apparatus used to study these channels is described in detail in chapter 3.

Measurements and Comparisons with Theory

This thesis presents results for the (γ,pn) and (γ,pp) missing energy distributions and missing momentum distributions for the ^{4}He nucleus. The cross-sections for specific channels will also be evaluated. The (γ,pn)d and (γ,pn)pn breakup channels will be examined separately to reveal both the differences and the similarities

between them and the results will be compared with data from recent experiments carried out on ^{6}Li, ^{16}O and ^{12}C.

Owing to the fact that the photon energy is well determined, this experiment will be especially sensitive to the photon energy dependence of the (γ,NN) cross-sections for the photon energy range available. The current measurement on the ^{4}He nucleus should reveal to what extent the quasideuteron model or a phase space model can describe the mechanics of these reactions. Information about the missing momentum distributions, for each channel will be extracted and compared with various model predictions.

Chapter 2

Theory of Photonuclear Reactions

2.1 Photo-absorption

The total photoabsorption cross-section per nucleon is shown in figure 2.1 [51]. This gives an overview of the total photoabsorption cross-section per nucleon in the range 10-10^5MeV. Two large peaks are discernible. The peak at lower energy is known as the giant resonance peak. In this region the photon is primarily absorbed via dipole transitions leading to collective modes of nuclear excitation. The higher energy peak occurs a little way above the threshold for real pions ($\sim$140 MeV centre of mass energy). In this region the cross-section is influenced by nucleon excitation via the Δ-resonance, and the strength of this effect increases rapidly above this energy, becoming dominant above $\sim$200 MeV in the deuterium case (fig. 22 of reference [52]). In this region, above pion threshold, the cross-section per nucleon is almost independent of the nucleus concerned, except for the case of ^{1}H. This discrepancy regarding the single proton is largely explained by nucleon Fermi motion and by Pauli blocking which affect nucleons which are in proximity with other nucleons. In the intermediate region, between the giant resonance peaks, and the real pion threshold, the cross-section is markedly lower, and very slowly decreasing with energy [51]. It

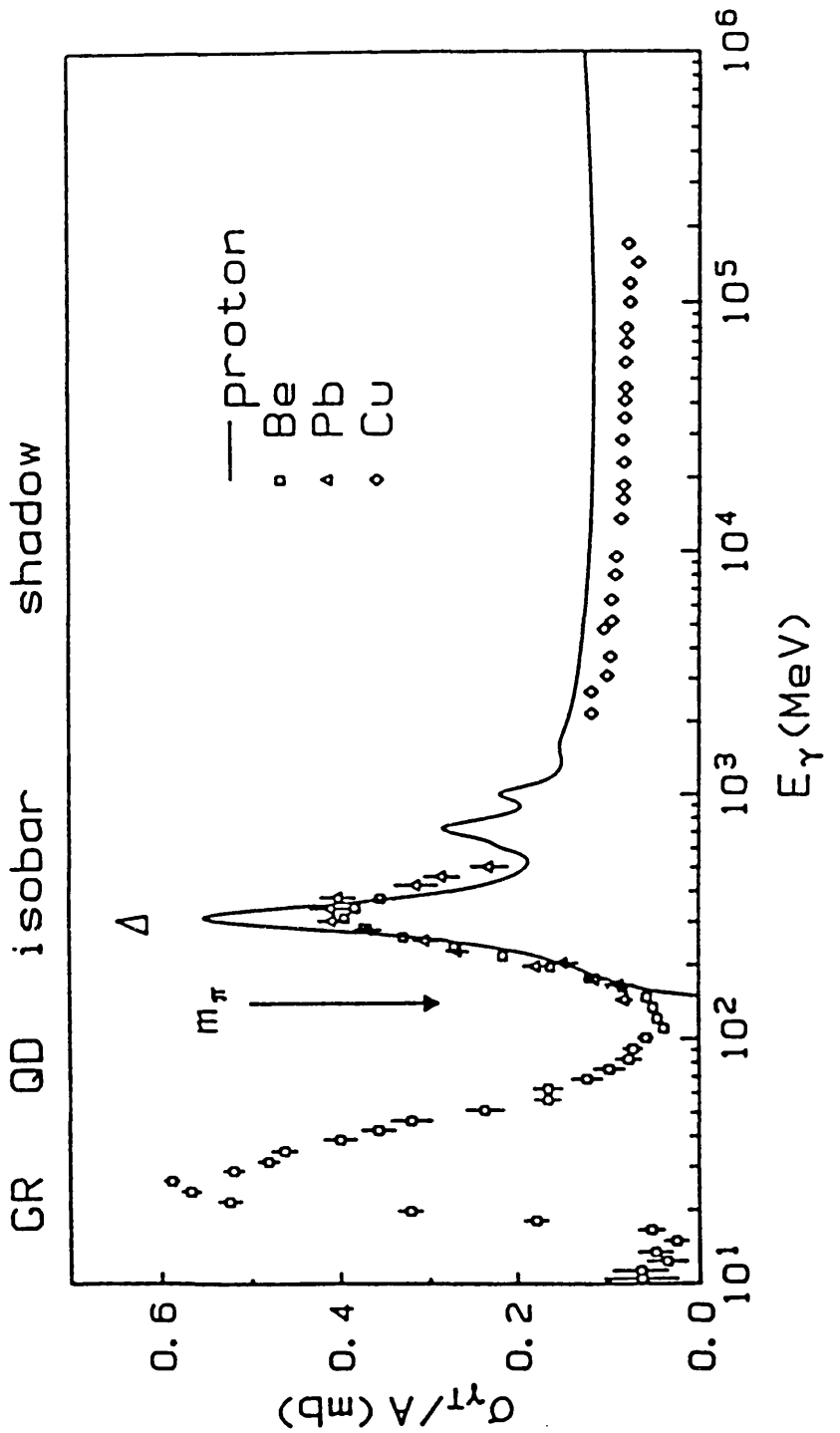

Figure 2.1: Total Photoabsorption cross-section per nucleon for beryllium, lead and copper, for the energy range 10-10^5 MeV. The graph shows the giant resonance region (GR), the quasi-deuteron region below pion threshold (QD) and the Δ-resonance region above the pion threshold.

is within this intermediate energy region that the present measurement is concerned, where the absorption due to p-n (proton-neutron) pair correlations is thought to be dominant.

Perhaps the simplest photonuclear reactions to study are the (γ,p) reactions, where the momentum mismatch, q, is defined [54] by $q = \mid \mathbf{p}_\gamma - \mathbf{p}_p \mid$, where $\mathbf{p}_p$ is the momentum of the proton immediately after photoabsorption and $\mathbf{p}_\gamma$ is the photon momentum. At photon energies of the order of 60 MeV, where the corresponding wavelength is $\sim \frac{h}{60MeV/c}$, or 1.52 fm, the photon would be expected to interact with only a small fraction of the nucleus. In single nucleon knockout reactions, it is likely that the photon transfers almost all of its energy to a single nucleon within the nucleus, the remainder of the energy being transferred to the residual nucleus to balance momentum. This reaction is called quasi-free knockout because the remainder of the nucleus acts as a spectator to the reaction.

Figure 2.2 shows the exclusive (γ,p) cross-section for ^{16}O as a function of momentum mismatch, q, from the data of Leitch *et.al.* [53] taken at the Kelvin Laboratory and at MIT. These results can be partially produced in a simplistic way from a realistic Woods-Saxon shell model potential folded with Bessel functions, based on a direct knockout reaction mechanism, where the cross-section for angular momentum l is given by

$$\sigma(q) \propto \mid \int_{r=0}^{\infty} R(r) r^2 j_l(qr) \mathrm{d}r \mid^2 \tag{2.1}$$

A slightly more sophisticated model could alternatively be used where the photon interacts with a correlated p-n pair, where momentum, but not energy, is imparted to the neutron. The neutron remains bound so that its wavefunction contributes as a power of 2 (see figure 2.3), thus

$$\sigma(q) \propto \mid \int_{0}^{\infty} R_p(r)[R_n(r)]^2 r^2 j_l(qr) \mathrm{d}r \mid^2 \tag{2.2}$$

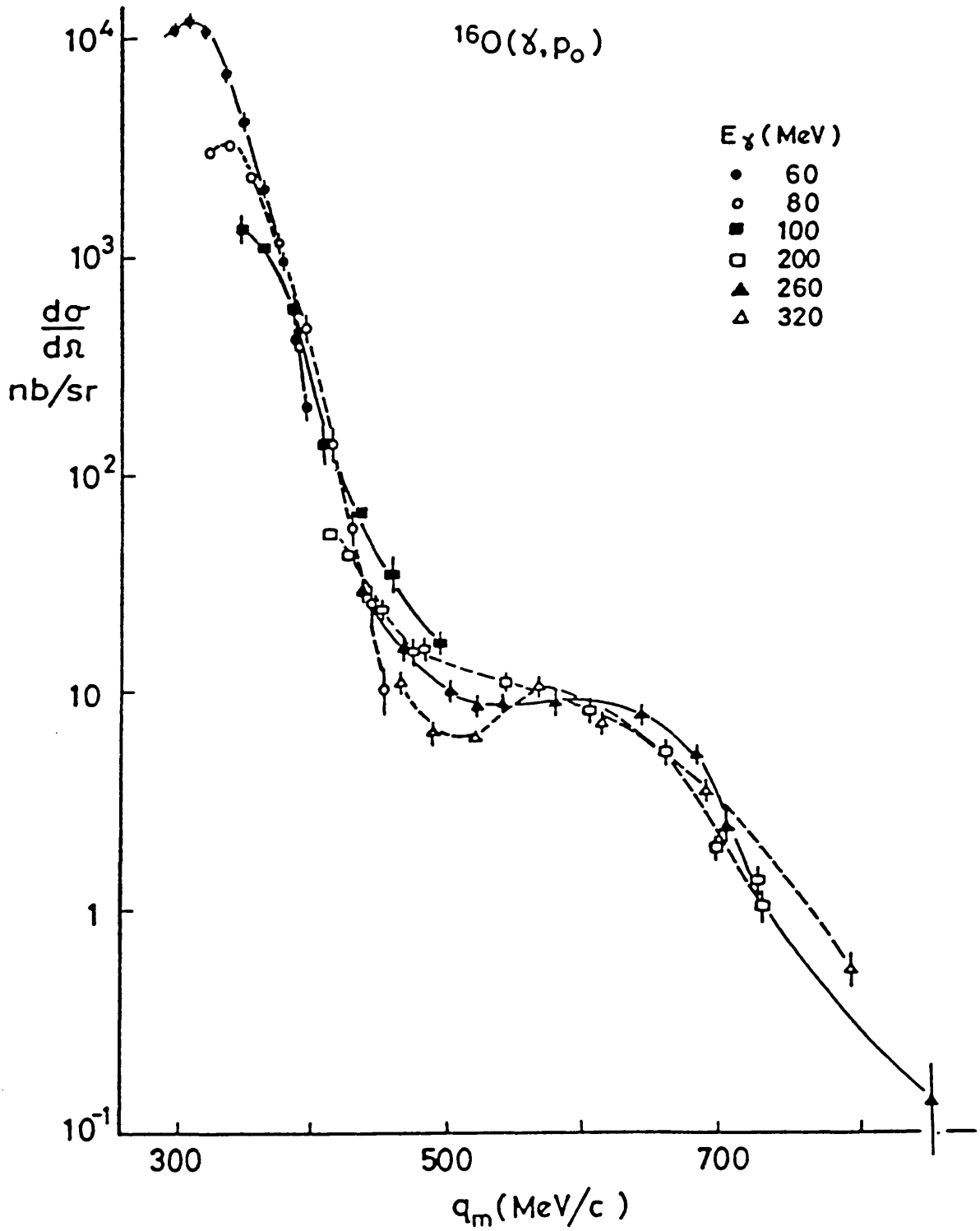

Figure 2.2: Exclusive (γ,p) cross-section for ^{16}O shown against mismatch momentum q_m

Such a reaction, which implicitly assumes zero range N-N interactions, may be made to fit the data by choosing suitable scaling [54], however this model is of limited validity for this reason.

Nevertheless this suggests, that for the energy range concerned, the (γ,p) cross-section may be sensitive to p-n correlations. In addition, theoretical calculations[55] using realistic nucleon-nucleon interactions show that the contributions coming from nucleon correlations are dominant for mismatch momenta higher than the Fermi momentum for nucleons.

These results suggest that the photoreactions are sensitive to nucleon-nucleon correlations, but the most direct way to test this is to study (γ,NN) reactions. Since high energy photons interact mainly by E1 absorption, photon interactions are expected to be especially sensitive to p-n pairs, which exchange charged mesons and have an electric dipole moment. A p-p pair within the nucleus, on the other hand, will not exchange charged mesons and may only couple to the photon via their quadrupole moment. Therefore the strength of photon absorption on correlated p-p pairs is expected to be much weaker than the QD strength.

The current status of the theory concerning photonuclear reactions at intermediate energies is still rather rudimentary. Until recently the precision of (γ,NN) experiments has been rather poor and this has provided little incentive to the development of the theory. It is only now that models proposed thirty years ago are being developed further. However some aspects of the theory have been developed in recent years in the lightest nuclei with the development of the solutions to the 3-nucleon bound state Faddeev equations [56]. This has been a great step towards understanding the ^{3}He nucleus in a model independent way, but full microscopic theories are still lacking for ^{4}He.

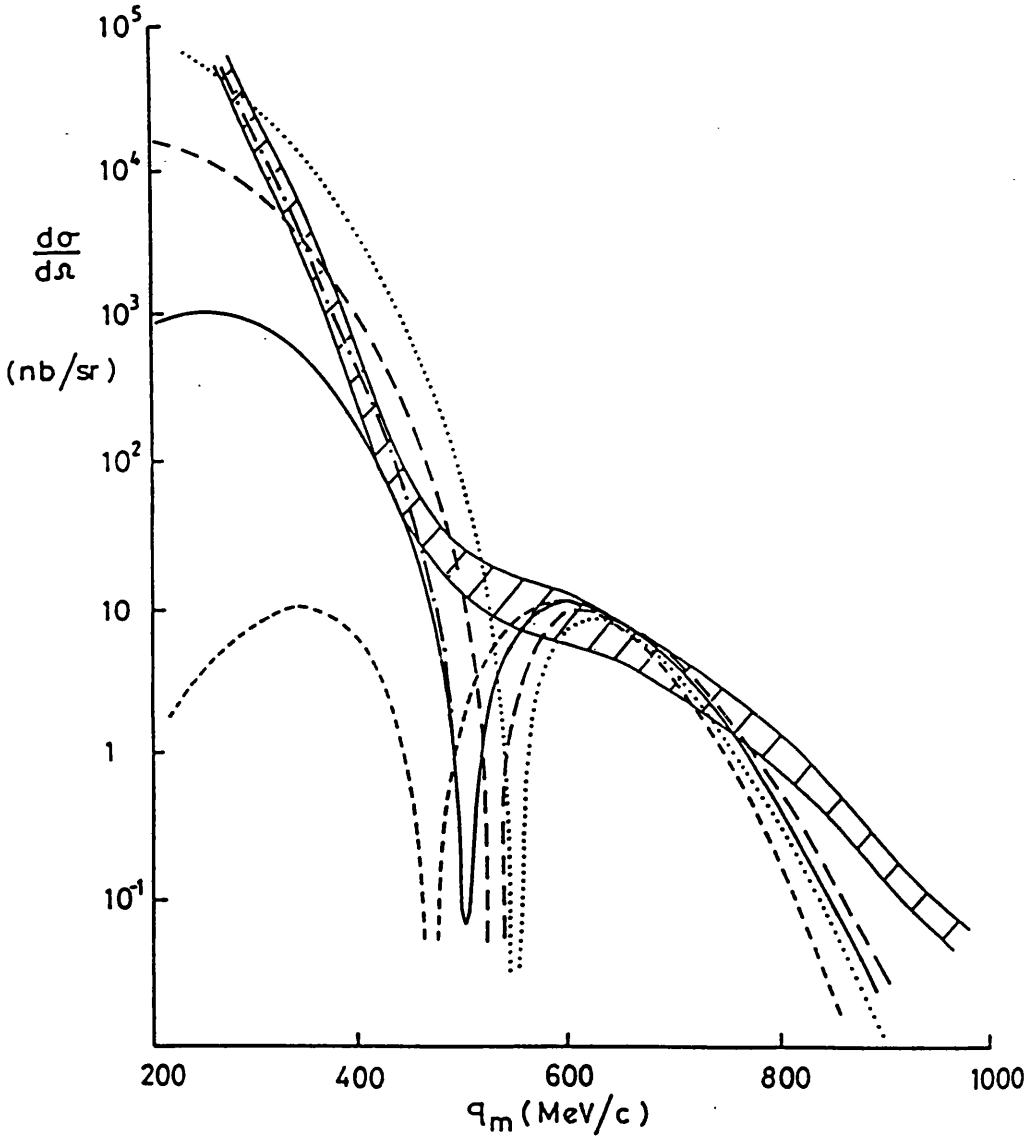

Figure 2.3: Comparison of the $^{16}O(\gamma,p_0)$ scaling function with Jastrow model calculations. The shaded area represents experimental data. The short-broken curve represents predictions for Bessel functions in the calculations of the term representing the 2N mechanism.

2.2 The quasi-deuteron Model

2.2.1 Nucleon Pair Correlations

Heidmann[57] attempted to explain the (N,d) pickup reaction by using a two-nucleon model, where the nucleus was considered to be an $(A-2)$ nucleus with a p-n pair travelling within it. This model was successful in explaining the surprisingly large pickup cross-section given the small binding energy of the deuteron. This picture was later used by Levinger [1] to account for the unexpectedly high strength of the photonuclear process at intermediate energies. In the Levinger treatment, the nucleus was viewed as an interacting p-n pair and $(A-2)$ non-participating "spectator" nucleons. It was assumed that if the distance between a proton and a neutron is much smaller than the average internucleon spacing in the nucleus, then it is unlikely that other nucleons will be similarly near to the two nucleons which are very close together. This model has become known as the quasideuteron model of Levinger.

Levinger predicted that because the photon interacts with quasideuterons, the photonuclear absorption cross-section should be proportional both to the density of quasideuterons, $\frac{NZ}{A}$, and to the deuteron cross section, σ_{d}. The cross-section, σ_{qd}, is therefore of the form

$$\sigma_{\mathrm{qd}}(E_\gamma) = L\frac{NZ}{A}\,\overline{\sigma_{\mathrm{d}}(E_\gamma)}, \qquad E_\gamma \geq 100\mathrm{MeV} \tag{2.3}$$

where the line above indicates that the real deuteron cross-section used is an appropriately weighted average, to take account of the Fermi motion associated with the quasideuteron. The parameter L (called the Levinger parameter) takes into account the enhancement in the cross-section due to the increased p-n coupling

in the quasideuteron. In his original paper [1] in 1951, Levinger quoted a value for L of 6.4 for photon energies above ~150 MeV, with a slightly lower value for energies less than this. This model, however, did not take account of Pauli-blocking, which would be expected to be significant in heavier nuclei. Levinger later proposed [58] a "modified quasideuteron model" to account for this, where the total cross-section was given by

$$\sigma_{MQD}(E_\gamma) = L\frac{NZ}{A}\sigma_d(E_\gamma)\exp(-D/E_\gamma) \tag{2.4}$$

where D is ~60 MeV. Tavares *et.al.* [59] proposed that L would be a weak function of A, and gave an expression for L of

$$L = 2.1\ln(1.3A) \tag{2.5}$$

This gives a value of 11.8 for Pb which was closely in agreement with the work of Leprêtre *et.al.* [60, 61] who studied the Pb cross-section in the range 34-132 MeV and obtained a value for L of 13.25 and a value of 67.4 MeV for D by fitting equation 2.4 to their data.

Levinger's model was further developed by Gottfried [9] (strictly for closed shell nuclei), who expressed the p-n pair correlation in the form of a Jastrow-type [62] correlation function for the p-n pair.

$$\rho(\mathbf{r}_1, \mathbf{r}_2) = \rho_s(\mathbf{r}_1, \mathbf{r}_2) \mid g(\mid \mathbf{r}_1 - \mathbf{r}_2 \mid) \mid^2 \tag{2.6}$$

where ρ_s could be derived from the shell model independent particle wavefunctions, which give a good description of the nuclear wavefunction when nucleons are well separated. Correlations are contained within the Jastrow-type function g, which may be related to the ground state deuteron wavefunction. ρ_s determines the quantity $F(P)$, which is the relative probability of a p-n pair having a total momentum P.

The cross-section can be expressed as [9]

$$\mathrm{d}\sigma = \frac{1}{(2\pi)^4} F(P) S_{\mathrm{fi}} \delta(\mathrm{E_f} - \mathrm{E_i}) \mathrm{d}^3\mathbf{p}_\mathrm{p} \mathrm{d}^3\mathbf{p}_\mathrm{n} \tag{2.7}$$

where the factor S_{fi} is the probability that two particles in a state of relative motion given by the short range correlation function perform a transition to the final scattering state [63]. It represents the more violent correlations of the p-n pair, and is related to the deuteron wavefunction through the relation

$$S_{\mathrm{fi}} = 3\gamma^3 \frac{4\pi}{p_p^\star E_p^\star} \left(\frac{\mathrm{d}\sigma_\mathrm{d}}{\mathrm{d}\Omega}\right)^\star \tag{2.8}$$

where γ is a proportionality constant and the $\star$ indicates that the quantity corresponds to the centre of momentum frame. The form factor $F(P)$ in the cross section (representing the incoming photon and ejected proton and neutron by plane waves) is given by

$$F(P) \propto \left| \int_\tau e^{i\mathbf{r}\cdot\mathbf{p}_p} e^{i\mathbf{r}\cdot\mathbf{p}_n} \psi_p(r) \psi_n(r) e^{-i\mathbf{r}\cdot\boldsymbol{k}_\gamma} \mathrm{d}^3\mathbf{r} \right|^2 \tag{2.9}$$

where again the integral is taken over all space, where $\psi_p(r)$ and $\psi_n(r)$ are the radial parts of the single particle wavefunction for the proton and the neutron and $\mathbf{p}_p$ and $\mathbf{p}_n$ are the proton and neutron momenta respectively. Since $\mathrm{d}^3\mathbf{r}$ is a volume element, this leads to

$$\int_{r=0}^{\infty} \int_{\theta=0}^{\pi} \mathrm{d}r \cdot \mathrm{d}\theta r^2 \sin\theta e^{i\mathbf{r}\cdot(\mathbf{p}_p + \mathbf{p}_n - \boldsymbol{k}_\gamma)} \psi_p(r) \psi_n(r) \tag{2.10}$$

for $l = 0$ states, where θ is the angle between $\mathbf{r}$ and $(\mathbf{p}_p + \mathbf{p}_n - \boldsymbol{k}_\gamma)$. This leads to

$$F(P) \propto \int_{r=0}^{\infty} \mathrm{d}r \cdot r^2 \psi_p(r) \psi_n(r) j_0(Pr) \tag{2.11}$$

for

$$P = \left| \mathbf{p}_p + \mathbf{p}_n - \boldsymbol{k}_\gamma \right| \tag{2.12}$$

The above treatment applies only to $l = 0$ states, however these are the only states

present in the ^{4}He nucleus. The more general form of the above equation [63] is

$$F(P) = \sum_{n,n',l,l'} \sum_{\rho=|l-l'|}^{l+l'} (2l+1)(2l'+1) \mid \langle ll'00 \mid \rho 0 \rangle \mid^2 . \\ \mid \int_0^\infty R_{n,l}(r) R_{n',l'}(r) j_\rho(Pr) r^2 \cdot \mathrm{d}r \mid^2 \tag{2.13}$$

where $R_{n,l}$ is the radial wavefunction for a nucleon of principal quantum number n and angular momentum l.

Meson Exchange Effects

Calculations by Fink and Gari [64, 65] indicate that the experimental photoproton and photoneutron cross-sections cannot be reproduced theoretically unless meson exchange currents are included in the calculation. Boato and Giannini[18] recently gave Gottfried's treatment some justification with regard to this, showing that the Gottfried factorisation is valid not only in explaining effects due to p-n correlations, but also in the presence of MEC and that the total cross-section of the 2-N photoemission is directly related to the Fourier transform of the nuclear correlation function. In their treatment, the (γ,pn) cross-section is given by the relation [18]

$$\mathrm{d}\sigma = \frac{(2\pi)^{-7}}{\omega} \mid \langle \beta \mid \mathrm{T} \mid \alpha \rangle \mid^2 \delta(\mathrm{E_f} - \mathrm{E_i}) \mathrm{d}^3\mathbf{p}_1 \mathrm{d}^3\mathbf{p}_2 \mathrm{d}^3\mathbf{p}_\mathrm{R} \tag{2.14}$$

where β and α denote the final and initial states respectively. T is the electromagnetic operator, given by

$$T = \int \mathrm{d}\mathbf{r} e^{i\mathbf{q}\cdot\mathbf{r}} \varepsilon_\lambda \cdot \mathbf{J}(\mathbf{r}) \tag{2.15}$$

where ε_λ is the polarisation vector of the photon, and $\mathbf{J}(\mathbf{r})$ is the total electromagnetic current.

Final State Interactions

After the photon has interacted with the quasideuteron, the participating nucleons may interact with the remainder of the nucleus giving final state interactions (FSI). Interactions between ejected nucleons and the residual nucleus can distort the cross-section in two ways, firstly, the nucleon may be absorbed, and secondly, as the nucleon leaves the residual nucleus, there is a slight "refraction" effect. A correction for both of these final state interaction effects was attempted by Gottfried. This was done by applying the factor $f_a(\frac{2R_0}{\lambda_a})\Gamma(\mathbf{p}_p, \mathbf{p}_n)$. f_a represents the absorption of outgoing nucleons and is derived from the nuclear radius, R_0, and the mean free path for absorption, λ_a. Γ represents the weak refraction that occurs as the nucleons of centre of mass momenta $\mathbf{p}_p$ and $\mathbf{p}_n$ leave the nucleus. These factors can in theory be included in the Monte-Carlo simulation of the experiment but this correction was not applied in the present analysis since the effect of weak refraction and absorption of fast nucleons are not expected to be very large in the case of ^{4}He. A more significant effect in the ^{4}He (γ,pn) case, however, is likely to be FSI between the two recoil nucleons leading to a bound deuteron.

2.2.2 The Pair Momentum Distribution for ^{4}He

The pair momentum distribution, $F(P)$, for ^{4}He, can be calculated using single particle shell model calculations. If all of the ^{4}He nucleons are in simple harmonic oscillator potentials, then for ^{4}He, which contains only $l = 0$ states, equation 2.13 simplifies to

$$F(P) = \left| \int_0^\infty [R_{00}(r)]^2 j_0(Pr) \mathrm{d}r \right|^2 \tag{2.16}$$

where $R_{ab}(r)$ is the radial wavefunction for a nucleon of principal quantum number a and angular momentum b. Let R_{00} be a simple harmonic oscillator function

$$R(r) = Ne^{-\beta r^2/2} \tag{2.17}$$

then

$$F(P) \propto \left| \int_0^\infty e^{-\beta r^2} j_0(Pr) \mathrm{d}r \right|^2 \tag{2.18}$$

but since

$$\int_0^\infty e^{-\beta r^2} j_0(Pr) \mathrm{d}r = \frac{\sqrt{\pi}}{4\beta^{3/2}} e^{-P^2/4\beta} \tag{2.19}$$

then

$$F(P) \propto e^{-P^2/2\beta} \tag{2.20}$$

If a centre of mass correction is applied to the 4-nucleon system, it can be shown that the rms radius R_0 is given by

$$R_0^2 = \frac{9}{8\beta} \tag{2.21}$$

The value of R_0, the rms radius for a nucleon in ^{4}He is taken to be 1.67 fm [66], giving

$$\beta = 0.3847 \mathrm{fm}^{-2} \tag{2.22}$$

2.3 Variational Wavefunctions for ^{4}He

A more sophisticated method of obtaining the $F(P)$ distribution is to use variational wavefunctions. Schiavilla and Pandharipande [67] have developed a general Monte Carlo method for obtaining the momentum distributions of nucleons and nucleon clusters. The calculations are based on a pair correlation function of the form

$$\begin{aligned} F_{ij} &= f^c(r_{ij})[1 + u^\sigma(r_{ij})\boldsymbol{\sigma}_i \cdot \boldsymbol{\sigma}_j + u^{t\tau}(r_{ij})S_{ij}\boldsymbol{\tau}_i \cdot \boldsymbol{\tau}_j] \\ &\equiv f^c(r_{ij})[1 + \textstyle\sum_p u^p(r_{ij})O^p_{ij}] \end{aligned} \tag{2.23}$$

where $f^c(r_{ij})$ represents central correlations, and depends only on the distance between two nucleons. $u^\sigma(r_{ij})$ is included to account for tensor correlations and $u^{t\tau}(r_{ij})$ is included to account for spin correlations. The nuclear wavefunction is then written in the form

$$\psi_v = \{S \prod_{i<j} f^c(r_{ij})[1 + \sum_p (\prod_{k\neq i,j} f^p_{ijk})u^p(r_{ij})O^p_{ij}]\}\Phi \tag{2.24}$$

where the factor f_{ijk} is included as a perturbation to take account of the effects of other nucleons, S is the symmetrizer and the Φ are antisymmetric non-interacting wavefunctions. The correlation functions $f^c(r)$, $u^\sigma(r)$ and $u^\tau(r)$, and the parameters f_{ijk} are determined variationally to minimise the overall energy, ignoring coulomb interactions. The probability of finding a nucleon with spin projection s and isospin projection t is given in terms of creation and destruction operators for the ground state nucleus, represented by $\mid A\rangle$, and is

$$N_{s,t}(\boldsymbol{k}) = \langle A \mid a^+_{s,t}(\boldsymbol{k})a_{s,t}(\boldsymbol{k}) \mid A\rangle \tag{2.25}$$

The nucleon momentum distributions are then obtained by summing $N_{s,t}(\boldsymbol{k})$

over all possible spin and isospin states.

$$N_{s,t}(\boldsymbol{k}) = \frac{A}{\Omega N_A} \int \psi_A^+(\boldsymbol{r}'_1, ..., \boldsymbol{r}_A) P_s(1) P_t(1) e^{i\boldsymbol{k}\cdot(\boldsymbol{r}'_1 - \boldsymbol{r}_1)} \cdot \psi_A(\boldsymbol{r}_1, ..., \boldsymbol{r}_A) \mathrm{d}\boldsymbol{r}'_1 \mathrm{d}\boldsymbol{r}_1, ..., \mathrm{d}\boldsymbol{r}_A \tag{2.26}$$

where N_A and Ω represent the wavefunction normalisation and normalisation volume. The nuclear wavefunctions are written

$$\psi_A = [\prod_{i<j\leq A} f^c(r_{ij})] M_A(\boldsymbol{r}_1, ..., \boldsymbol{r}_A) \Phi_A \tag{2.27}$$

where Φ_A are uncorrelated wavefunctions which have no dependence upon the coordinates $\boldsymbol{r}_i$. $M_A(\boldsymbol{r}_1, ..., \boldsymbol{r}_A)$ is a matrix operator given by

$$M_A(\boldsymbol{r}_1, ..., \boldsymbol{r}_A) = S \prod_{i<j} [1 + \sum_p (\prod_{k\neq i,j} f^p_{ijk}) u^p(r_{ij}) O^p_{ij}] \tag{2.28}$$

The momentum distributions for the nucleons are obtained by using Monte Carlo techniques to sample the integrand

$$W(\boldsymbol{R}) X(t, \boldsymbol{k}, \boldsymbol{R}) \tag{2.29}$$

to give

$$N_p(\boldsymbol{k}) = \frac{A}{N_A} I(t = \frac{1}{2}, \boldsymbol{k}) \tag{2.30}$$

where

$$I(t, \boldsymbol{k}) = \int W(\boldsymbol{R}) X(t, \boldsymbol{k}, \boldsymbol{R}) \mathrm{d}\boldsymbol{R} \tag{2.31}$$

where

$$\boldsymbol{R} = \boldsymbol{r}'_1 \boldsymbol{r}_1 ... \boldsymbol{r}_A \tag{2.32}$$

and

$$W(\boldsymbol{R}) = \prod_{i<j} f^c(\boldsymbol{r}'_{ij}) f^c(\boldsymbol{r}_{ij}) \tag{2.33}$$

and

$$X(t,\boldsymbol{k},\boldsymbol{r}) = \phi_A^+ M_A^+(\boldsymbol{r}_1',...,\boldsymbol{r}_A) P_t(1) e^{i\boldsymbol{k}\cdot(\boldsymbol{r}_1'-\boldsymbol{r}_1)} M_A(\boldsymbol{r}_1,...,\boldsymbol{r}_A)\phi_A \tag{2.34}$$

By folding together two single-nucleon momentum density distributions obtained by this method, the pair momentum distribution $F(P)$ can be obtained.

2.4 Phase Space Models for ^{4}He (γ,pn) reactions

It would appear from past experimental work that the quasideuteron model is likely to be suited to predicting photonuclear strengths at intermediate energies. Theoretical calculations have been discussed relating to this model for simple harmonic oscillator wavefunctions and Variational wavefunctions. However in order to test the validity of these models it is useful to compare the results with predictions from the available phase space alone. This can be done by considering the situation where the available centre-of-mass energy is distributed among the final state particles according to the densities of final energy states. The three body phase space predicts [68] that if the energies of two of the three particles are plotted on perpendicular axes, the density of events per unit area should be uniform within the permitted kinematic region.

If C is the total kinetic energy available to the three final state particles in their mutual centre-of-mass frame, then

$$C = T_p + T_n + T_R \tag{2.35}$$

where T_p, T_n and T_R are the kinetic energies of the proton, neutron and recoil

system respectively. In the non-relativistic limit,

$$\frac{m_R}{m}T_R = T_p + T_n + 2\sqrt{T_pT_n}\cos\theta_{pn} \tag{2.36}$$

where m is the nucleon mass, m_R is the recoil mass and θ_{pn} is the angle between the proton and the neutron in the centre-of-mass frame.

if we define T_D as

$$T_D = T_p - T_n \tag{2.37}$$

then

$$(C - T_R)^2 - T_D^2 = (T_p + T_n)^2 - (T_p - T_n)^2 \tag{2.38}$$

or

$$(C - T_R)^2 - T_D^2 = 4T_pT_n \tag{2.39}$$

rewriting equation 2.36 in terms of T_R and T_D,

$$\frac{m_R}{m}T_R = C - T_R + [(C - T_R)^2 - T_D^2]^{1/2}\cos\theta_{pn} \tag{2.40}$$

or

$$T_D^2 = (C - T_R)^2 - \frac{1}{\cos^2\theta_{pn}}\left((\frac{m_R}{m} + 1)T_R - C\right)^2 \tag{2.41}$$

For a given value of T_R, T_D has its maximum value when

$$\cos^2\theta_{pn} = 1 \tag{2.42}$$

thus

$$T_D^2 = (C - T_R)^2 - [(\frac{m_R}{m} + 1)T_R - C]^2 \tag{2.43}$$

marks the maximum and minimum possible values of T_D for a given value of T_R. This can be re-written as the equation of an ellipse with semi-major axes a and b,

$$\frac{T_D^2}{a^2} + \frac{(T_R - b)^2}{b^2} = 1 \tag{2.44}$$

where $a = C[m_R/(m_R + 2m)]^{1/2}$ and $b = C[m/(m_R + 2m)]$

Since T_D and T_R are simply linear combinations of T_p and T_n, a plot of T_D versus T_R should yield an ellipse of uniform event probability density whose boundaries are given by 2.44.

The probability of having a value of T_R between T_R' and $T_R' + \mathrm{d}T_R$ is thus proportional to

$$2T_D^{max}\mathrm{d}T_R = 2\sqrt{(C - T_R)^2 - [(\frac{m_R}{m} + 1)T_R - C]^2}\mathrm{d}T_R \tag{2.45}$$

rewriting $T_R = p_R^2/2m_R$ and $\mathrm{d}T_R = p_R\mathrm{d}p_R/m_R$ we can show [19] that for a given available energy, C, the probability of the recoil system's momentum lying between between p_R and $p_R + \mathrm{d}p_R$ is proportional to

$$p_R^2(1 - p_R^2\frac{m_R + 2m}{4Cmm_R})^2\mathrm{d}p_R \tag{2.46}$$

2.5 Conclusion

The present work should provide evidence as to how appropriate the quasideuteron model is in describing the ^{4}He nucleus. A direct comparison between quasideuteron and phase space model predictions with experimental data should give a good indication of the validity of the quasideuteron approach.

Certainly final state interaction effects will distort the picture somewhat but it is likely that these effects will be small as far as the detected nucleons are concerned.

The quasideuteron model appears to dominate in the intermediate energy region, however this model may be unable to explain photonuclear strengths in some regions of phase space, where 3-N absorption mechanisms are observed to be significant. This effect may be significant even on the relatively low density ^{3}He nucleus, where it may account for 10-20 % [69] of photonuclear reactions in this case. 3-N absorption mechanisms also seem to be strong in ^{4}He at photon energies of $\sim$400 MeV [46, 47]. The ^{4}He nucleus, being of much higher density, might be expected to be noticeably affected by such mechanisms, which would tend to share the photon's energy between 3 nucleons, thus destroying N-N angular correlations in these reactions. However, experimental data on ^{3}H and ^{3}He are relatively sparse, and quasi-3-nucleon models in analogy with the quasideuteron model are difficult to test at the present time.

Both 3-nucleon interactions and final state interactions would be expected to contribute to the (γ,pp) channel, whereas pure quasideuteron interactions should not. It is hoped that the present measurements will provide some indication of the mechanisms responsible for this photodisintegration channel.

Chapter 3

The Experimental System

3.1 An Overview

The data presented in this thesis were obtained from photodisintegration measurements on ^{4}He, which were carried out using the tagged photon facility at the Mainz 180 MeV electron microtron MAMI-A, in February and August of 1987. The experimental apparatus was configured in such a way that for every (γ,NN) event that was recorded, the apparatus would determine the energy of the photon, identify the two particles detected from the reaction, and measure their momenta. This chapter contains a description of the apparatus which was used during those measurements. Details of each piece of apparatus are given as well as information on the electronics and signal processing.

An overview of the experimental system is given in figure 3.1. At the bottom of the picture, the incoming electron beam provided by the Mainz 100% duty-cycle microtron is shown. The 183 MeV electron beam is directed onto an aluminium radiator to produce bremsstrahlung photons, which are tagged in a QDD (quadrupole-dipole-dipole) magnetic spectrometer [3].

The tagged photons are incident on a liquid ^{4}He target, where nuclear reactions

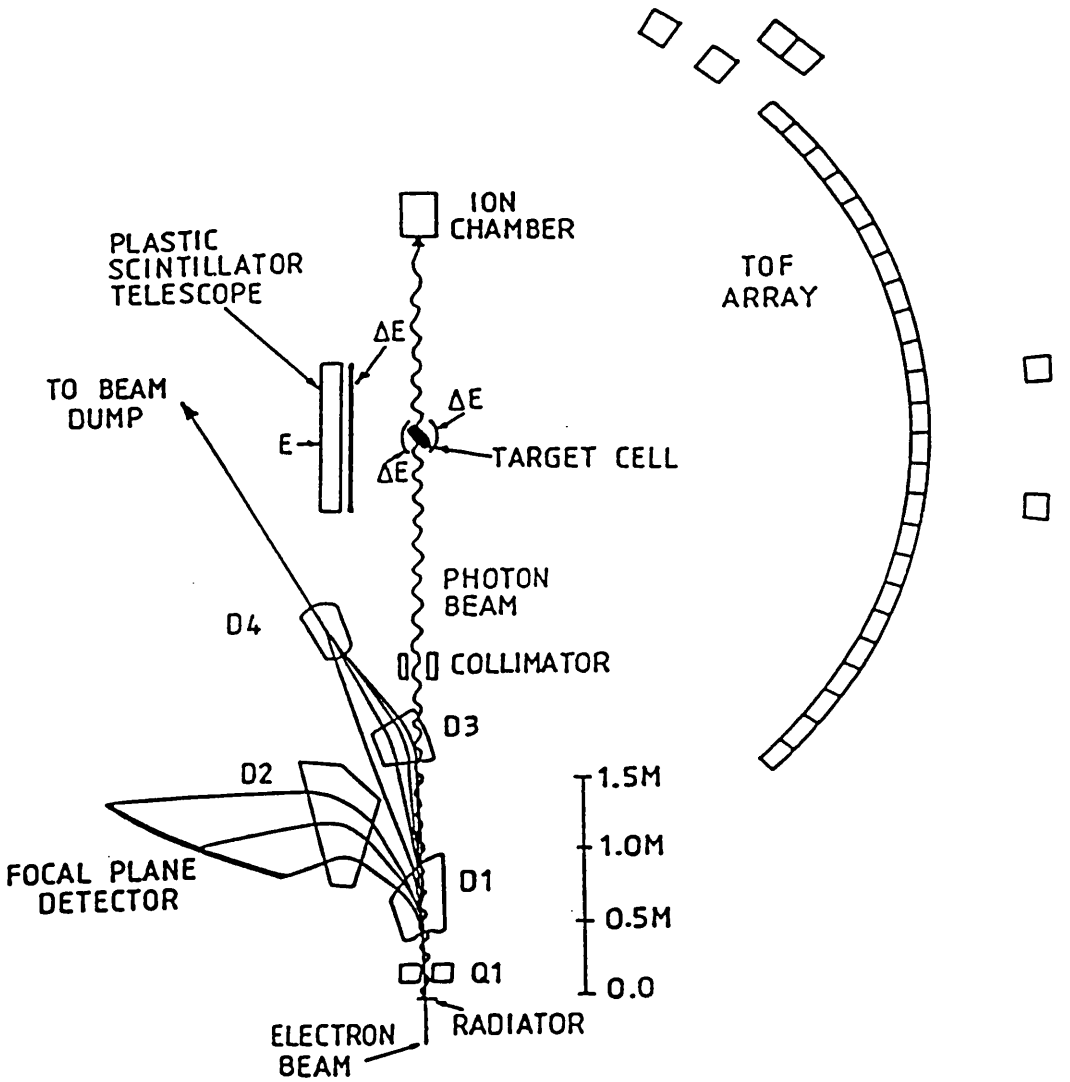

Figure 3.1: Schematic diagram of the experimental system.

cause nucleons to be ejected. The ejected particles are observed by the two detector arrays situated on either side of the target. The detectors are of large solid angle, and have good angular and energy resolution, enabling a full identification of the breakup channels. On the left side is shown a ΔE,ΔE,E telescope which is used to detect and identify protons and deuterons. On the right is a TOF array, which can detect and identify neutrons, protons and deuterons. The ΔE,ΔE,E telescope had horizontal and vertical position sensitivity, which is used to determine the polar and azimuthal angles of one of the detected particles. The TOF detectors situated on the other side of the target measure the vertical position and timing of other, correlated particles. By knowing which TOF detector produces a signal the particle's horizontal position is determined with good accuracy. The curved ΔE detectors register charged particles only, and the TOF-side curved ΔE is used in conjunction with the TOF detectors to separate TOF-side protons and deuterons from neutrons.

3.2 The Accelerator

The racetrack electron microtron [72],[2],[71], illustrated in figure 3.2, was used to provide the continuous electron beam for this experiment. The accelerator consists of a Van de Graaf injector followed by two electron microtron stages which are used to accelerate the electrons to ~180 MeV using a 2.45 GHz r.f. field.

The Van de Graaf injector produces electrons of 2.1 MeV energy, which are injected into stage 1 of the microtron where they are circulated between two large magnets in orbits of gradually increasing size. In each turn, the electrons pass through the same accelerating section situated between the magnets. There are a total of 14 turns in this stage after which the electrons are accelerated to 14 MeV. The electrons then enter stage 2 where they are accelerated through 51 turns to

reach an energy of 180 MeV. At the last turn an extractor magnet is used to deflect the beam into the beam handling system which subsequently guides it to the bremsstrahlung radiator.

The r.f. field used to accelerate the electrons also acts to equalise their energies. Electrons of energies that are too high take a slightly longer time to arrive once again at the accelerating field, as they take a longer flight path through the magnets. They are then slightly out of phase with respect to the accelerating field and so are not accelerated by as much as electrons of the correct energy. Similarly, electrons whose energies are too low are over-accelerated on subsequent passes through the accelerating section. This feed-back mechanism leads to the production of a beam with a resolution of 36 keV FWHM, suitable for use in the photon tagging experiment.

3.3 The Tagging Spectrometer

The focussed electron beam provided by the microtron passes through an aluminium radiator to produce strongly forward-peaked bremsstrahlung. The small proportion of the beam electrons which interact with the radiator to produce bremsstrahlung also lose energy in the process. These electrons degraded in energy are focussed by a quadrupole magnet, Q1, shown in figure 3.1 and by two dipole magnets, D1 and D2, onto the focal plane of the tagging spectrometer shown to the left of D2 on the diagram. D1 and D2 each have field homogeneities of better than 5 parts in 10^4 [3].

The quadrupole magnet, Q1, provides vertical focussing for the electrons while the two dipole magnets, D1 and D2, give horizontal focussing. The position on the focal plane at which a given electron arrives depends only on its energy, therefore to determine the electron energy only the position of the electron on the focal plane needs to be recorded. By determining the energy of an electron, the energy of the

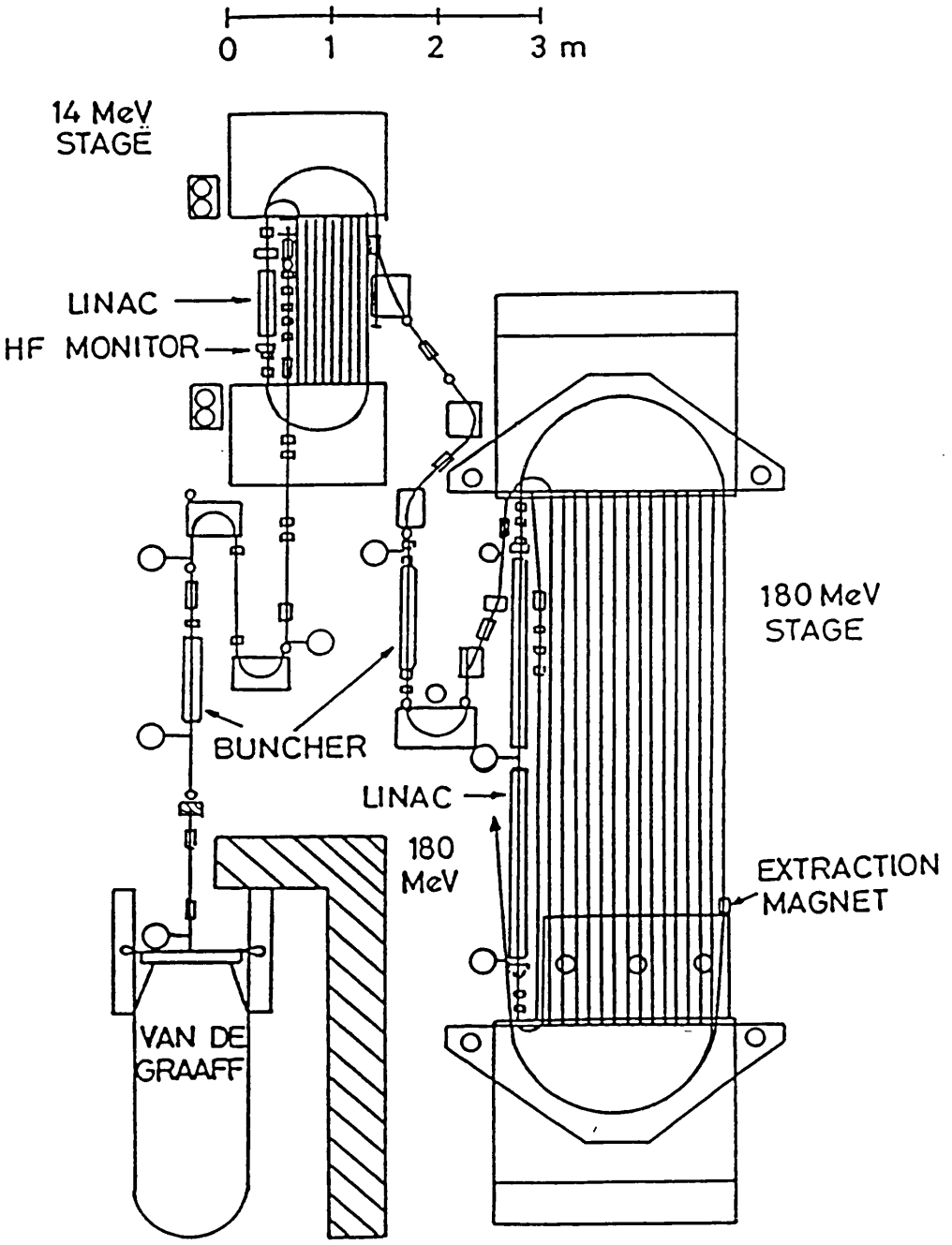

Figure 3.2: The accelerating stages of MAMI-A

corresponding bremsstrahlung photon is calculated as the difference between the incident electron beam energy (182.95±0.02 MeV) and the energy of the electron detected at the focal plane. It is through measuring the energy and timing of the focal place electron that the photon is tagged.

The momentum acceptance of the analysing magnet is large, so that the lowest momentum accepted (for a given magnet setting) is roughly half of the highest. Four magnet settings were normally used, leading to four trajectories for the electron beams, which allow for a wide range of electron energies, and hence photon energies, to be tagged. In this experiment, however, only trajectories 1 and 2, which gave the widest photon energy coverages, were used. The range of photon energies covered by each trajectory is shown in table 3.1. Magnets D3 and D4 serve to transport the undegraded electron beam away from the experimental area.

The electrons which arrive at the focal plane are detected by a position sensitive focal plane detector (FPD) [3] which consists of an array of 92 scintillator detectors. These detectors overlap one another so that for every useful event, at least 2 adjacent scintillators produce a signal. There are 91 coincidence output channels from this array, each corresponding to a particular pair of neighbouring detectors. The output channel number, which determines the tagged photon energy, is recorded in a bit pattern unit by the computer for every recorded event. The timing of each event is recorded by combining the outputs of groups of 8 channels and feeding them to 12 TDC's (the first and last TDC's are exceptions taking the inputs from only four and seven channels respectively). The TDC's record the timing of the electron relative to the timing of the reaction trigger, called the X-trigger, which is determined by the timing of the particle detected on the proton side curved ΔE detector.

The principal advantage of splitting the FPD into 12 sections was that events

Trajectory	From	To
1	80	131
2	131	155
3	155	167.5
4	167.5	173.75

Table 3.1: Table of photon energy ranges (MeV) tagged for each trajectory

corresponding to a given TDC could be treated separately from most of the others. This technique improved the ratio of real to random coincidences considerably over that obtained using a single TDC for all 91 channels. This in turn reduced the correction factors (and their associated errors) to the data, as described in section 4.3.1.

The photon energy resolution was essentially determined by the energy acceptance of each focal plane detector. This was ~0.5 MeV for the 80-131 MeV photon energy range.

3.3.1 The Beam Monitor

In order to monitor the photon flux incident on the target, a beam monitor was used in the measurement. An ionisation chamber was used to measure on-line, via a ratemeter, the instantaneous value of the total photon beam intensity. It also recorded the integrated photon beam intensity for each data set. This monitor was situated in the photon beam beyond the target, and was large enough to intercept the full collimated beam.

If the electron beam was unstable this would be reflected in a change in the photon beam intensity and hence in the monitor count rate, and the electron beam would then be re-aligned. In addition to the photon beam monitor, a Faraday cup

was used to monitor the electron beam current, which was displayed in the control room. A typical beam current for the tagged photon experiments was ~50 nA.

3.3.2 The Radiator

The choice of the bremsstrahlung radiator is a compromise. Too thin a radiator leads to a poor photon flux compared to the background produced by the primary beam flux. Having a radiator which is too thick will lead to multiple electron scattering leading to a broader bremstrahlung cone and a lower tagging efficiency. The radiator used, 25 μm of aluminium (2.8×10^{-4} radiation lengths), was a good compromise between these two effects.

The radiator is mounted on a wheel and is controlled electronically by a stepping motor. For tagging efficiency background corrections, as described in section 3.3.3, the radiator is removed using the electronically controlled wheel.

3.3.3 The Tagging Efficiency Measurements

The beam was collimated to discard the low intensity tails of the bremsstrahlung cone and define the photon beam spot size of 23 mm diameter at the target position. This permitted targets of small size to be used. The profile of the beam accepted by the collimator was recorded photographically several times during the experiment. A typical beam photograph is shown in figure 3.3. Because the beam was collimated, a substantial fraction of the photons produced at the radiator were stopped before reaching the target. Therefore not all of the electrons detected in the FPD corresponded to photons incident on the target. Tagging efficiency measurements were performed to ascertain the proportion of the electrons incident on the FPD for which the corresponding photons were incident on the target. These measurements

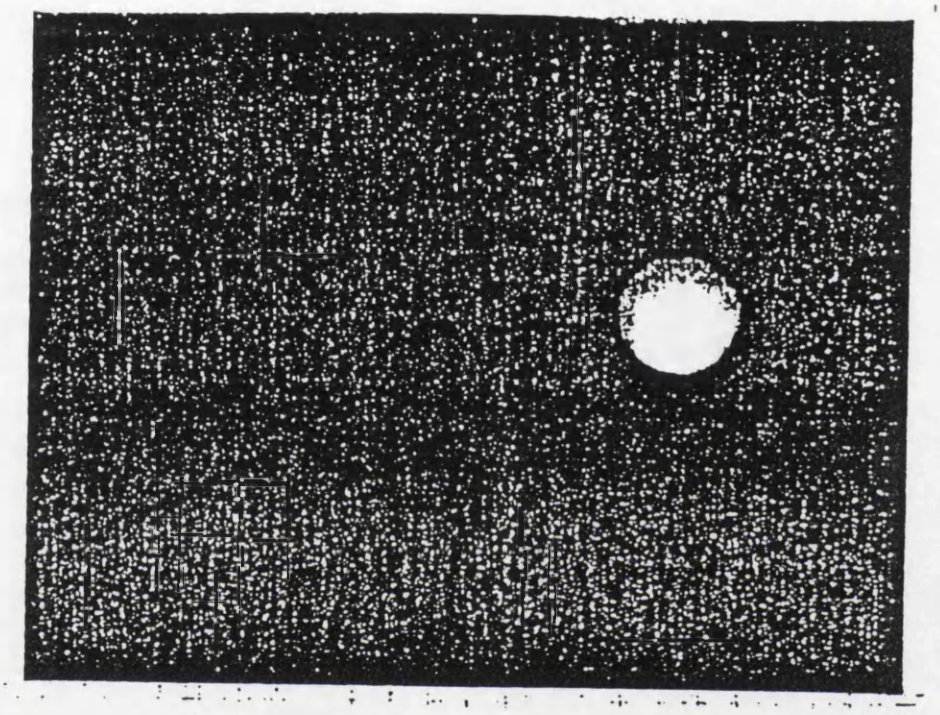

Figure 3.3: A photograph of the tagged photon beam emerging from the collimator

used a scintillating glass detector of 100% photon detection efficiency in coincidence with the FPD. To measure the tagging efficiency, the electron beam was set at low intensity and the scintillating glass detector was placed in the position normally occupied by the target. The number of photons detected was compared with the number of electrons in the tagging spectrometer and the ratio was calculated to give the tagging efficiency. In fact, two measurements were taken, one with the radiator in place, and the other with the radiator absent. This allowed corrections for background. The tagging efficiency is a weak function of photon energy because the divergence of the photon beam is a function of energy. This effect may in principle be partially corrected for at the analysis stage, but in practice the variation with photon energy was found to be very small and was neglected.

3.4 The ΔE,ΔE,E Scintillator Array

The ΔE,ΔE,E array[4] shown schematically in figure 3.4 consists of 3 horizontal blocks of plastic scintillator, each of height 13.5 cm, depth 11 cm, length 1 m and with a refractive index of ~1.5. These E blocks (made of NE110) are of sufficient thickness to stop protons of energy up to 120 MeV. Immediately in front of the E-blocks are 5 vertical plastic scintillator strips, each 3 mm thick, 50 cm in height and 20 cm wide. Another, smaller ΔE transmission scintillation detector, described in section 3.5 is placed 10 cm from the target. A photo-multiplier tube (PMT) is attached to both ends of each E block and via twisted strip adiabatic light guides, to both ends of each ΔE strip. Each PMT is connected to an ADC and to a TDC, each of which are read by the computer for every event that is recorded. The horizontal and vertical positions of the detected particle are determined off-line from the time differences between the TDC signals at the ends of the scintillator block or strip.

From the calculated position, the scattering and azimuthal angles are determined for the particle detected. The energy of the proton (or deuteron) is determined from the light output of the scintillator. As is explained in section 4.1.3, the geometric mean of the light intensities detected at the ends of an E block is related linearly (to a very good approximation), to the energy deposited in the detector. Thus the ΔE,ΔE,E array is used to measure the energy and direction of an identified particle.

A charged particle passing through the scintillators will lose kinetic energy at a rate determined by the Bethe-Bloch formula [73] and this loss rate $\left(\frac{dE}{dx}\right)$ is determined almost entirely by the particle velocity and is not sensitive to the mass of the particle. Thus a particle may be identified by examining the relationship between the signal in the E block, related to its energy E, and the $\left(\frac{dE}{dx}\right)$ signal in the ΔE strip, related to its velocity, as shown in figure 4.5. The detector can be used to differentiate between electrons, protons and deuterons.

The useful detector aperture was limited, since for particles arriving close to one end of an E block, the PMT light collection was strongly position dependent. This resulted in poor energy resolution for such particles and they were therefore discarded from the data. Particles incident near the ends of the ΔE-strips were also discarded since they can emerge from the top and bottom surfaces of the E-blocks if their energy is sufficiently high. A scatter plot of the horizontal and vertical positions of incident particles is shown in figure 3.5, the dashed lines indicating the cuts used. With these cuts the useful solid angle subtended by the detector was 0.89 steradians.

The effective energy threshold of the detector is determined by the particle energy losses in the two ΔE strips and the electronic threshold applied to the output from the E-block PMT's in order to eliminate noise and background. The effective

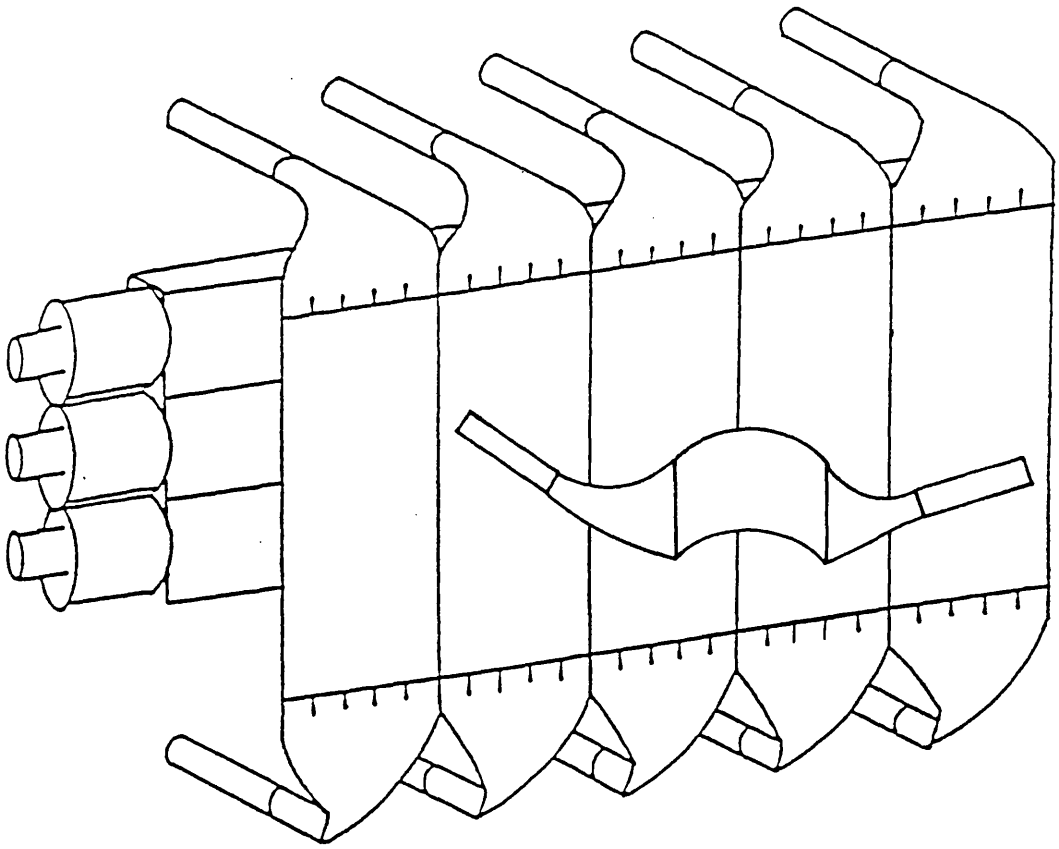

Figure 3.4: A Diagram of the ΔE,ΔE,E array

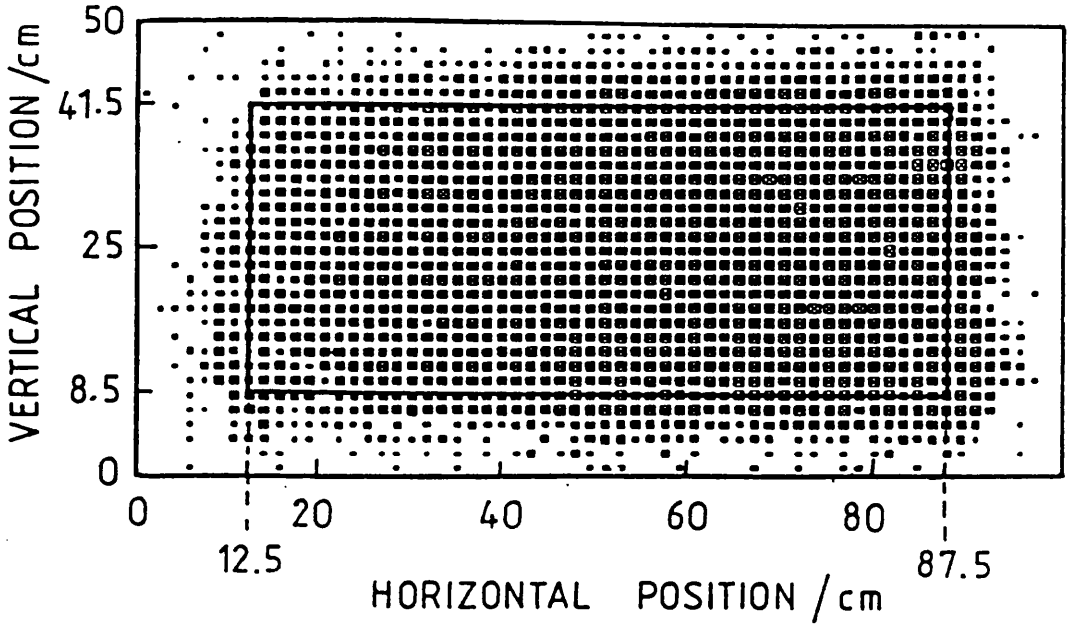

Figure 3.5: A scatter plot of the horizontal and vertical positions of particles detected by the ΔE, ΔE, E scintillator detector.

threshold for protons was dependent on the angle between the proton and the detector surfaces. This is because of the proton path length through the ΔE-strip being angular dependent. The proton detector threshold was 27.5 MeV at right angles to the detector surface, 30.4 MeV at the most forward angle and 29.0 MeV at the most backward angle.

In (γ,pn) data, it is of interest to detect particles from reactions corresponding to a wide range of missing energies (see appendix A.2). However reactions of high missing energies correspond to low energy protons and some of these protons have energies below the detector threshold. To minimise these losses, the discriminator thresholds on the ΔE,ΔE,E detector were set as low as possible The triple coincidence between the two ΔE layers and the E-blocks ensured that even with thresholds at minimum, the random background recorded was not excessive. This

threshold, however, was sufficiently high to present a significant limitation to the nuclear information which could be obtained, particularly at the lower photon energies and higher missing energies.

The ΔE,ΔE,E array incorporates light flasher units in the E blocks, to provide a reference light intensity. A feed back loop controlled by a PIN diode which monitored the light output from the flasher, was included to provide additional stability. The flasher signals were used to monitor PMT gain drifts occurring during the course of a measurement. The flasher peaks were invaluable online, since a flasher peak that is broad in energy indicates data in which the PMT gains are varying with time. However the flasher unit could not be used for accurate energy calibrations through monitoring small drifts in the detector gains, as the flasher unit output drifted very slightly every few hours due to minor instabilities in its pre-amplifier. Nevertheless the flasher units provided a useful check on the gain stability of the detector and approximate energy calibrations could be obtained, which determined the proton energy to within 2 MeV. This was useful in obtaining initial calibrations, although a more accurate technique was used to obtain the final calibrations.

3.5 The Curved ΔE Start Detectors

Two curved ΔE detectors were attached to the target scattering chamber. The proton side curved ΔE, forming part of the E,ΔE,ΔE array, was useful in online background rejection, and was used to determine the timing of the charged particle trigger. The TOF side curved ΔE was necessary for particle identification, to allow protons and deuterons to be differentiated from neutrons.

The curved ΔE detectors were made of NE102 and shaped to curve around the scattering chamber of the target. The scintillator was firstly manufactured as a flat

piece of plastic (1.1mm thick), and was bent to fit to the outside of the scattering chamber (radius of bend 9.5 cm) using hot water to soften it temporarily. It was desirable to position the ΔE's as close to the target as possible so as to determine best the timing of the particles ejected from the target. The curved ΔE detectors used fibre-optic cables at either end in order to collect the scintillation light efficiently, and transmit it to the two PMT's.

3.6 The TOF detector array

The time-of-flight detector array comprised 24 NE110 plastic scintillator blocks which were arranged vertically on the opposite side of the target to the ΔE,ΔE,E array. These detectors (described in reference [5]) were 1.8 m tall, 20 cm wide and 10 cm thick and were positioned 3 m from the target, covering an angular range of 43° to 137°. Their total solid angle at the target was ~1 sr. The detectors were position sensitive with a vertical position resolution of ~5 cm, corresponding to an azimuthal angle of ~0.6°. These detectors were used to observe the reaction product correlated with the particle recorded by the ΔE,ΔE,E array. For protons, the detection efficiency above the threshold energy was ~100 %, but for neutrons these detectors typically had an efficiency of 10-15 % depending on the neutron energy and the thresholds used. Each detector had 2 PMT's attached, one at either end, in order to provide both scintillator pulse height and timing information. Due to a shortage of available ADC's and TDC's, the 24 TOF detectors were multiplexed, where each detector was connected to a unique combination of ADC's and TDC's, with each ADC or TDC connected to four TOF-detector PMT's. By identifying which combination of ADC's and TDC's gave signals it was possible to deduce which detector received the particle.

A plot is shown in figure 4.9 of the pulse height geometric mean versus particle speed for this detector array showing how particle identification was possible.

3.7 The ^{4}He Targets

In order to achieve a satisfactory foreground to background ratio, experiments with ^{4}He targets normally require the helium to be contained at high density and there are two ways of achieving a ^{4}He target at high density, namely high pressure gas targets and cryogenic liquid targets.

Gas targets have some advantages over liquid targets. For instance they are particularly useful if the target thickness must be accurately ascertained. However, such a method method would be undesirable for this particular experiment as it requires target cell walls thick enough to withstand several atmospheres of pressure, leading to high energy losses for charged particles as well as creating high background levels from the target cell.

The other method, using liquid helium, allows the target cell walls to be thinner, but introduces other technical difficulties. Containment of a cryogenic target imposes difficulties due to heat radiation from the surroundings. The target must be suspended in vacuum and surrounded by heat shielding, but the heat shielding and vacuum containment must not interfere too greatly with the photon beam or with the outgoing particles. These problems are discussed in more detail in reference [13]. The experimental difficulties are mitigated slightly due to the large gas to liquid density ratio, this ratio being 700 for ^{4}He, which allows the liquid target to be made relatively small in volume. The target was $\sim$30 cm^3 in volume, with a thickness of $\sim$1 cm (0.125 g/cm^2) containing $\sim$3.2 grammes of liquid ^{4}He. The small size reduces the problems of containment, and reduces the amount of cooling neces-

sary. It also allows the point of interaction and therefore the particle trajectories to be well determined.

Kapton windows of thickness 120μm were used on both sides of the target cell in order to allow charged particles to pass through either side. The thin windows also reduced the background produced by the photon beam. The windows were supported by a 6 mm thick elliptical aluminium frame with an internal aperture with major and minor axes of 109 mm and 50 mm respectively. Unfortunately, charged particles could not escape at all angles owing to the presence of the vacuum chamber supporting walls (see fig. 3.6). Thus not all of the TOF detectors could be used for proton detection. In addition, the target cell was surrounded by heat shielding (5μm aluminised mylar) which also contributed to the background and energy losses.

Two different cryogenic systems were employed to produce liquid helium targets. The first was an open cryostat which simply contained liquid ^{4}He, which was allowed to boil off slowly, and was refilled periodically from a dewar. The second was a closed loop system which was isolated from the atmosphere, and was used to liquify gaseous helium, and could in principle be used for ^{3}He as well as ^{4}He. The former system was used for the lower photon energy range (80-131 MeV) and the latter was used for the higher energy range (131-150 MeV). Both of the targets used the same vacuum chamber. The plan of the scattering chamber is shown in figure 3.6

3.7.1 The Open Cryogenic System

The open cryogenic system for ^{4}He containment involved the use of a cryostat to supply the target cell continuously with fresh liquid helium. The boil-off helium gas

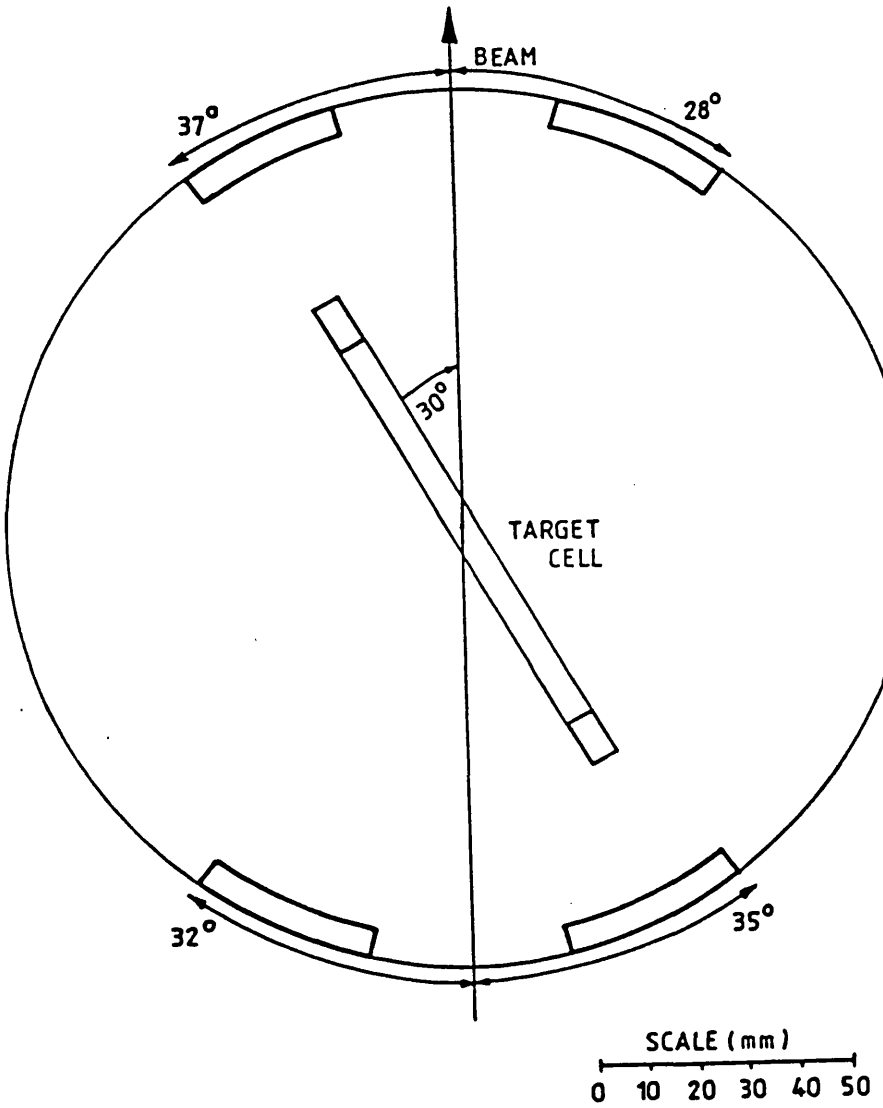

Figure 3.6: Plan of target used. The windows on the sides of the scattering chamber were not identical. They were set at different heights, which were chosen to match the heights of the detector arrays.

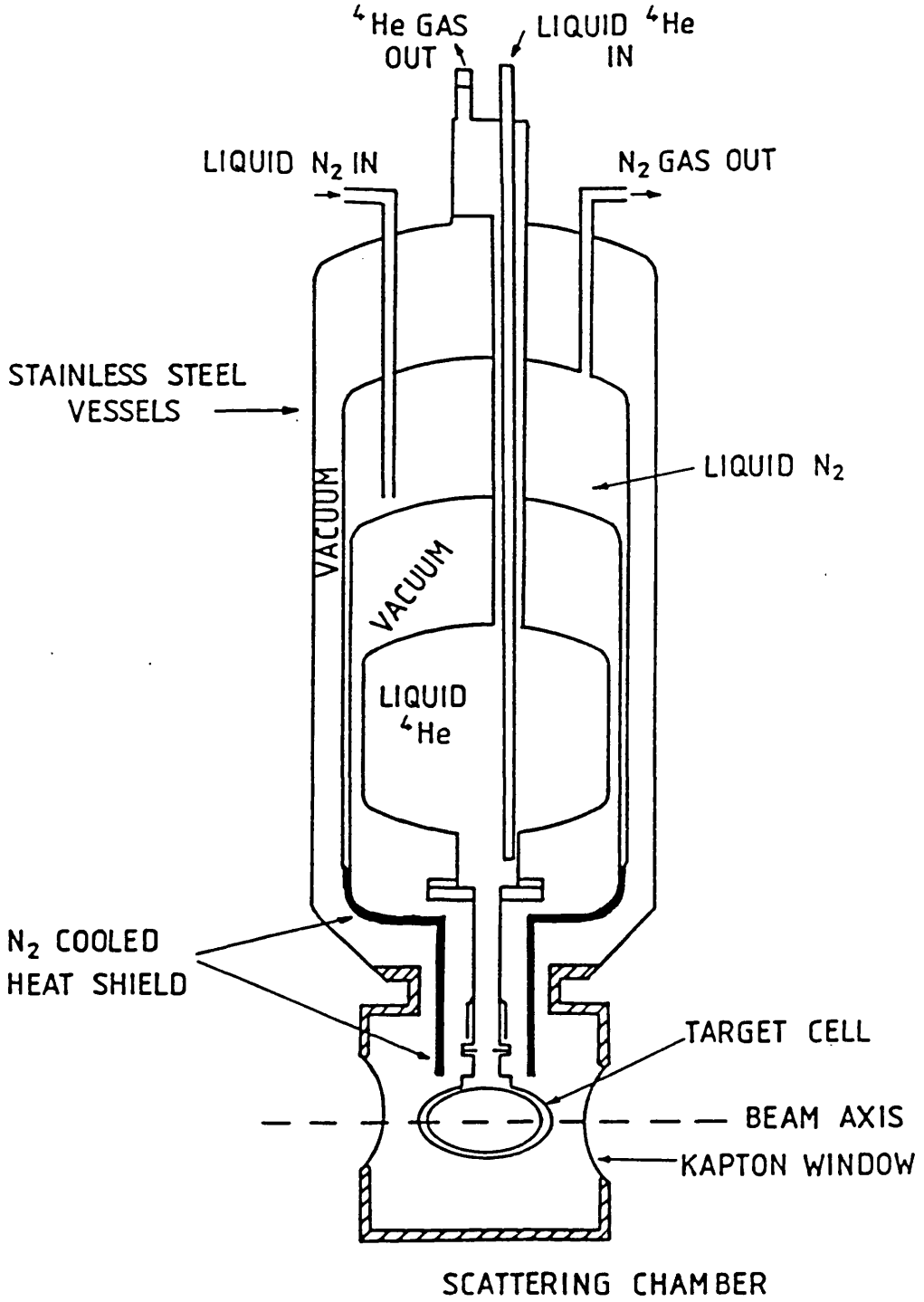

Figure 3.7: The Cryostat Liquid Target Arrangement

was vented to the atmosphere. The cryostat, shown in figure 3.7, acted as a temporary reservoir and required regular refilling with fresh liquid ^{4}He. The containment vessels above the scattering chamber were constructed of stainless steel, and the solid part of the target cell was made of copper. The apparatus was constructed so that a liquid nitrogen cooled screen would partially shield the liquid helium from heat radiation. The nitrogen-cooled heat shield was invaluable since it greatly reduced the heat radiation reaching the target from its surroundings (the radiation flux from material at that temperature compared to room temperature being about $\frac{(77K)^4}{(300K)^4}$, which is less than 0.5 %). This shield could only partially cover the target since it could not be placed in the path of the beam or outgoing particles. The pipework was constructed so that the heat conduction from the helium-cooled parts of the apparatus to the nitrogen-cooled parts was kept to a minimum. The supporting metal connection between the outer wall for the helium gas was made relatively high in the cryostat (see diagram), so as to minimise the heat input through conduction to the liquid helium in the inner tube. The pipework was designed to be strong, but thin so as to minimise heat conduction along the pipes, but allowing heat conduction between the inside and the outside of a pipe to allow heat exchange between the incoming and outgoing helium. The metal connection between the liquid nitrogen and the radiation shield, on the other hand, was made to be a good heat conductor in order to keep the shield cool. The vacuum compartments all communicated freely, the vacuum being maintained by a single turbo-pump (TMP) which was connected to the bottom of the scattering chamber via a wide aperture.

The target operated reliably. Only the quantity of liquid in the cryostat and the vacuum quality required constant attention and were monitored by closed circuit T.V. cameras viewing the relevant guages and meters. The amount of liquid helium in the cryostat above the target was estimated from the resistance of a wire immersed

within the helium, which was superconducting only if submerged within the liquid. A small current was passed through the wire to prevent that part of the wire above the surface from becoming superconducting as well. When the liquid level fell below a predetermined value, the experiment was stopped for 15-20 minutes to allow refilling. This was required at ~5 hourly intervals.

3.7.2 The Closed Cryogenic System

The second method of helium containment employed a closed (isolated from atmosphere) system where the gas was liquified through the iso-enthalpic Joule-Kelvin expansion induced by passing the gas through an adjustable needle valve. The Joule-Kelvin expansion only gives a cooling effect below 40K for ^{4}He, and this cooling is only significant below ~10 K (see figure 3.8). Pre-cooling the ^{4}He was therefore necessary using two compressor-operated cold heads (which used expansion of ^{4}He gas at high pressure to provide cooling). The ^{4}He feed-pipe was soldered to the cold heads so as to form a thermal contact, where the cold heads were designed to cool the ^{4}He to 10 K.

A schematic diagram of the system is shown in figure 3.9. The helium was liquified in the refrigerator and deposited in the 25 cm^3 target cell housed within the vacuum. The refrigerator incorporated about 10 metres of miniature coaxial pipework, of minimum diameter 1 mm, which acted as counter-flow heat exchangers. This pipework had numerous soft solder joints which were exceptionally delicate and required extensive leak-testing.

The cooling of the target took place in two stages. Firstly the helium gas was passed through with the needle valve fully open until the needle valve temperature was close to 10K (the gas-to-target-cell pipe makes contact with the cold heads), at

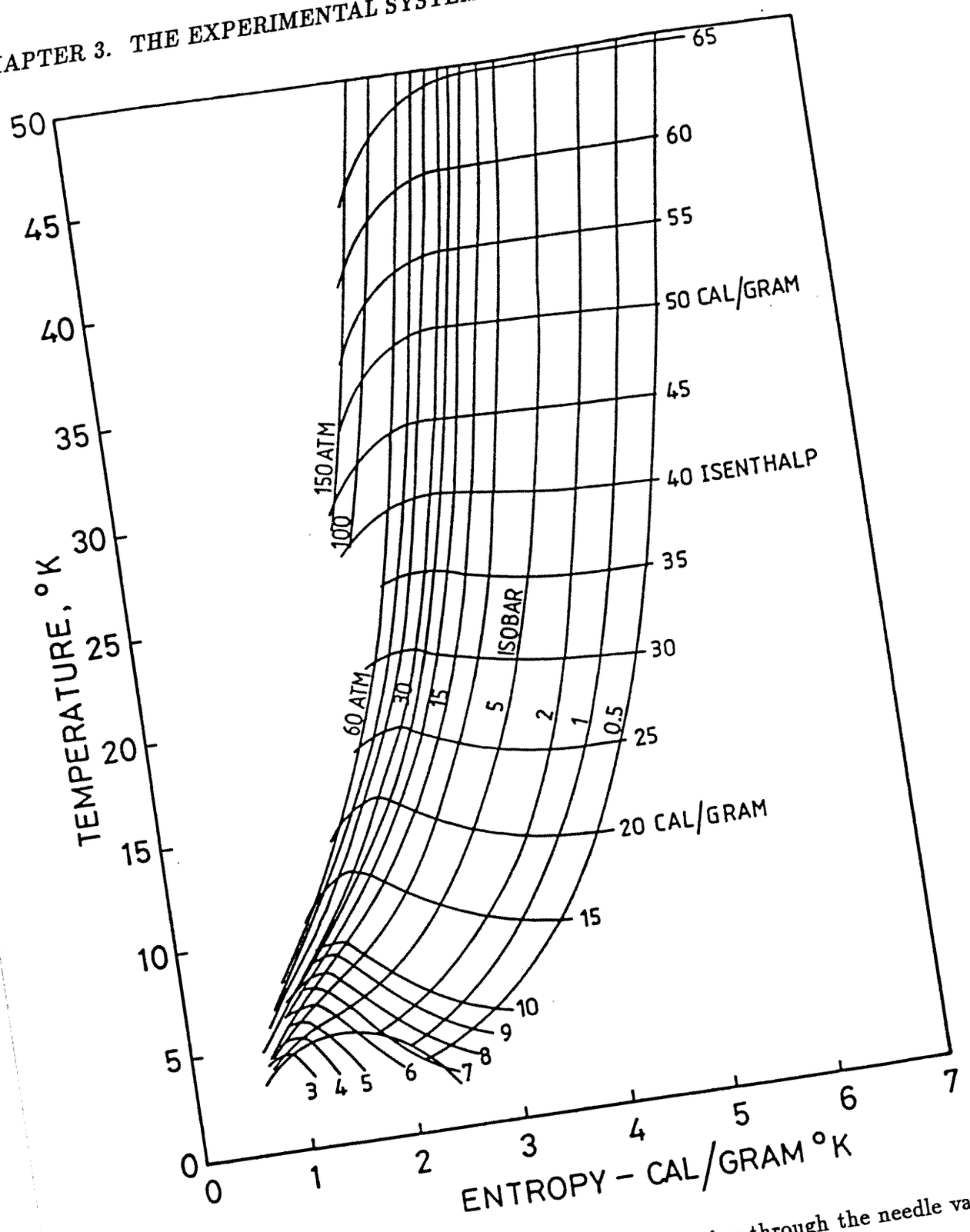

Figure 3.8: Entropy-Temperature Graph for ^{4}He. Passing through the needle valve is equivalent to moving to the right along an iso-enthalpic curve

which point the Joule-Kelvin effect would be powerful enough to cool it still further. Once the target and pipework had cooled sufficiently, the needle valve was closed so that the Joule-Kelvin effect came into operation. Between the 10K cold head and the target a counterflow heat exchanger cooled the gas to ~3K. The adjustment of the needle valve was optimised with the help of several temperature monitors which were located on various parts of the apparatus. It also contained pressure monitors to monitor the pressure within the target cell (strain guage), and in the target vacuum chamber (pirani guage). The pressure differential across the needle valve and the gas flow rate were controlled electronically.

During operation, since the helium cell could not be seen due to the heat shielding, the only reliable way to ascertain how much liquid helium was in the target cell was to estimate the amount of gas which had condensed and and hence been lost from the gas phase. Knowing the density of liquid helium the volume of liquid in the target cell could then be estimated. The system also included electronic safety features such as one to automatically return the gas to the buffer in the event of failure of the cell windows or vacuum, or a blockage of the needle valve. The gas return would be induced if a poor vacuum was recorded in the scattering chamber by the pirani guage. In addition, the system was configured so that all of the helium was recovered at the end of the experiment.

The system was developed for use with a ^{3}He target, but in the event was used for a measurement on ^{4}He at the higher photon energy range, $E\gamma = 131 - 155$ MeV. A diagram of the external part of the refrigeration system is shown in figure 3.10.

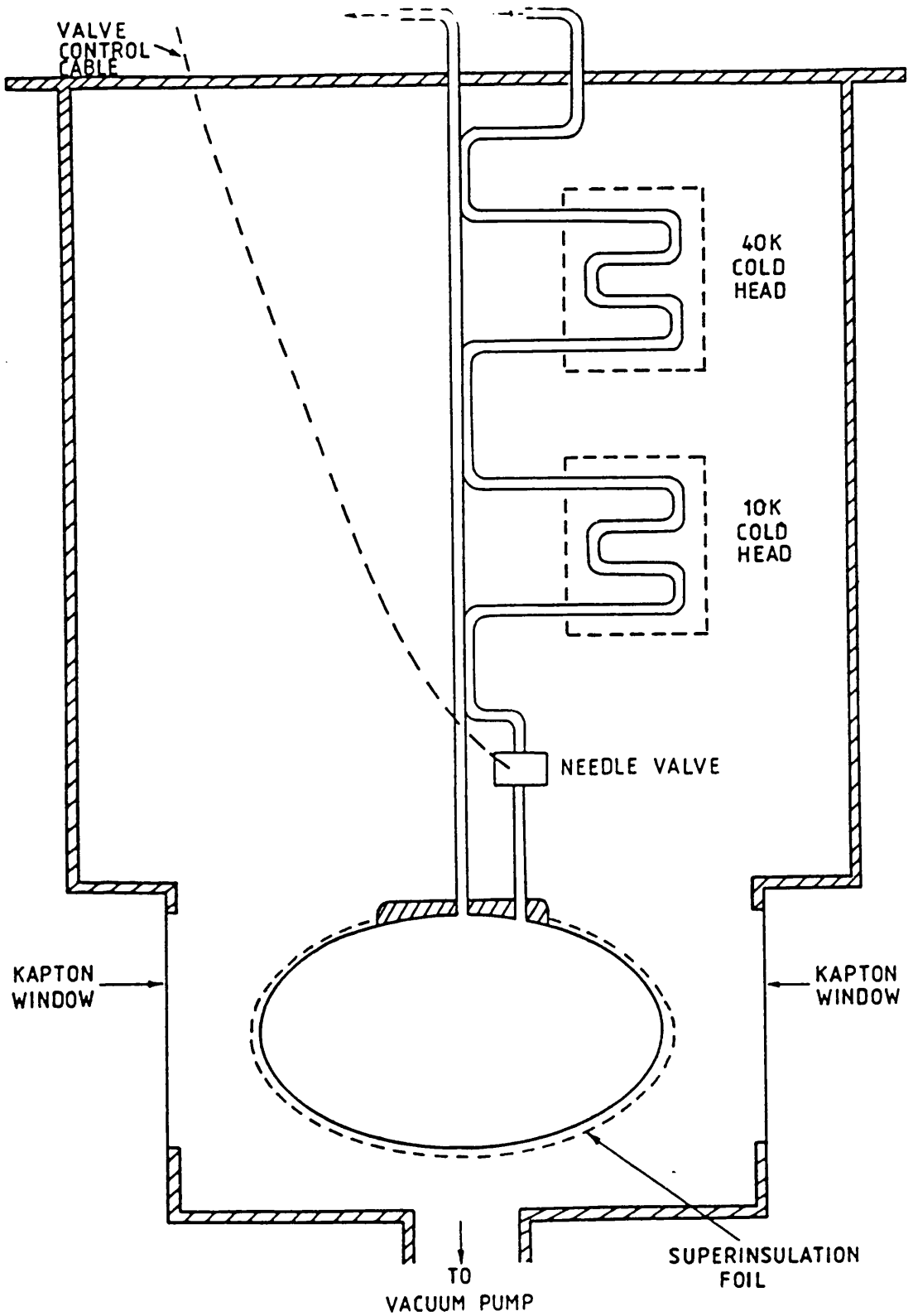

Figure 3.9: A schematic diagram of the helium liquifier. In the apparatus used, the right-hand pipe is contained within the left hand pipe (concentric) whereas they are shown alongside one another in this diagram.

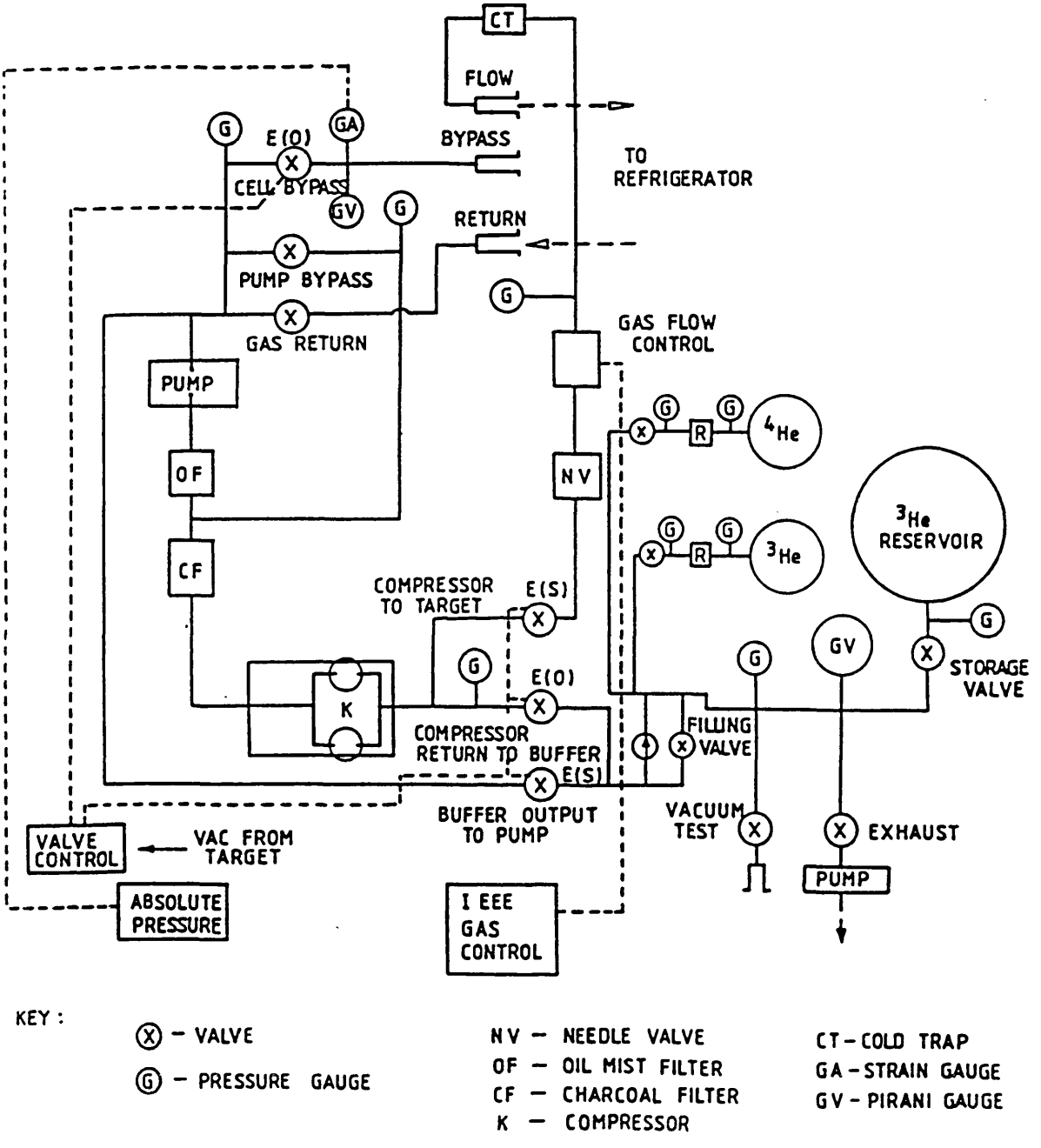

Figure 3.10: The exterior parts of the refrigeration system

3.8 The Online Datataking

The electronics were configured in such a way that for an event to be recorded as part of the experimental data, the system required a signal in both the charged particle detector array (ΔE,ΔE,E array) and in the tagging spectrometer. When an event was recorded, the signals from the charged particle array, the tagging spectrometer, the TOF array and the TOF side curved ΔE detectors were recorded by the computer.

3.8.1 The Data Accumulation System

The particle detection apparatus consisted of three detector arrays. The first detector array was the tagging spectrometer, which was described in section 3.3. The second detector array was the ΔE, ΔE, E array, described in section 3.4, and the third was the TOF-detector array, described in section 3.6. An event was recorded when a suitable signal activated the ΔE, ΔE, E array in coincidence with an event in the FPD. The coincidence time window used was 30 ns wide to allow both random and true coincidences to be recorded. In order to minimise the potentially large number of events which could be generated by electrons creating random coincidences, an online electron veto was used in the ΔE, ΔE, E array (see fig. 3.11). One of the E-blocks, one of the ΔE-strips and the curved ΔE were each required to give a signal above their respective thresholds, and an additional condition had to be met. For this condition, the signals from all 6 scintillator block PMT's were added together and the resulting signal was attenuated by a variable amount. Similarly the signals from all of the vertical ΔE strips were added together and attenuated. The attenuated E and ΔE signals were then added together, and the signal resulting had to exceed a separate threshold as an additional condition on the X-trigger. This procedure resulted in a diagonal cut on a E-ΔE plot of the recorded events the position

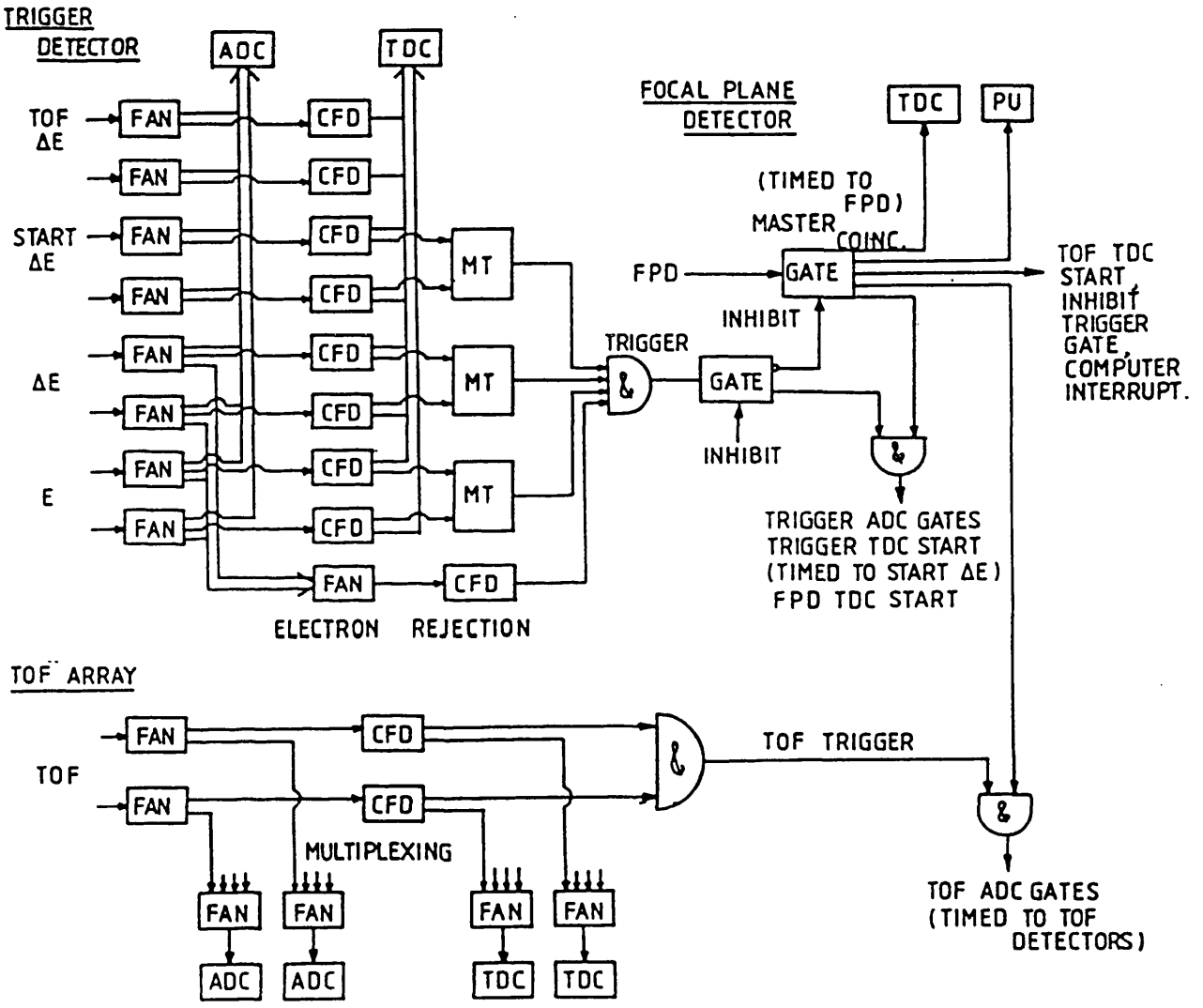

Figure 3.11: A diagram of the coincidence electronics, PU: pattern unit, CFD: constant fraction discriminator, MT: mean timer.

of which could be controlled by the two attenuation factors. Most electrons were eliminated in this way. When the X-trigger was activated, in coincidence with an event in the focal plane detector, an event was recorded by the computer. At this point, the signals from all of the CAMAC ADC's and TDC's were passed through an HP1000 computer where the information was encoded, and transferred via a swinging buffer to an HP3000 computer, where each event was written to tape.

A diagram of the overall electronic system is shown (figure 3.11). The timing of the experimental system was configured so that the particle timings were recorded relative to the FPD timing, because the FPD yielded better timing resolution than the curved ΔE of the E,ΔE,ΔE array. This was important for accurate TOF measurements. The TOF TDC's are started by the first signals from the FPD. Thus the TDC's are started with the electron (spectrometer) timing, and are stopped by the TOF TDC's.

The electron timing in the tagging spectrometer (taken relative to the X-trigger timing) was recorded because it could be used to distinguish accidental coincidences in which triggers were produced by untagged photons in random coincidences with FPD signals. The contribution due to such random events was subtracted from the yield due to prompt events. The timing of the TOF array was used for a randoms subtraction as well as for energy measurement and will be more fully expained in section 4.3.1.

During the datataking, a number of scalers were used to monitor the count rates. Two sets of scalers were used:-

- A set of scalers were used to monitor the total counts in each section of the FPD. This gave a measurement of the photon flux and hence an overall normalisation of the data. The contents of the scalers were recorded at the end

of each file to be used in the analysis off-line.

- Scalers were used to monitor the detection equipment and coincidence electronics. These could be used to give an immediate indication of any problems in the performance of the detectors or in the accumulation of data.

Chapter 4

Data Analysis

In this chapter the calibration of the apparatus and the reduction and analysis of the data will be discussed. The generation of spectra and the various corrections to the measured yield will be described. Finally the interpretation of the data by comparison with Monte Carlo (MC) models of the reaction mechanism will be described.

The experimental data were stored event by event on 1600 BPI magnetic tape, using an HP3000 computer. One recorded event contains the values of all of the non-zero ADC's, TDC's and PU's. The data sets which were taken comprised files corresponding to the target filled with liquid helium, the target empty, and various runs to allow the detectors to be calibrated off-line. At the end of each data set the numbers of counts which each scaler received during the data taking are recorded. The recorded ADC, TDC and PU signals, which originated from the detector arrays, could not be fully interpreted until they were calibrated off-line, using a purpose-written data analysis program. Once calibrated, the ADC and TDC signals were then used in the program to determine the momenta of the two detected reaction products, as well as that of the incoming photon, for each event recorded. The spectra obtained were corrected for background and random coincidence effects.

The calibrations and data event corrections which were carried out in the off-line analysis are discussed in some detail in the following sections.

The data taken in the course of this work covered two photon energy ranges, 80-131 MeV and 131-155 MeV. Due to instabilities in the microtron, however, accurate calibration of the 131-155 MeV dataset was not possible. Consequently the analysis presented here has been confined to the 80-131 MeV range over which accurate calibration was possible. The detectors used in this experiment had limited energy and angular acceptances and also had energy dependent efficiencies. The data recorded were thus modified by the response function of the apparatus. In order to fully interpret the data, therefore, it was necessary to perform a Monte Carlo simulation in order to understand and account for the distortions which the data suffered. A Monte Carlo program was already available for this purpose, but it required some modifications for use on these particular data. Details of the Monte Carlo simulations are given in section 4.5.

4.1 Detector Calibrations

4.1.1 Tagging Spectrometer Calibration

The photon energy depends on the incident electron energy and the energy of the degraded electron. The former was determined by the magnetic fields in the microtron end magnets. The latter depended on the tagged photon spectrometer magnetic fields and on the particular channel of the FPD which fired. In practice the magnet currents were set to predetermined values and monitored throughout the experiment. The photon energy could then easily be determined from a look-up table of E_γ against FPD channel.

4.1.2 ΔE,ΔE,E Array Position Calibration

The position of a particle on this detector array (shown in figure 3.4) was determined from the time difference of the signals at either end of both the NE110 E-block and the NE102A ΔE-strip which the particle entered. The position calibrations for the E-blocks were carried out by observing the E-block time difference spectrum, where the condition was imposed that a chosen ΔE-strip had to receive an event. This gave rectangular shaped time distributions with smeared edges as shown in figure 4.1. The time-positions corresponding to the edges of each ΔE-strip were estimated by looking at spectra from two neighbouring ΔE-strips as in figure 4.2. The TDC time difference values at half maximum for the two spectra were compared. The midpoint between the two half-maxima was taken to represent the boundary between the two ΔE-strips.

A similar procedure was carried out for the position calibration of each ΔE-strip using analogous conditions on the E-blocks, but with a small correction to take account of the ranges of the particles stopped in the E-blocks. This correction was included because in practice the light is not emitted at the surface of the E-block, but a short distance into the scintillator (due to the particle range). This therefore affected the position of the trajectory through the ΔE-strip. The penetration depth assumed was 2 cm for the 80-131 MeV photon energy range used. This assumed depth was based on the range corresponding to the average expected proton energies.

By knowing the physical positions and dimensions of the E-blocks and ΔE-strips, the position calibration was complete and the flight direction of any detected particle could be calculated. The position resolution was found to be 29 mm horizontally and 44 mm vertically [4]. In the data analysis, the determination of the particle's direction was uncertain due to the position resolution of the detector and

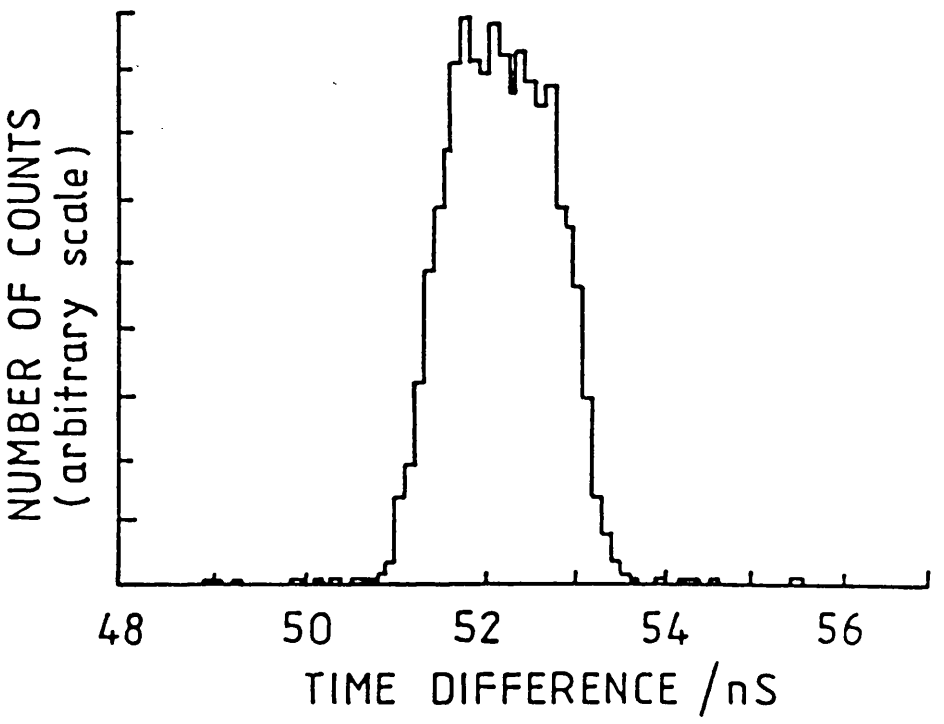

Figure 4.1: Time difference spectrum. The time difference between the signals from PMT's at either end of the ΔE-strip.

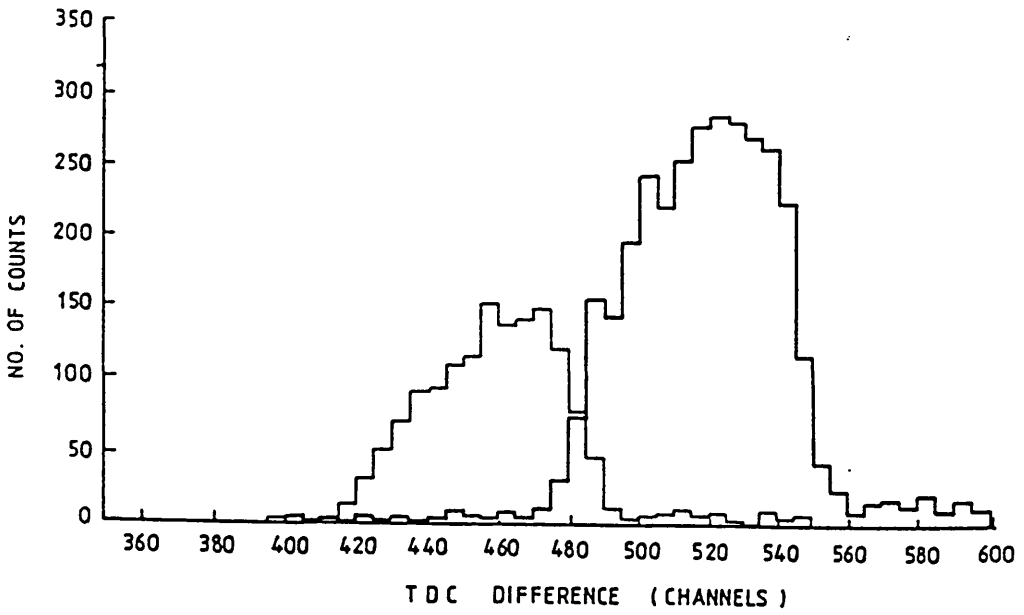

Figure 4.2: Calibrations: shows the ΔE-strip time difference spectra corresponding to two neighbouring E-blocks. The boundary was assumed to be at the midpoint between the two time-positions corresponding to the half maxima.

also because it is not possible to determine from what point on the beamspot at the target that the particle had originated. Taking both of these effects into account the angular resolution was estimated to be of the order of 0.1 rad.

4.1.3 ΔE,ΔE,E Array Energy Calibration

When a charged particle passes through a scintillator, light is emitted as the particle is slowed down. The total amount of light emitted is dependent on the mass, charge and kinetic energy (KE) of the particle. The method of determining the KE of a particle is complicated by the fact that the emitted light is attenuated by the scintillator. However, the attenuation is exponential to a good approximation, thus the light intensity at the end of a scintillator element is

$$I = Le^{-Kx} \tag{4.1}$$

where L is the initial light intensity, x is the distance traversed by the light and K is a constant for the scintillator elements. If the length of the scintillator is l, and the particle is incident at a distance x from end 1, and the intensities at both ends are I_1 and I_2, then the geometric mean of these is $\sqrt{I_1 I_2}$ where

$$\sqrt{I_1 I_2} = L e^{-Kx/2} e^{-K(l-x)/2} = L e^{-Kl/2} \tag{4.2}$$

which is position independent. Thus, assuming an exponential attenuation, the kinetic energy will be simply related to the geometric mean of the light signals at the PMT's on the E-blocks.

The particle's KE (T) is related to the light intensity L by

$$L = T - k \ln\left(1 + \frac{T}{k}\right) \tag{4.3}$$

where $k = 6.1$ MeV for protons and $k = 11.35$ MeV for deuterons. A graph of this relationship is shown in figure 4.3 for protons of energy up to 100 MeV. It is clear from this graph that the relationship between light output and kinetic energy is approximately linear for the proton energies that we are concerned with ($\sim$ 10-60 MeV).

The PMT pulse output signals, P_1 and P_2 are proportional to the intensities I_1 and I_2 respectively. The relationship between these signals and T the charged particle KE is given approximately by

$$T = \alpha\sqrt{P_1 P_2} + \beta \tag{4.4}$$

where α and β are the calibration constants for the particular E-block. This detector was calibrated by observing the geometric mean of the pulse height signals for protons of known energy incident on the detector. The calibration was first carried out by using the deuterium data obtained with a CD_2 target. In the d(γ,p)n

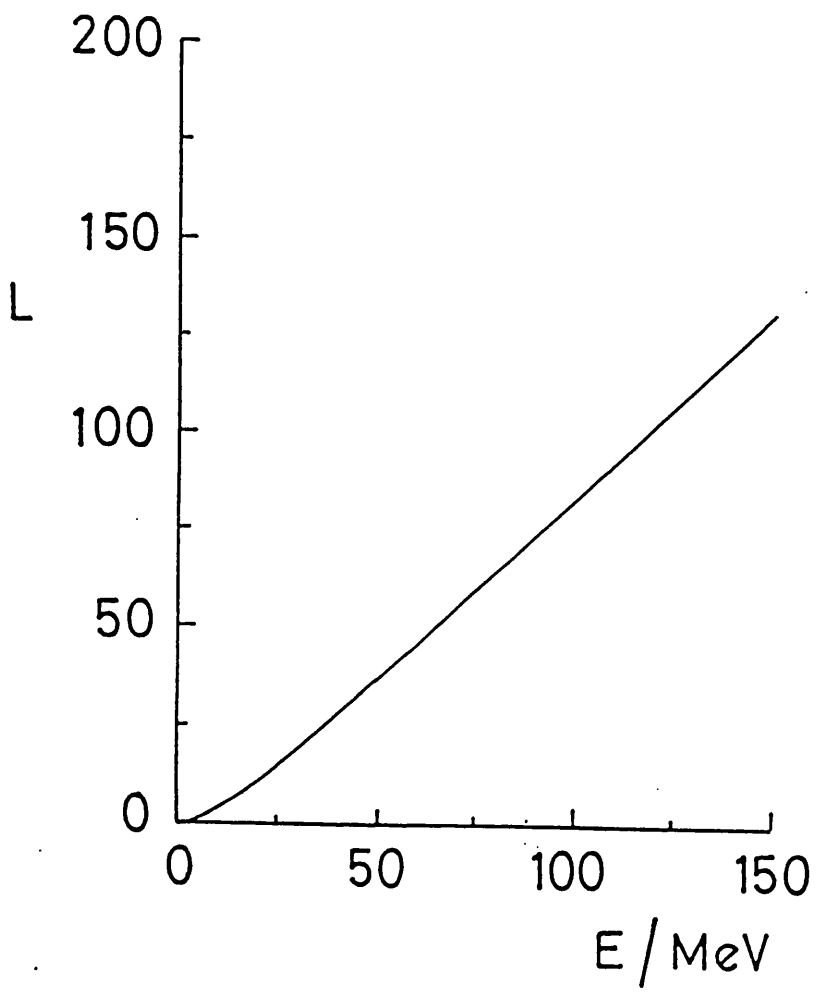

Figure 4.3: Light output versus proton energy for T_p in the range 0-150 MeV.

channel, the proton energy is determined by E_γ and θ_p alone and both of these are available from independent calibrations. This reaction had a good real to random ratio. Figure 4.4 shows the relationship observed between pulse height geometric mean and the expected energy for the d(γ,p)n reaction.

It was found, however, that the gain of the PMT's in the trigger detector drifted in time and that it was frequently better to use data from the ^{4}He (γ,p) reaction obtained at the same time as the (γ,pN) data for energy calibration. In this case the proton kinetic energy was calculated from the two-body kinematics of the ^{4}He (γ,p) ^{3}H reaction, knowing the photon energy and the proton angle, which are given by equations A.20 and A.21 in appendix A.1. This allowed the detector to be calibrated with an error in the proton energy of less than 0.5 MeV.

The only major disadvantage was that this self-calibration could only be used for photon energies up to ~110 MeV [74]. However for the higher photon energies, any drifts or changes in the calibration could be estimated from the position of the ^{4}He(γ,pn)d missing energy breakup peak since the TOF-detector timing calibrations were stable and the TOF energy calibration did not change.

The Light Flasher Unit

A light flasher unit, described in section 3.4, was incorporated into the ΔE,ΔE,E array in order to monitor the gain of the E-detector. This unit emitted pulses of light, of constant intensity, to produce a peak in the pulse height spectra of the PMT's. However, even with the aid of a feedback circuit, the intensity was only approximately constant. These flasher events were written to tape in such a way that they could be easily identified and separated from the nuclear events during the off-line analysis. There was a correlation between the flasher signals in

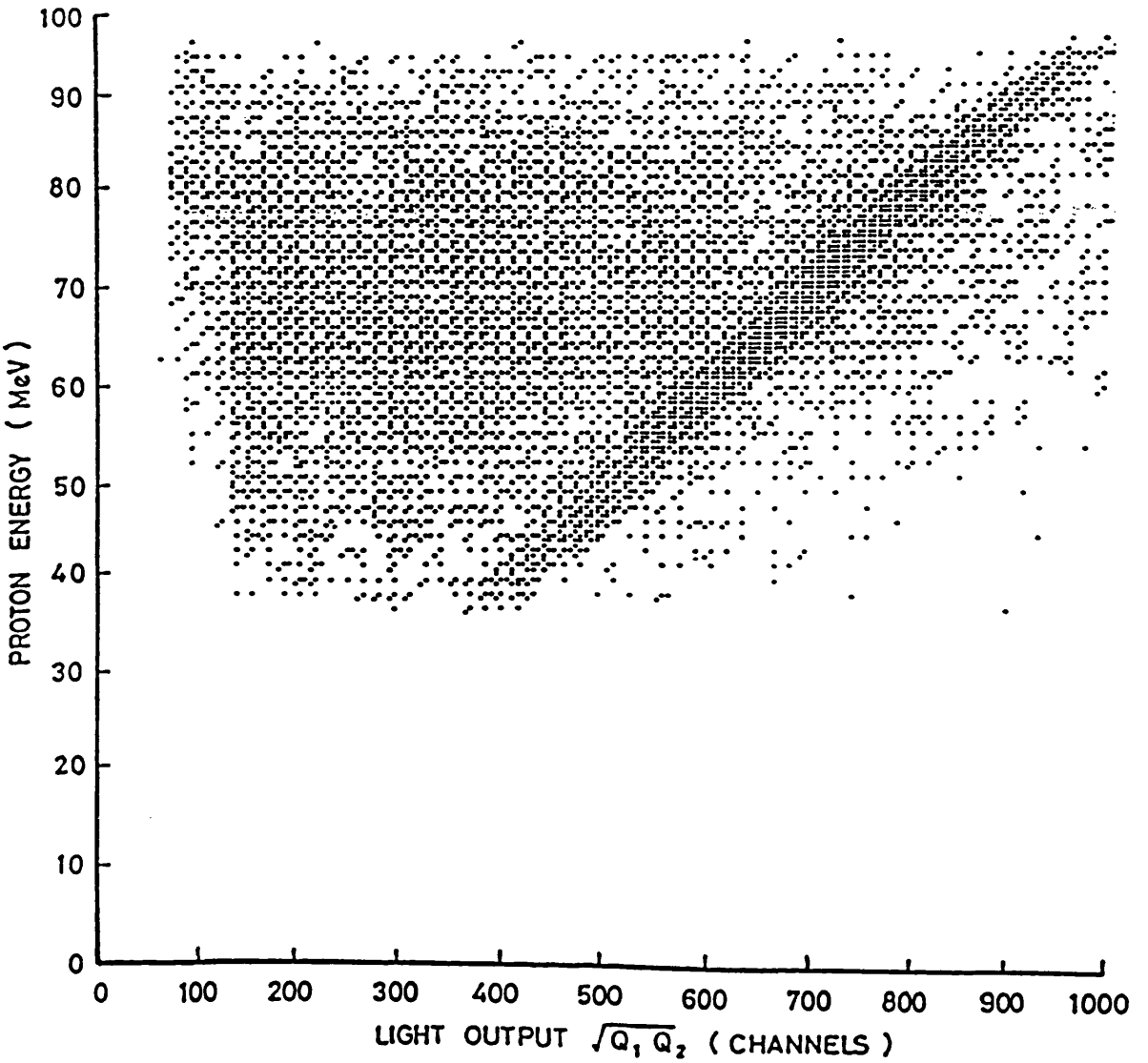

Figure 4.4: Scatter plot of proton energy calculated from photon energy and proton angle versus proton energy calculated from pulse height geometric mean in the ΔE,ΔE,E array.

the PMT's and the gains in the PMT's. Thus the flasher signals could be used to monitor the stability of the apparatus. If large drifts were observed, the detectors were re-calibrated for the data following the occurrence of the drift. For data at higher photon energies, where the (γ,p)t reaction could not be used for detector calibrations, the flasher signals were used to obtain new energy calibrations.

The flasher peak above is insufficient to track variations in both α and β, the gain and the offset calibration constants in equation 4.4. However it was found, using (γ,p)t calibrations at lower photon energies, that the offset, β, did not vary much. To a first approximation, therefore, it was constant, so that the gain could be calculated approximately from the position of the flasher peak alone. The slight offset shifts which were observed for some files for the lower photon energies were thought to be due to shifts in the ADC pedestal values. In the data, the pedestal values were negative (but close to zero) and thus they could not be measured directly in order to correct shifts in their values. For these reasons, the flasher data were only used in the calibrations of those files (such as background data) not containing ^{4}He data or CD_2 data It was less accurate than other methods used to calibrate the detector, a typical uncertainty being $\sim$1.5 MeV

4.1.4 Time-of-Flight Detector Array Calibration

The horizontal dimensions of the detectors in the time-of-flight TOF array were small, therefore the horizontal position was well determined by knowing which detector received the particle. The vertical position, on the other hand, was determined from the time difference between the signals from the top and bottom ends. The particle's flight path to the detector was calculated from its horizontal distance from the target, and from the vertical position of the incident particle at the detector

relative to the vertical position of the target.

The particles in the TOF-array were identified from the ADC and TDC information, but their energies were calculated from the TDC information alone. To interpret the TDC signals properly, it was necessary to obtain the start time (T_0) of the reaction for each TOF-detector TDC spectrum. This was done by carrying out an active target measurement.

The active target consisted of a plastic scintillator detector with a sheet of lead attached to its downstream side. The photons produced relativistic electrons which were scattered by the lead and subsequently detected by the TOF array. Since each electron travelled with a velocity of ~c, the flight times to each detector could be calculated from the electron flight paths. The recorded arrival times of the electrons at the TOF detectors could therefore be used to calculate their start time in the TDC spectrum and so obtain the timing offsets of the TOF detector TDC spectra required for the analysis of the data. This timing was compared with the arrival time of the TOF-detector signal in order to obtain a timing calibration for each detector.

In order to estimate the final reaction yields, it is necessary to take account of the TOF detector efficiencies for neutrons (in the (γ,pn) case). The code STANTON was used (in order to estimate these efficiencies) [75]. The predictions of this code are estimated to be accurate to $\pm 10\%$.

4.2 Data Reduction

The data produced in the ^{4}He measurement filled 15 magnetic tapes in total. This large amount of data takes a considerable length of time for the computer to process and only a very small fraction of the data corresponded to ^{4}He photonuclear events

which could be fully determined kinematically. In order to analyse the data, events which were clearly not useful were rejected by a number of methods, described below. In this process, it was impossible to ensure that no true nuclear events were rejected, therefore correction factors had to be applied to the data following the data reduction process to correct for these lost events.

The useful data are categorised into reaction channels, and events relating to different coincidence timing regions (see later), or to different FPD sections, are treated separately from one another. The target-out background data are treated in exactly the same way as the target-in foreground data at the data reduction stages. The steps taken to extract the suitable events for study are given in the following list:-

1. The ΔE,E detector array (shown in figure 3.4) was used to distinguish between protons, deuterons and electrons. To achieve this, the ADC signal geometric mean (GM) in the E-block was compared with the ADC signal GM in the ΔE-strip which fired. Each event could be displayed on an E-ΔE scatter plot as in figure 4.5. The proton, deuteron and electron events lie in distinct regions on this plot, and by selecting events which correspond to particular regions, proton or deuteron events could be identified and kept as separate data sets. In the data selection, data were treated separately for events in each E-block, ΔE-strip combination because the gains of the PMT's were only approximately matched. These cuts were made loosely in order to minimise the number of protons or deuterons lost due to a particle's energy being shared by 2 E-blocks (see figure 4.6). Nevertheless, the particle identification was imperfect because in some events the charged particles distributed their energies between two E-blocks and so failed to satisfy the cuts. This effect, however, could be kept to

a minimum by carefully selecting the regions used. In addition, events were necessarily lost from these regions because of inelastic interactions of protons in the scintillator. [76]. The effects of these losses are discussed along with the results in the next chapter.

2. An energy versus time-of-flight cut on the ΔE,ΔE,E array detector was carried out to remove some of the remaining unwanted electron events. The ADC signal GM in an E block was compared with the timing difference between the E block TDC which fired and the curved ΔE TDC signal. This gives the flight-time of the particle and hence is related to its velocity. An example of this cut is shown in figure 4.7 where events to the left of the dashed line are rejected. The fact that two separate cuts were used to identify charged particles enabled both cuts to be taken 'loosely' without allowing too many electron events through the cuts. This led to the rejection of relatively few good events, at the expense of retaining a little more background.

3. If a proton strikes the ΔE,ΔE,E array close to one of the PMT's in an E-block this gives a non-uniform light collection. Consequently the signal may misrepresent the particle's energy. Events close to one of the PMT's in a ΔE-strip were also rejected in order to remove events where particles are too close to the upper and lower corners of the E-block array where particles are not completely stopped by the scintillator. Events where the particle was within 12.5 cm of the end of an E-block or within 8.5 cm of the end of of a ΔE-strip were rejected. The positions of the cuts, which defined the solid angle of 0.9 sr subtended by the detector, are shown on the scatter plot in figure 3.5.

4. The next step in the data reduction was to require that at least one TOF-detector gave a signal. This was done by requiring that there were discernible

signals in at least one suitable combination of two ADC's and two TDC's. The TOF detectors were multiplexed, and to determine whether or not a given TOF detector fired, it was necessary to look at its unique combination of ADC's and TDC's to find out whether they all fired above suitable software thresholds in coincidence. The time window used at this stage was generous so as to include both prompt and random neutrons in the analysis. The positioning of the prompt and random regions was aided by observing the scatter plot given in figure 4.8 which shows the pulse height versus the square of speed for particles detected in a TOF-detector. This diagram shows a linear ridge due to protons and neutrons depositing their maximum energy, and a distribution of neutron events below this ridge. Events where more than one TOF-detector registered an event, for a given prompt or random region were discarded in the analysis.

5. The TOF-side ΔE-detector could be used to aid identification of the particle which emerged on this side of the target. If the particle was charged, the detector would fire, but neutrons had a negligible probability of triggering this detector. Even if a neutron fires it, it is highly unlikely that the recoil proton or neutron will be detected by one of the 24 scintillator blocks. For charged particle selection, a particle speed versus TOF pulse height cut was used, which allowed clear separation of protons and deuterons as shown in figure 4.9. The speed of a given particle was calculated from the TOF signal time and the distance from the target to the part of the TOF-detector which received the particle.

6. The data were then split into prompt and random regions (figure 4.10) on the basis of flight time to the TOF detectors and the time difference between the FPD and the ΔE,ΔE,E array. This procedure is described in section 4.3.1. This

is necessary because some of the events in the prompt region in a FPD TDC are still due to random coincidence, and the data must be corrected for such events.

7. Finally, for (γ,pn) data, a separation was carried out on the basis of the (γ,pn) missing energy, as defined in appendix A.2, in order to identify the breakup modes in the (γ,pn) channel. This missing energy resolution is sufficient to identify the (γ,pn)d and (γ,pn)pn modes as shown in figure 5.1

4.3 Normalisation of the Data

4.3.1 Corrections to the Data

In the course of the data analysis, one of the major steps was to extract unwanted events from the data. This unwanted data can be summarised in three broad categories, namely, background data, ambiguous data and events generated through random coincidences.

- The background data was corrected for by subtracting target-out data (suitably normalised) from the target-in dataset. This background data arose largely from the photon beam interacting with parts of the target assembly, including the thin kapton walls and the heat shielding around the target. In addition some background radiation is produced by the microtron and by the beam dump at the far end of the experimental hall.

- Experimental data which was ambiguous arose from multiplexing of the TOF-detectors and from multiple events in the FPD. This required correction factors to be applied to the data to compensate for the actual photonuclear events which had to be discarded.

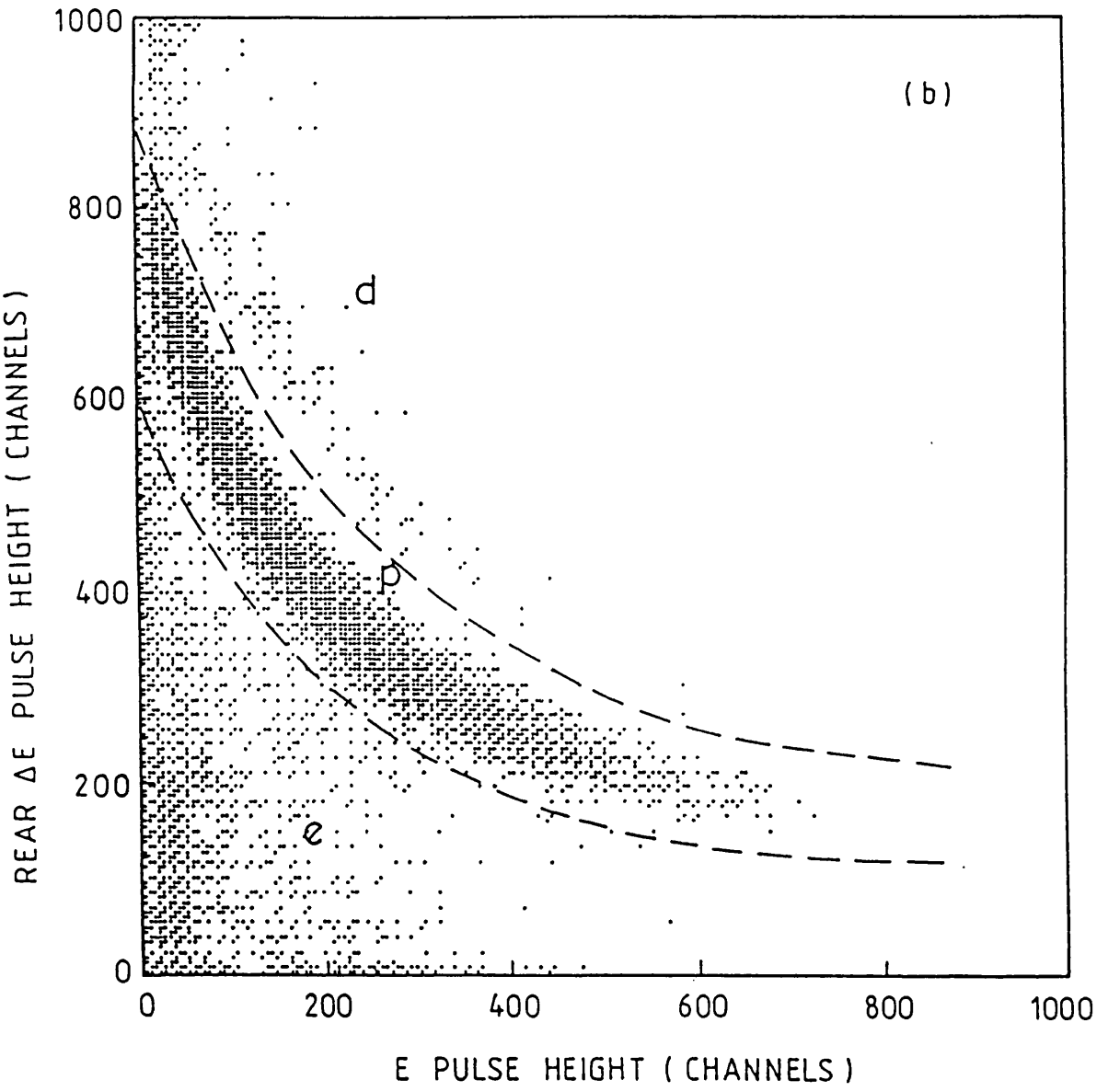

Figure 4.5: Particle identification E,ΔE plot showing protons(p) and deuterons(d). The events to the lower left of the protons are mainly due to electrons.

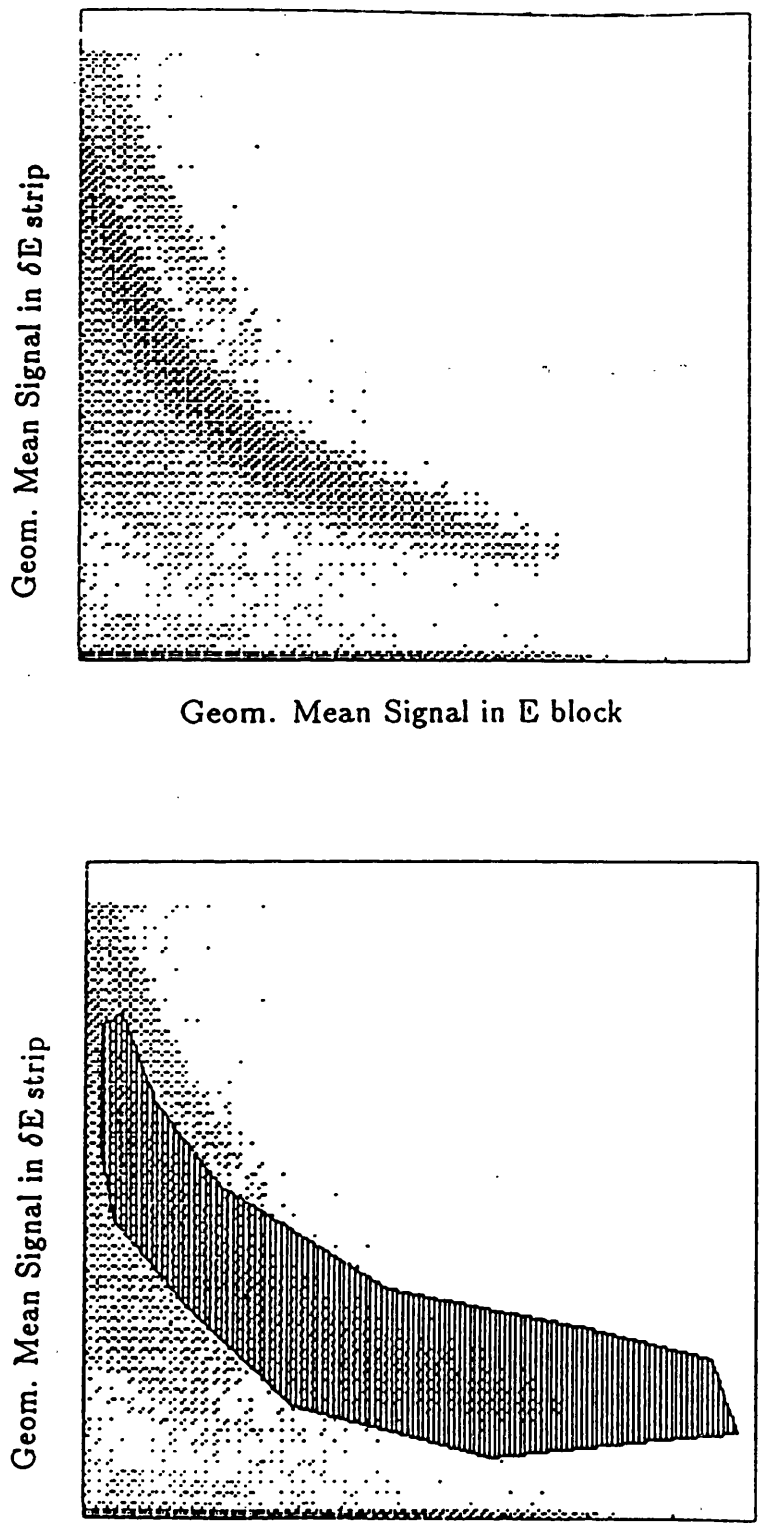

Figure 4.6: Upper plot shows an E-ΔE plot for a particular pixel. Lower plot shows within what limits a proton should appear.

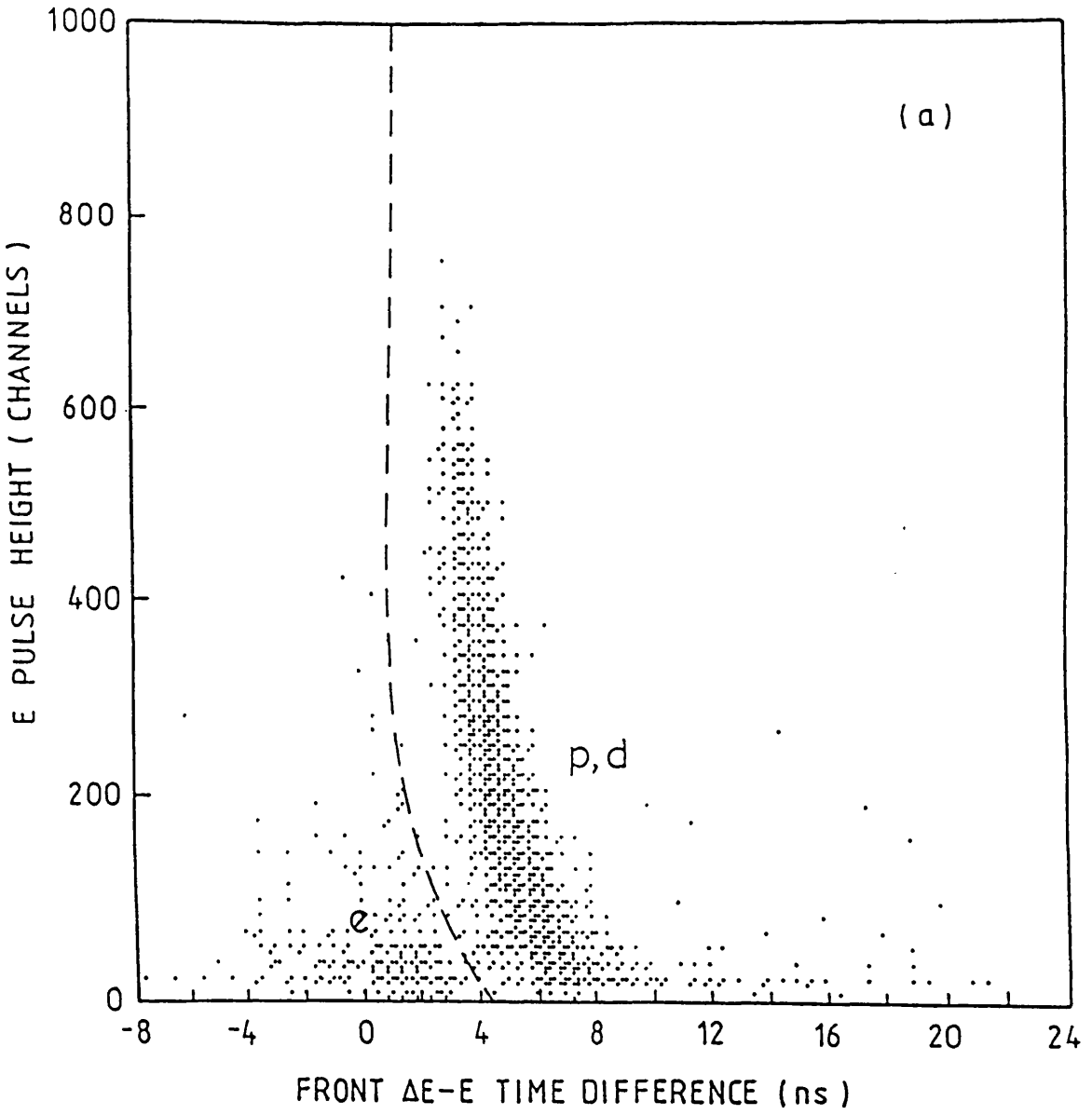

Figure 4.7: E-block pulse height signal versus particle time of flight between the curved ΔE detector and the E detector.

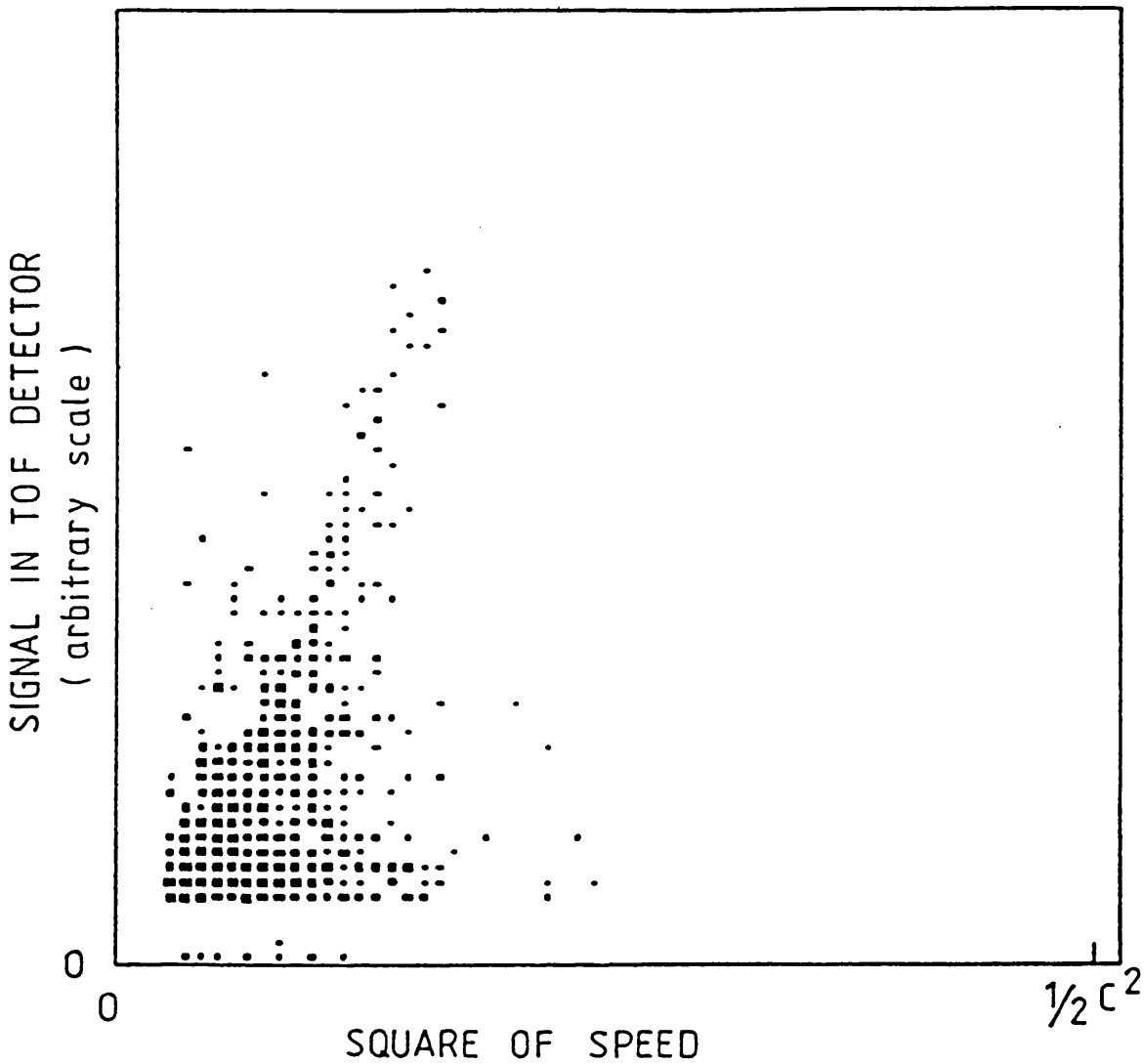

Figure 4.8: Pulse height in TOF-side ΔE versus (speed)^2.

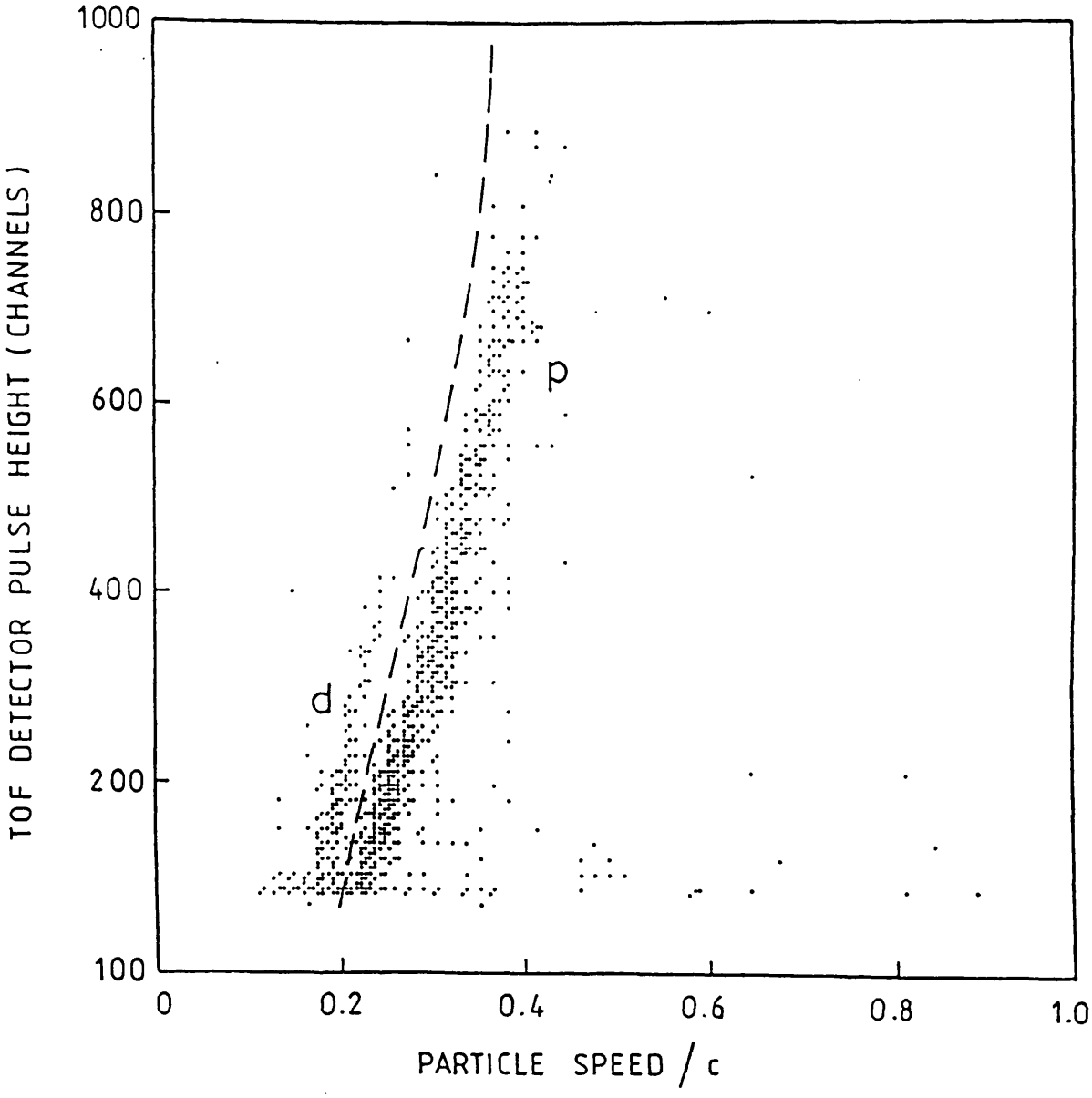

Figure 4.9: TOF detector ADC signal versus speed for TOF-side charged particles.

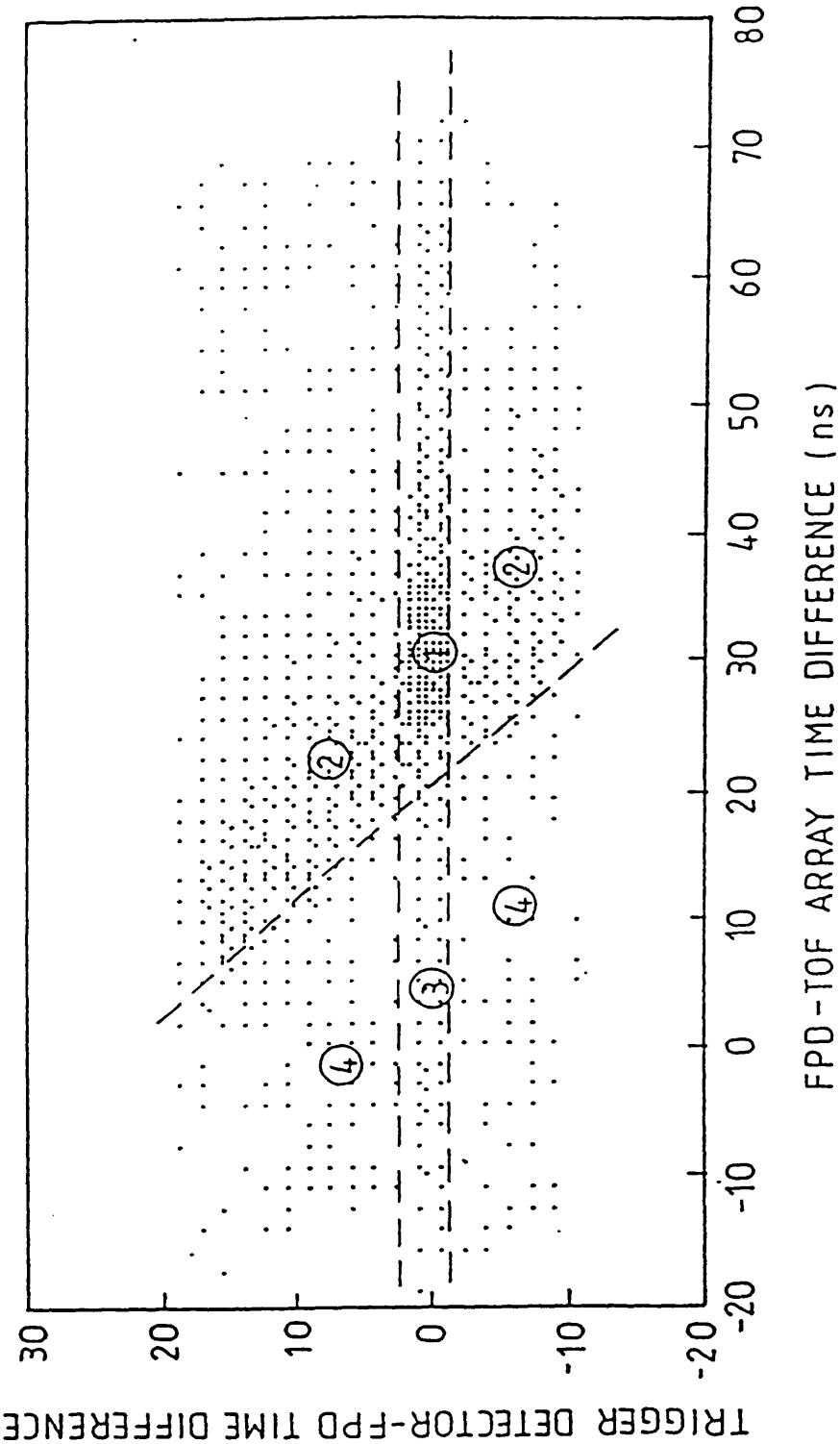

Figure 4.10: 2-D spectrum of e-n time difference versus p-e time difference for (γ,pn) events.

- The correction of the data for random coincidences was rather complicated and required some examination of the relative strengths of each type of random coincidence before a correction could be carried out (described below).

The remainder of this section will deal with how random coincidence effects and ambiguous events were treated.

Random Coincidences

In the analysis of the (γ,NN) data, a triple coincidence was required between the ΔE,ΔE,E array, the FPD and at least one detector in the TOF array. However it is possible that two of the detectors may receive correlated signals due to a single nuclear event while the third detector receives a signal due to a separate event occurring simultaneously. Such an occurrence is known as a random coincidence. An example of a random coincidence would be a proton and a neutron produced as a result of a photon, whose energy is outwith the tagged photon range, interacting in the target occurring simultaneously with a signal on the FPD, due to a tagged photon which does not interact in the target. Such events, in the text below, are called *(pn)e* events[1]. Since in these events the photons were untagged, they occur uniformly in time within the tagger TDC window. Figure 4.11 shows a TDC spectrum with a prompt coincidence peak sitting on top of a random background. The peak of events corresponding to the tagged photons was located and a suitably normalised sample of events on either side was subtracted from the data to correct for random coincidences. This subtraction was carried out because random coincidences exist under the prompt peak as well as in the events at either side of the peak.

[1]In this notation, the two terms in brackets correspond to the same reaction. The symbol not within brackets is not due to the same event but arrives at about the same time as the other two

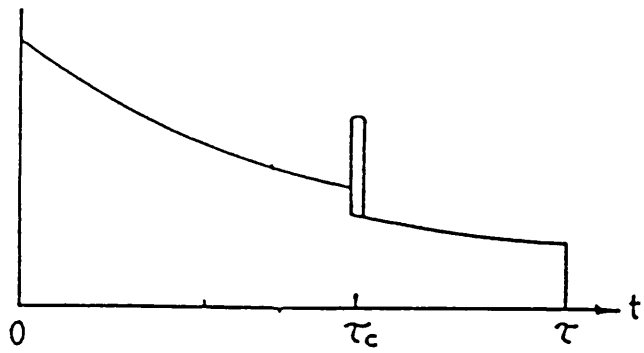

Figure 4.11: Time Distribution of a FPD TDC (schematic)

The effects of other random coincidences can be seen in figure 4.10 which shows four regions, labelled 1,2,3 and 4 which are designated according to their timing in relation to real and random events. Region 1 shows those events which are *(epn)*, That is, all particles prompt. Region 2 shows *e(pn)* events where an untagged photon may produce a p-n pair which are subsequently detected. Region 3 shows *(ep)n* events, where a proton and a FPD electron are prompt, but the neutron arrives either too early or too late to be from the same reaction. *(en)p* events lie directly above and below region 1 and as can be seen from the figure are not very significant. Finally region 4 contains completely random events where all three detector arrays receive particles from different reactions. In producing a (γ,pn) or a (γ,pp) spectrum, the data in regions 1 and 4 are added together (with appropriate normalisations) and the data in regions 2 and 3 are subtracted from this data in order to correct for random events. The reason for this will become apparent in the following argument.

Consider for simplicity the hypothetical situation where events are triggered by a beam particle, and two particles, labelled 1 and 2 are detected (see figure 4.12.

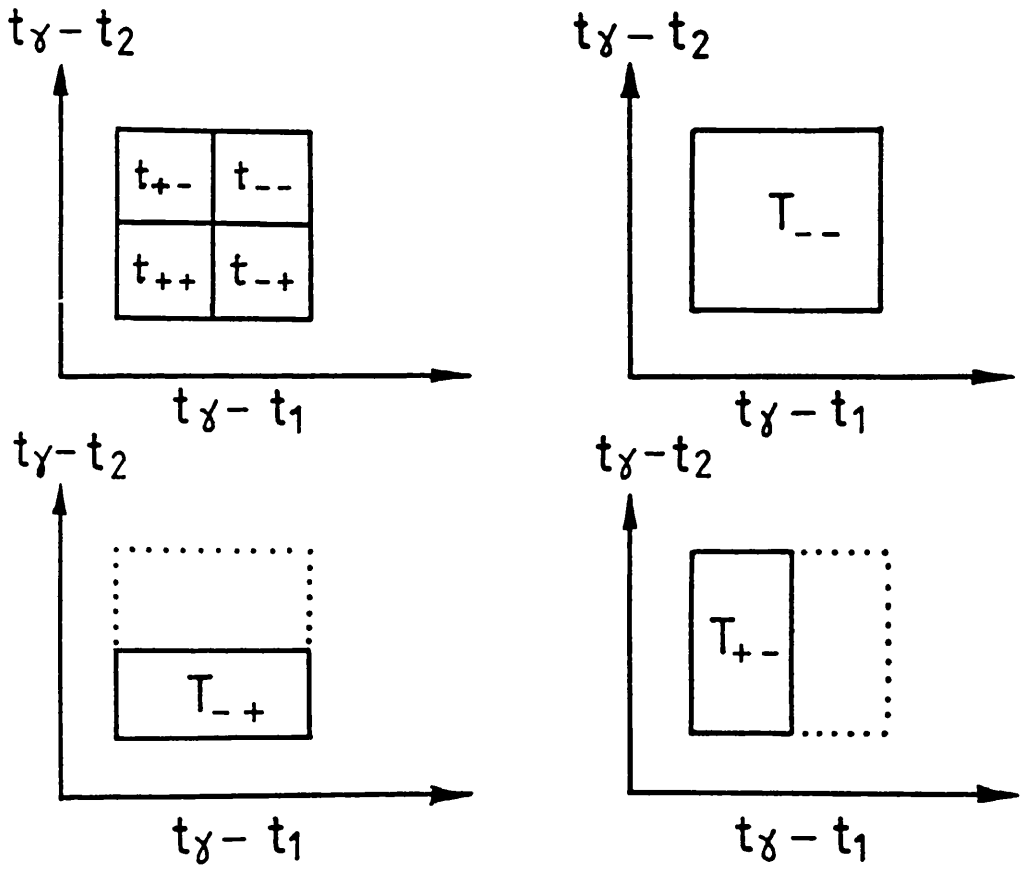

Figure 4.12: Schematic diagram: The horizontal axis represents the timing difference between particle 1 and beam particle, vertical axis is timing difference between particle 2 and beam particle. Symbols are explained in the text.

It is assumed here that there are no random coincidences involving an untagged beam particle and that the prompt and random regions are of equal size.
The symbols in the figure are defined as follows:-

t_{++} is the set of events where both particles arrive close enough in time to the beam particle that they could originate from the same reaction. these are called *(e12)* events.

t_{+-} is set of events where particle 1 is prompt (with respect to FPD) but particle 2 arrives at a sufficiently different time that it cannot belong to the same reaction. These are *(e1)2* events.

t_{-+} is the set of events where 1 is at the wrong time but 2 is prompt.

(e2)1 is the set of events where particle 1 arrives too early (or too late) but particle 2 arrives at the correct time to be consistent with a reaction.

t_{--} is the set of events where 1 and 2 both arrive at the wrong time, these are *(e)12* events.

T_{++} is the set of true nuclear events. The time distribution of T_{++} is the same as that of t_{++} and T_{++} is a subset of t_{++}. T_{+-} is set of events where particle 1 comes from the reaction produced by the tagged beam particle and particle 2 is random T_{-+} is set of events where 2 is from the reaction involving the tagged beam particle but 1 is random T_{--} is set of events where both particles are random

The T-sets are each mutually exclusive, similarly for the t-sets. Since the distributions of the events in a given rectangle in figure 4.12 may be treated as uniform, the following relations hold, where for any region S, $n(S)$ is the number of events in S.

$$n(t_{++}) = n(T_{++}) + \frac{1}{2}n(T_{+-}) + \frac{1}{2}n(T_{-+}) + \frac{1}{4}n(T_{--}) \tag{4.5}$$

$$n(t_{-+}) = \frac{1}{2}n(T_{-+}) + \frac{1}{4}n(T_{--}) \tag{4.6}$$

$$n(t_{+-}) = \frac{1}{2}n(T_{+-}) + \frac{1}{4}n(T_{--}) \tag{4.7}$$

$$n(t_{--}) = \frac{1}{4}n(T_{--}) \tag{4.8}$$

it may be shown from the above that

$$n(T_{++}) = n(t_{++}) + n(t_{--}) - n(t_{-+}) - n(t_{+-}) \tag{4.9}$$

Thus we may calculate the number of true nuclear events, $n(T_{++})$, from the numbers of events in the four regions t_{++}, t_{+-}, t_{-+} and t_{--} in figure 4.12 using equation 4.9. The above argument assumes that the number of random coincidences caused by untagged beam particles producing correlated 1-2 pairs is negligible. However, the least common type of random coincidence (see figure 4.10) was actually *(en)p* events. The axes were therefore effectively redefined so that the least common type of coincidence was neglected. The essential argument and method of correcting randoms was essentially the same, but definitions of t_1 and t_2 had to be modified as follows:-

If t_1 is defined as FPD timing plus TOF-detector timing - trigger timing (with appropriate cable corrections) and t_2 is defined to be trigger (ΔE, ΔE, E array) timing then the plots represented in figure 4.12 will correspond to t_{++} as region 1, t_{+-} as region 2, t_{-+} as region 3 and t_{--} as region 4. With these definitions it is valid to apply equation 4.9 to correct the data for randoms.

In figure 4.12 and in the above argument it is assumed that the prompt and random cuts are of equal width. However it was found to be advantageous to choose larger regions for t_{-+}, t_{+-} and t_{--} therefore the events in each of the four t-regions

had to be given weightings in inverse proportion to their physical areas on the scatter plot, to obtain the desired spectra.

Analysed Data

After the calibration parameters had been evaluated, the useful data were written in a partially analysed, calibration-independent form to simplify the final analysis stages. An event was only retained if it satisfied the criteria listed in section 4.2. This technique was helpful because it could be used to write all of the data in a concise form. These calibration independent files could easily be added together, with a given event containing information on the photon energy, proton and neutron momenta, and whether or not the event was prompt with respect to the two parameters illustrated in figure 4.10. Each event was assigned a weighting determined by the relative size of the region in figure 4.10 in which it belonged and was also assigned a label to indicate whether it corresponded to (γ,pn), (γ,pp) or any other identifiable reaction.

It was possible, during an event, that more than one FPD signal was received within a given region of the timing distribution in figure 4.10. The actual nuclear event would be equally likely to correspond to either of these two FPD signals, that is, it is equally likely that the event was created as a result of either of the two photons tagged. Therefore it was necessary that such an event be treated as two separate events, one where the photon corresponds to the first FPD TDC in question and one where it corresponds to the second. The method used to achieve this was to rewrite the event to the analysed data file as two separate events, which were identical but for the photon energies. This is essentially the same as treating each FPD TDC as though they were of a different experiment.

Weighting of Randoms Subtractions

In the present work it is often necessary to observe the behaviour of a particular physical quantity, such as the recoil momentum, or the proton angle. These parameters will be calculated from the events written on output files, where each event will be given a weighting according to whether it is real or random. The quantity of interest is in general a real number and may take a range of values. Thus what is studied is its statistical distribution. If events due to other processes interfere with the data, then their contributions should be subtracted from each spectrum, but often the subtracted events will require different weightings in the analysis from those of the events of interest, due to the different breadths of time windows used. Thus we must be clear how to perform this subtraction in the correct way paying particular attention to experimental errors. In the process of evaluating a spectrum, if n events correspond to the i^{th} channel in this spectrum, and the weighting of the j^{th} event in this channel is $w_j[i]$, then the number of counts in this channel, with its experimental error, will be

$$(\Sigma_{j=1}^{n} w_j[i]) \pm \sqrt{\Sigma_{j=1}^{n} (w_j[i])^2} \tag{4.10}$$

The $w_j[i]$ may be positive or negative, depending on the conditions of the event, that is, in what region of figure 4.12 it lies. The above method is used for any spectrum derived from the analysed data files, such as missing energy or recoil momentum for example. This is the technique used to correct for random and background events in the present analysis. The final spectra were obtained by adding weightings, with the errors added in quadrature.

Corrections for Detector Effects

Several overall corrections were made to the experimental yield to compensate for distortions which occurred at various stages in the analysis. The corrections are listed below:-

1. Events which were not recorded by the computer at the online stage:

   (a) Low energy charged particles which had energies below the threshold of the ΔE,E array. These events were corrected for by Monte Carlo simulations as described later.

   (b) Events lost due to inefficiencies in the TOF detectors, or due to their thresholds. These were corrected for by Monte Carlo simulations.

   (c) Events where one or both of the ejected particles missed the detectors altogether. These events were corrected for by Monte Carlo simulations.

   (d) Events where the particle passed between two ΔE-strips.

   f_l is the correction factor for events which are lost because the charged particle passes between two neighbouring ΔE-strips. If the gaps between the strips are of width $x = 0.6mm$ and the strips are of width $y = 20cm$, and if $c = 12.5cm$ equals the widths of the strips at either end of the detector which are ignored (as in section 4.2 (3)), then the total gap is $4x$, the total width of ΔE used is $5y - 2c$, and the fraction of events lost is

   $$\frac{4x}{5y - 2c} \tag{4.11}$$

   therefore

   $$f_l = 1 + \frac{4x}{5y - 2c} = 1.0033 \tag{4.12}$$

(e) Computer dead time. A correction for this effect was applied to the measured cross-section. f_d, the dead-time correction, is calculated from the ratio

$$f_d = \frac{X_t}{X_a} \tag{4.13}$$

where X_t is the total number of X-triggers and X_a is the number of X-triggers accepted by the computer. The correction factor for events lost in this way was found to be 1.0096.

2. Events that were rejected at the analysis stage because of ambiguities:

(a) Events where more than one electron was detected in a given FPD section. These correction factors for multiple hits within a FPD section are beam rate dependent and were applied separately to each FPD section and for each group of files. The correction for the nth FPD TDC is $exp(\alpha_n)$ [77] where

$$\alpha_n = (\tau_c^n + (S_n - 1)\tau^n)N_e'(n) \tag{4.14}$$

where S_n is the number of electron detectors feeding into the n^{th} FPD TDC (usually 8),

$$S_1 = 4, S_2 = S_3 = ... = S_{11} = 8, S_{12} = 7 \tag{4.15}$$

τ_c^n is the time difference between the beginning of the time gate (see figure 4.11) and the prompt peak, and τ^n is the time-width of the gate. $N_e'(n) = \frac{L_n}{S_n t_{\rm dat}}$ is the rate per unit time per channel of the n^{th} FPD TDC, where $t_{\rm dat}$ is the time taken to accumulate the data and L_n is the number of events recorded by the n^{th} FPD TDC.

The average corrections applied to each section ($e^{\alpha_1}...e^{\alpha_{12}}$) were respectively 1.019, 1.039, 1.042, 1.044, 1.046, 1.048, 1.049, 1.051, 1.056, 1.059, 1.066 and 1.063.

(b) Events where the TOF detector array could not be demultiplexed, because more than one detector appeared to receive a signal. These ambiguous events required a correction, f_m, given by

$$f_m = \frac{c_1 + c_2 + c_3 + ...}{c_1} \tag{4.16}$$

where c_n is the number of events where n detectors appear to register. The value is $f_m = 1.072 \pm 0.009$.

3. Events that were unintentionally lost at the data reduction stage because of the way that the data reduction was carried out:

(a) Events that were lost in the ΔE,E proton region cuts because the particle underwent a nuclear reaction and thus produced a reduced signal in the E-detector [76]. However this effect was small (with an estimated correction factor of ~3%) and was neglected.

The neutron detector and ΔE,ΔE,E array efficiencies were not used to correct the data by weighting the events as in reference [19], since for events where the efficiency is low, and the required correction is large (i.e. low energy neutrons), the calculated correction is inaccurate. Instead the effect was incorporated into the Monte Carlo program since events whose detection efficiency is low have only a small impact on the pseudo data generated by the Monte Carlo simulation. The simulation is then compared directly with the measured spectra.

4.3.2 The Target Thickness Measurement

In order to evaluate the absolute cross-sections, it was necessary to determine the quantity of ^{4}He within the photon beam. However, this was complicated by the fact that the liquid helium contained bubbles and the target cell windows "bowed out" because the target cell was set in vacuum. Due to the nonuniformity of the beam, and the nonuniformity of the target thickness, the effective thickness was difficult to estimate by direct measurement. In addition, it was uncertain exactly what percentage of the liquid volume was displaced by bubbles of gas. The method used for the target thickness measurement avoided these problems, because it calculated the target's *effective* thickness. This was done by measuring the number of electron-positron pairs which were produced in the target by pair production. During a separate run, two thin scintillator detectors were placed downstream from the target to detect e^-, e^+ pairs produced in the target by the tagged photon beam. The detector closer to the target was 1/8" thick and the other detector was 1/4" thick. A plot (figure 4.13) is shown of the signal in the first detector versus the signal in the second detector during this measurement. This plot allowed a cut on e^--e^+ pair events (this is the cluster of events further from the origin) to be carried out to remove unwanted background. By doing this, unwanted signals caused by pair production within the detectors were eliminated. The e^--e^+ yield from the target is proportional to the target's effective thickness and the square of the atomic number, it does not give an absolute determination of the target thickness directly but this can be achieved by comparison with a carbon target of known thickness.

Two ^{12}C foils of thicknesses 0.9 mm and 2.0 mm and known densities were alternately placed behind the target in separate runs in order to allow the inter-calibration to be made. The carbon strips produced additional pairs which were

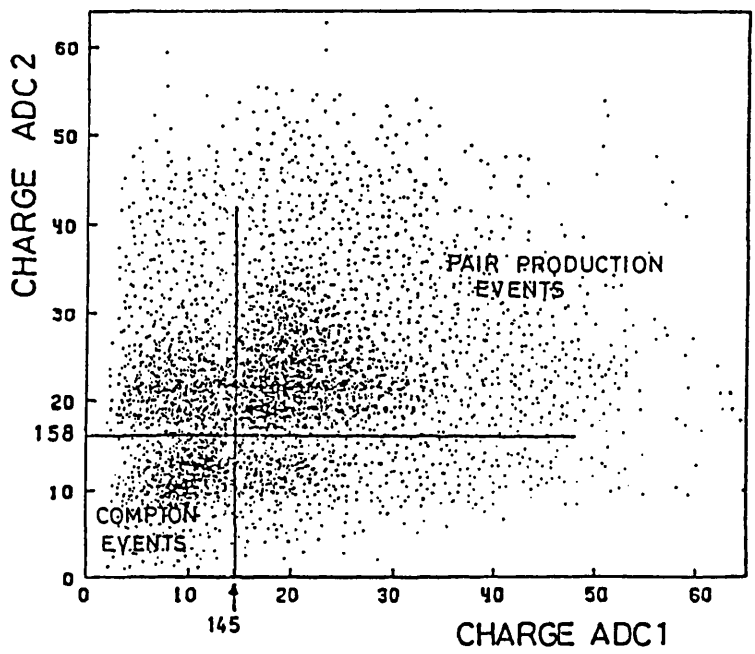

Figure 4.13: Pulse heights obtained in the target thickness measurement. The distribution at $\sim$ channels 20-25 is due to electron-positron pair production in the target and the carbon strip behind the target.

detected by the scintillator strips. The increase in the count rate caused by adding a carbon strip was compared with the yield from the target (corrected for empty target) in order to determine the target thickness. The ^{4}He target thickness was measured[78] to be 0.284±0.004 g/cm^2 for the larger target which was used for the lower γ-energy range. The target for the higher photon energy data was smaller, but no explicit thickness measurement was made for this target.

4.4 The Cross-Section Calculations

In this section the calculation of cross-sections for (γ,NN) reactions will be discussed. The two nucleons which are ejected will be labelled 1 and 2, where particle 1 is detected by the ΔE,ΔE,E array and particle 2 is detected by the TOF array.

In the following, n_t is the number of target nuclei per unit area. This quantity is derived from the target thickness measurement (described in section 4.3.2) and was (4.272±0.060) × 10^{22} nuclei/cm^2. The number of photons of energy E_γ that are incident on the target is ϕ and y is the corresponding yield of photonuclear reactions within the kinematic region of interest for an idealised experiment where every particle is detected. The nuclear cross-section in the selected kinematic region is thus given by

$$\sigma(E_\gamma) = \frac{y}{\phi n_t} \tag{4.17}$$

Evaluation of the Yield (y)

Equation 4.17 refers to the ideal experiment, where all of the reaction products are detected for *every* event. This formula cannot be applied directly since it is neither possible to detect the ejected particles at every energy nor at all possible angles.

Therefore the experimental yield is considerably less than the reaction yield y. The observed yield, y', is given by

$$y' = \frac{\eta(\mathbf{p}_1, \mathbf{p}_2)}{f} y \tag{4.18}$$

where f represents corrections applied to the data for event losses resulting from a number of factors which are described below and $\eta(\mathbf{p}_1, \mathbf{p}_2)$, described in section 4.5.2, is the probability that if particle 1 has momentum $\mathbf{p}_1$ and particle 2 has momentum $\mathbf{p}_2$, then both particles are registered by the detector arrays. The response function of the detector arrays, η, cannot simply be used to obtain y directly from y' because for most possible combinations of angles, η will be zero (*ie.* the particles are not detected). Thus to obtain y from y' one must evaluate an averaged value of η through a Monte Carlo simulation. As will be shown, we can calculate the (weighted) average value of η as a function of the quantity of interest (such as the recoil momentum), and use this as the correction factor. If the overall Monte Carlo correction is $C_{MC} = \frac{1}{\eta_{ave}}$ (described in section 4.5.2), then

$$\sigma(E_\gamma) = \frac{y'}{\phi n_t} C_{MC} f \tag{4.19}$$

The cross-section is usually binned as a function of some quantity, x, in which case C_{MC} is calculated for a specific value of x instead of being averaged over all values of x, and

$$\frac{\partial}{\partial x}\sigma(E_\gamma, x) = \frac{y'}{\phi n_t} C_{MC}(x) f \tag{4.20}$$

$\frac{\partial \sigma}{\partial x}(E_\gamma, x)$ is the differential cross-section with respect to x. The factor f is the correction factor for events lost due to computer dead time, multiple electron hits in a FPD TDC, TOF detector multiplexing, and for event losses due to protons or deuterons lost which pass through more than 1 proton detector E-block or ΔE join. This correction factor may be expressed as

$$f = e^{\alpha} f_d f_m f_l \tag{4.21}$$

Evaluation of the Photon Flux (ϕ)

The flux, ϕ, is given by

$$\phi = \varepsilon_t N_e \tag{4.22}$$

where N_e is the number of electrons detected on the FPD and ε_t is the tagging efficiency, or the fraction of FPD electrons which correspond to tagged photons incident on the target. The tagging efficiency, taken from several measurements, was found to vary slightly from run to run by up to ~0.5%. The average tagging efficiency was 0.373 ± 0.004.

In the case of events where an electron scatters in a FPD scintillator and fires a group of neighbouring channels in the FPD, the electron is treated in the analysis as though it interacts with the scintillator corresponding the the lowest tagged photon energy range. This somewhat arbitrarily removes the ambiguity regarding the photon energy but because the data is analysed section by section, it is possible that the electron may straddle two sections leading to double counting. However this latter effect was very slight and was therefore neglected.

4.5 Data Interpretation

4.5.1 Monte Carlo Simulations of Detector Responses

The acceptances in angle and energy of the detector arrays are modelled by Monte Carlo (MC) techniques. In order to account for biasing of the data as a result of particles not being detected for all angles or all energies, it is necessary to simulate the event losses on the computer in order to obtain corrections. For instance, above threshold, the TOF detectors have an efficiency of only ~10%, for neutron detection,

and this efficiency varies with neutron energy. This simulation is necessarily model dependent, as some theoretical model of the reaction mechanism must be used. For example, the quasideuteron model, using shell model single particle wavefunctions, or alternatively a phase space model may be used to describe the distributions of energies and angles of the outgoing particles.

In this Monte Carlo treatment, the following quantities are chosen at random from appropriate distributions:-

1. Photon energy: This is chosen at random for each event from a weighted distribution of photon energies. The distribution which was used was derived from the bremsstrahlung photon energy distribution multiplied by the absolute real deuteron cross-section for that photon energy.

2. Momentum of p-n pair: In the case of the QD model, the momenta of the two nucleons are chosen using shell model independent particle wavefunctions. From the momenta of the two nucleons, the momentum sum is calculated (QD momentum). The momenta of the beam photon and the QD are then transformed into the γ + QD centre of mass frame. The cross-section distribution of the γ + QD reaction is taken to be the same as that of the $\gamma + d$ reaction within the respective COM frames of the two reactions. For (γ,pp) reactions in this model, the QD angular distribution may be used or an isotropic distribution. The predicted proton and neutron momenta from this reaction are then transformed back to the lab frame. In the case of the phase space model, the proton and neutron kinetic energies in the final state are chosen in such a way that all kinematically allowed combinations are equally probable.

For the QD model the Monte Carlo program used a parametrisation of the

deuterium photodisintegration cross-section [70] and either harmonic oscillator wavefunctions or variational wavefunctions obtained using the Urbana potential [67].

The predicted momentum distribution of the QD has to be truncated at very high QD momenta. This is because for high QD momentum (which corresponds to high recoil momentum) a significant proportion of the available photon energy provides the recoil and QD energies. Above a certain QD momentum value, therefore, there is insufficient photon energy left to break up the QD. If this happens, then the MC program rejects that particular event as being not energetically possible. For an event to be recorded in the program, the reaction must not only be energetically possible but the ejected particles must have sufficient energies and be travelling in the right directions to be detected by the apparatus. The events detected are also weighted according to their detection efficiency.

4.5.2 Monte Carlo Method

In the following treatment $\eta(\mathbf{p}_1, \mathbf{p}_2)$ is the probability that if particles 1 and 2 have momenta $\mathbf{p}_1$ and $\mathbf{p}_2$, then particle 1 is registered by the E,ΔE detector and particle 2 is registered by the TOF detector array. The value of η must be calculated for every event in the Monte Carlo simulation.

η is given by

$$\eta(\mathbf{p}_1, \mathbf{p}_2) = \chi_L(\theta_1, \phi_1)\varepsilon_L(T_1)\chi_R(\theta_2, \phi_2)\varepsilon_R(T_2) \tag{4.23}$$

where θ_i and ϕ_i are the polar angles of particle i and T_i is the kinetic energy of particle i.

$$\chi(\theta, \phi) = \begin{cases} 1, & \text{if detector covers the direction of the particle} \\ 0, & \text{otherwise} \end{cases}$$

where L refers in this case to the ΔE,ΔE,E array and R refers to the TOF array. $\varepsilon_L(T_1)$ is the probability of particle 1 being stopped by the scintillator and producing a pulse of light above the E,ΔE detector threshold. $\varepsilon_R(T_2)$ is the probability of particle 2 being stopped by the TOF array scintillator to produce a pulse of light above threshold.

Using MC models,

$$C_{MC} = \frac{1}{\eta(p_1, p_2)} \tag{4.24}$$

may be estimated as a function of recoil momentum or another suitable parameter. This may then be used as a correction factor to the experimental data as in section 4.4, allowing cross-sections to be determined.

Model Predictions

The Monte Carlo program works as follows: If x is the probability that the particles are detected for a given event, then x is added to the channel of the spectrum under study. For example, if an event had recoil momentum 256 MeV/c predicted in a particular event and the probability of detection was 0.13 then in the simulation the effective number of counts in the 250-260 MeV/c bin would be increased by 0.13 .

Since the efficiencies of the TOF-detectors are normally higher for protons than for neutrons, it is expected that the correction factors for (γ,pp) analysis will be less than for (γ,pn) analysis. It is also expected that the overall correction factors will generally be lower for QD reactions than for PS reactions. This is because the strong angular correlation between the outgoing particles in the QD case produces a higher detection efficiency since the detector systems were placed roughly opposite one another.

Chapter 5

Results

This chapter presents the results of the experiment. Measured missing energy spectra, angular correlation spectra and recoil momentum spectra are presented and comparisons are made with predictions of various reaction models. Cross-sections are deduced and compared with previous measurements. Finally comparisons are drawn with (γ,NN) reactions in other light nuclei.

The ΔE,ΔE,E and TOF detectors can only detect particles over limited angular ranges and have restricted energy acceptances. This leads to the data being biased and Monte Carlo simulations are used to interpret the spectra. To evaluate the cross-sections, correction factors were obtained from the Monte Carlo calculations.

5.1 Missing Energy

The double-arm missing energy (appendix A.2) yields important information on the reaction in both the (γ,pn) and (γ,pp) channels. The (γ,pn) missing energy, which is fully determined from the experimentally measured parameters, indicates among other things whether the residual nucleus is a bound deuteron, or a separate proton-neutron pair. Furthermore the shape of the (γ,pn)pn channel's contribution to the

missing energy spectrum is related to the photon interaction mechanism and can in the case of a quasideuteron interaction be predicted from the quasideuteron (QD) momentum distribution, as explained in appendix A.2.1.

5.1.1 Missing Energy for the (γ,pn) reaction

The missing energy for the (γ,pn) reaction is given by

$$E_m = E_\gamma - T_p - T_n - T_R \tag{5.1}$$

where E_γ, T_p and T_n are respectively the energies of the tagged photon and the detected proton and neutron. T_R is the recoil kinetic energy and is calculated as described in appendix A.2.

An experimental (γ,pn) missing energy spectrum is shown in figure 5.1 for photon energies in the range 80-131 MeV. The experimental resolution is sufficient to separate the (γ,pn)d and (γ,pn)pn events. The (γ,pn)d reaction should give a single value for missing energy at E_m = 26.1 MeV, smeared only by the resolution of the detector arrays. However the extra degree of freedom in the 4-body disintegration channel allows a range of missing energies from 28.3 MeV upwards, with the upper limit depending on the energy available to the reaction and on the detector thresholds. After the MC corrections have been applied to this spectrum, the areas under the 3-body and 4-body breakup peaks correspond to the total cross-sections of the two channels.

It would appear from this figure that the three-body yield is much stronger than the four-body yield despite the residual particles in the three-body case being held together by a binding energy of only 2.2 MeV. However, in practice the detec-

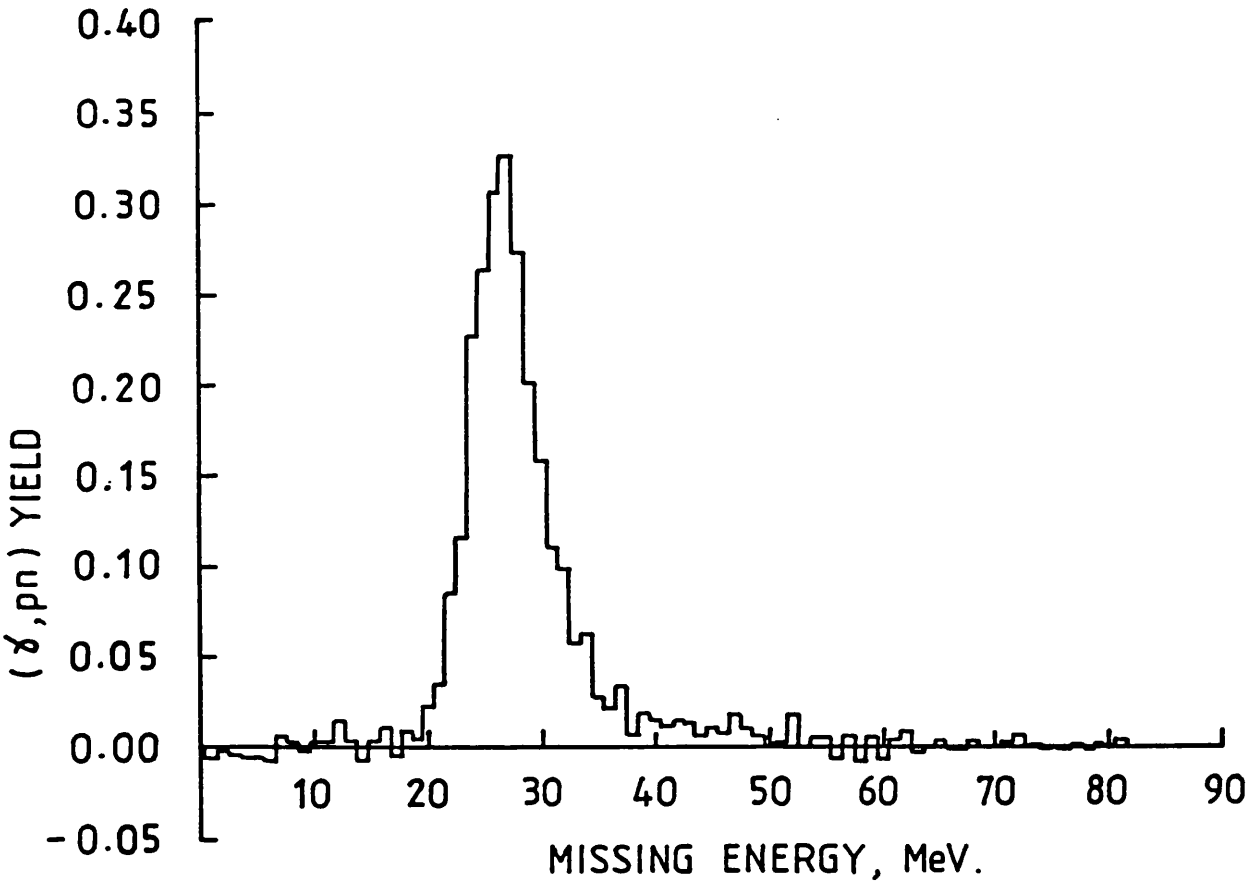

Figure 5.1: Missing energy spectrum for (γ,pn) events:- The peak at 26.1 MeV corresponds to the (γ,pn)d channel. The weak broader distribution at higher missing energies is due to the (γ,pn)pn reaction. The vertical scale is arbitrary.

tor thresholds prevent any measurement of the four body strength at the highest missing energies. The observed strength at lower missing energies is also truncated by detector effects for the lowest photon energies which were studied. This is particularly evident in figure 5.2 where the lowest photon energy range (bottom figure) shows little strength for missing energies above 30 MeV. Even at the highest photon energies where the effect of thresholds is expected to be much less important the 4-body contribution is small compared to the 3-body contribution. However a quantitative assessment of the relative strengths requires a detailed consideration of the shape of the 4-body distribution (appendix A.2.1), and of the detector acceptances.

The spectrum of the ^{4}He (γ,pn) missing energy in figure 5.1 reveals a (γ,pn)d peak at 26.1 MeV of width 7 MeV. This width indicates the overall energy resolution of the detection system. The broader distribution at higher missing energies is attributed to the (γ,pn)pn reaction and appears much weaker than the (γ,pn)d peak. Figure 5.3 shows this missing energy together with the d(γ,pn) missing energy spectrum obtained from calibration data taken using a CD_2 target, shifted, scaled and superimposed on the ^{4}He three-body breakup peak. This reaction, like the ^{4}He (γ,pn)d reaction, has a unique Q-value, and therefore the deuterium peak also reflects the experimental missing energy resolution. Since the charged particle energy losses in the two targets are very similar, both peaks would be expected to have the same width. As can be seen, the two peaks do have very similar shapes, except for the high missing energy tail due to the ^{4}He four-body breakup. Both the ^{4}He and ^{2}H missing energy spectra are expected to show small tails at high missing energies due to nuclear interactions of protons detected in the scintillator (as described in ref. [76]) which degrade the detected proton energy shifting events to higher missing energies. However a significant cancellation of this effect is expected if the deuterium peak shape is fitted to the ^{4}He data in order to extract the 4-body experimental

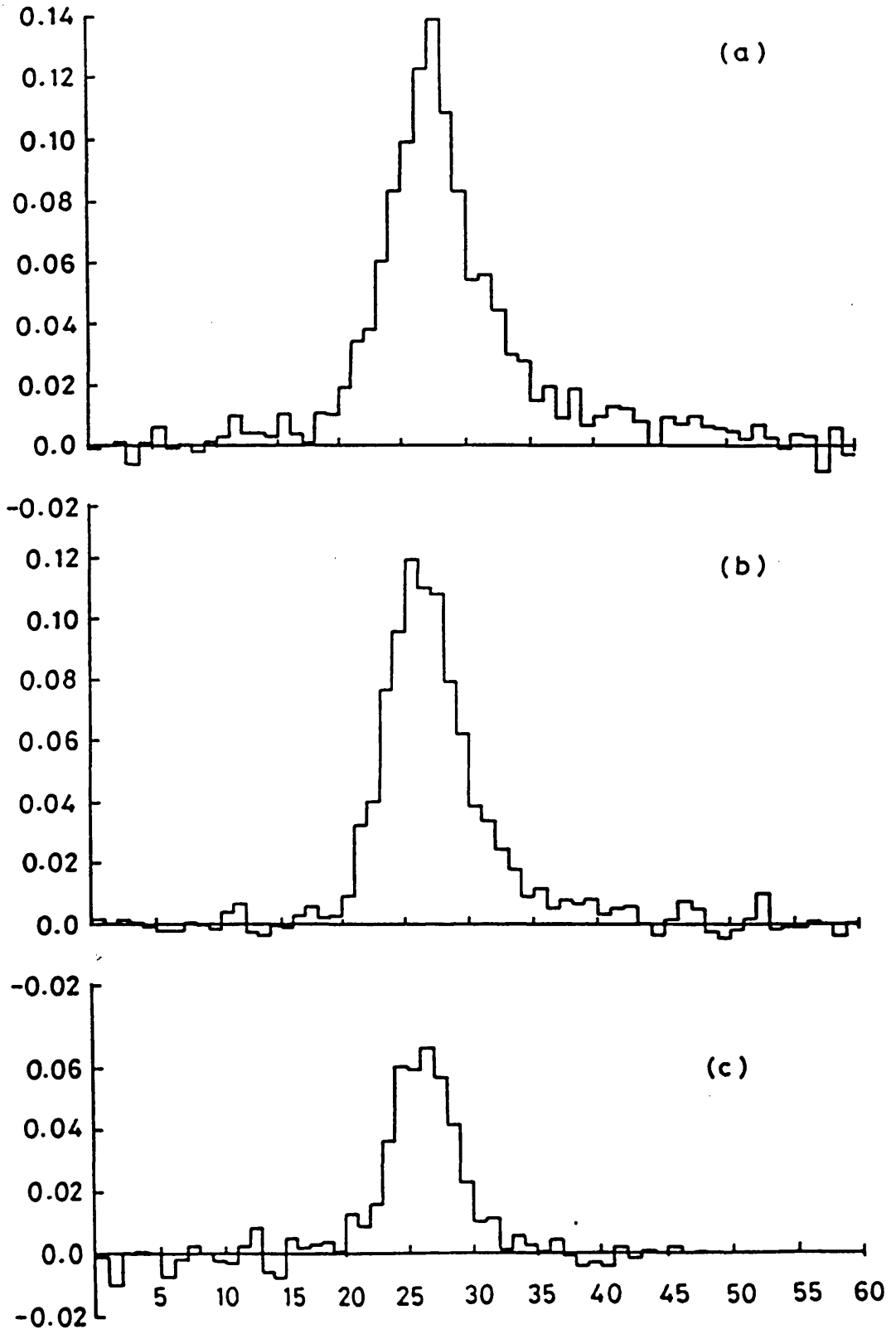

Figure 5.2: Experimental missing energy yields for three photon energy ranges, namely 115.0-131.5 MeV, 97.0-115.0 MeV and 79.5-97.0 MeV.

yield, since the nuclear interaction contributions should be broadly similar in both peaks.

The difference between the two missing energy yields in figure 5.3 is shown in figure 5.4 and reveals the extent of the ^{4}He (γ,pn)pn four-body breakup strength (thick solid line). The reaction threshold is also shown on the graph and agrees well with experimental data. Figure 5.4 also shows the MC prediction for the quasideuteron (QD) model with simple harmonic oscillator (SHO) momentum distributions (thin solid line), and a phase space distribution (dashed line). The two proton absorption prediction (where the photon is assumed to be absorbed by a proton-proton pair) is calculated with simple harmonic oscillator wavefunctions and is shown as a dotted line. The MC calculations take the detector acceptances into account. The QD model results calculated with the variational wavefunctions of Schiavilla *et.al.* [67] (using the Urbana potential) were found to be not significantly different from the harmonic oscillator results. There is very little difference between absorption on a p-p pair and the phase space distribution. The results of absorption on a p-n pair, however, give a distribution which peaks at lower missing energies. None of the models provides a perfect fit to the data, which has an intermediate shape, so that no definite distinction between the models can be made.

5.1.2 Missing Energy for the ^{4}He (γ,pp) reaction

The (γ,pp) missing energy is shown in figure 5.5. This contains a single broad distribution of 4-body breakup events in which a correlated p-p pair is detected. The (γ,pp)nn detection efficiency is an order of magnitude higher than that of the (γ,pn)pn channel, but despite this, its detected strength is still much less than that of the (γ,pn) reaction. The (γ,pp) reaction could result from direct absorption of

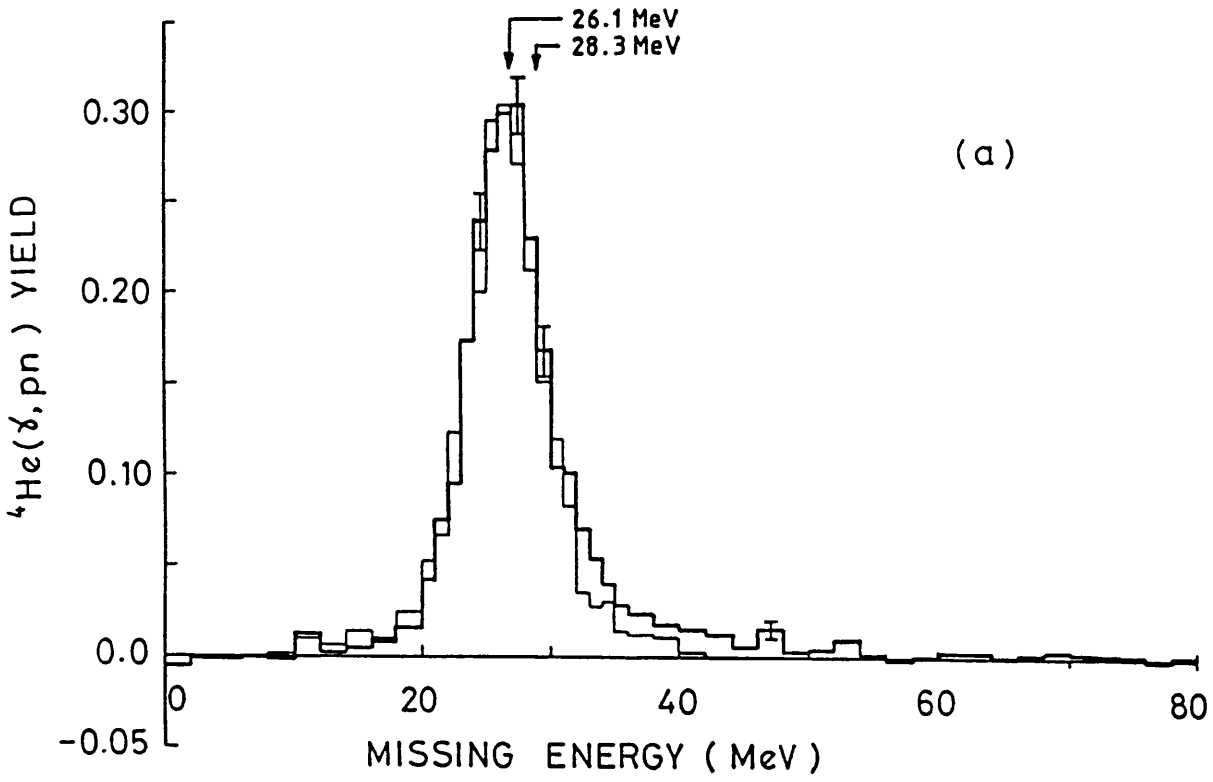

Figure 5.3: The ^{4}He (γ,pn) missing energy contrasted with the d(γ,pn) missing energy. The thick line is the ^{4}He missing energy spectrum. The thin line is derived from the deuterium missing energy peak.

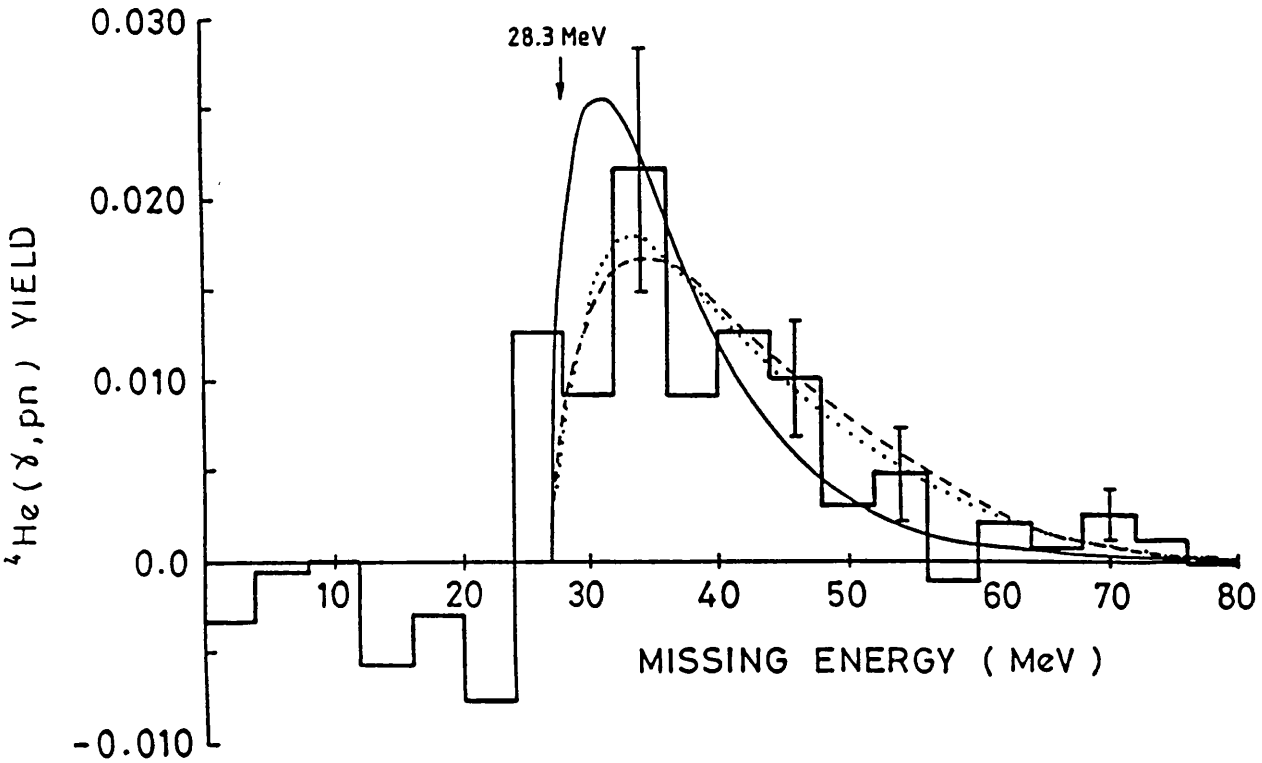

Figure 5.4: ^{4}He(γ,pn)pn missing energy distribution deduced from the difference between the ^{4}He yield and the deuterium yield. The thick line is the experimental data. The thin solid line is the prediction from the QD model with SHO wavefunctions. The dotted line is for absorption of the photon by p-p pairs. The dashed line is the PS model prediction.

the photon by the p-p pair, from a final state interaction (FSI) following absorption by a p-n pair, or by 3-body absorption. As can be seen in the figure, the results are fairly consistent with both a QD model and a phase space (PS) model prediction, but do not agree with a two-proton absorption mechanism.

5.2 Angular Correlations and Distributions

The QD model predicts that if two nucleons are ejected due to a photonuclear reaction, their directions will be correlated with the nucleons leaving in approximately opposite directions in the centre of mass frame of the $(\gamma + \alpha)$ system. A spectrum of this angle is shown in figure 5.6. This spectrum was calculated as described in appendix C.

It is because of the positioning of the detectors that the detection system is primarily sensitive to events where the proton and the neutron left the nucleus "back to back". The MC predictions for the opening angle in the QD and PS models are shown in figures 5.7 and 5.8 after detector acceptances have been taken into account. The MC calculations suggest that the opening angle distribution is insensitive to the reaction mechanism, since the predicted results for the QD model and the PS model appear very similar. The main reason for the similarity is probably that the apparatus was configured with detectors positioned at opposite sides of the target so as to be especially sensitive to N-N pairs coming off roughly back to back.

The proton and neutron angular distributions are shown in figures 5.9 and 5.10. Significant forward peaking is observed in the proton angular distribution for (γ,pn) events.

It is of interest to observe the experimental yield in the reference frame in

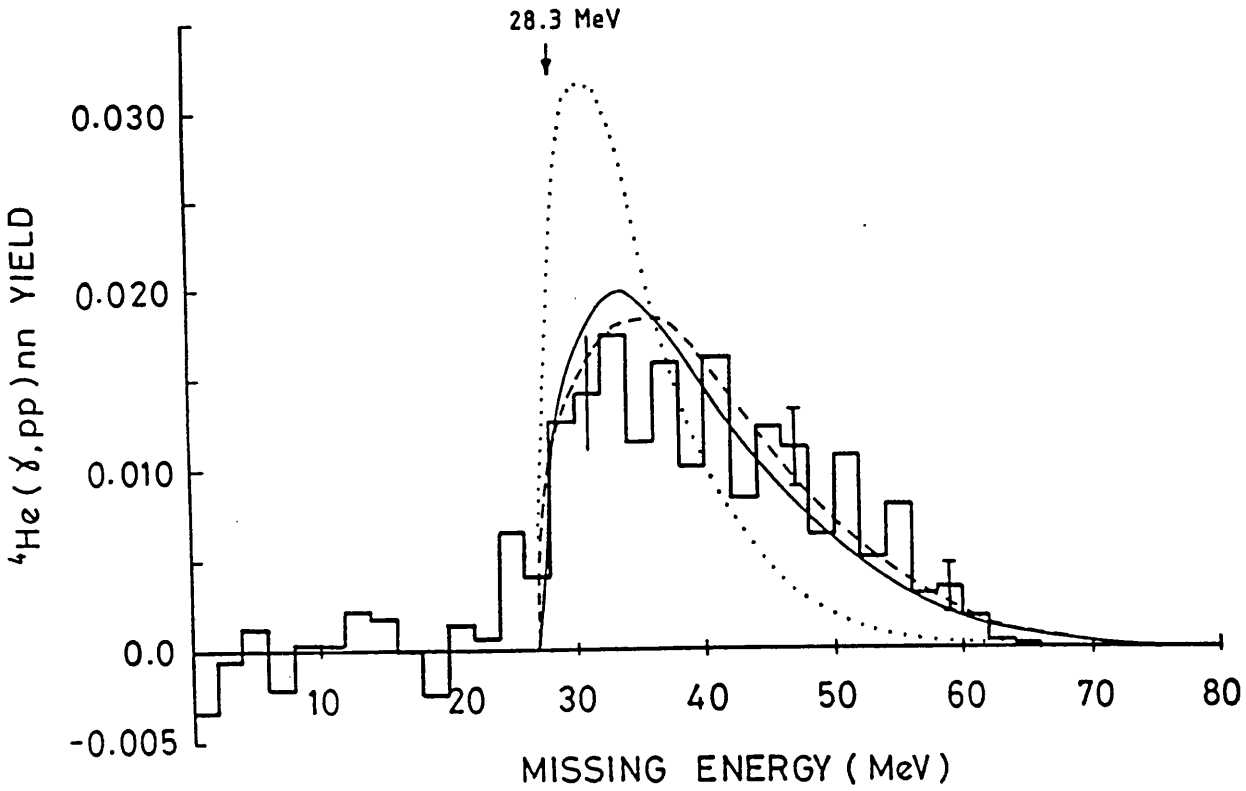

Figure 5.5: ^{4}He (γ,pp) missing energy. The thick line is experimental data. The thin solid line is the prediction from the QD model with SHO wavefunctions. The dotted line is for the 2-proton absorption model prediction. The dashed line is for the PS model prediction

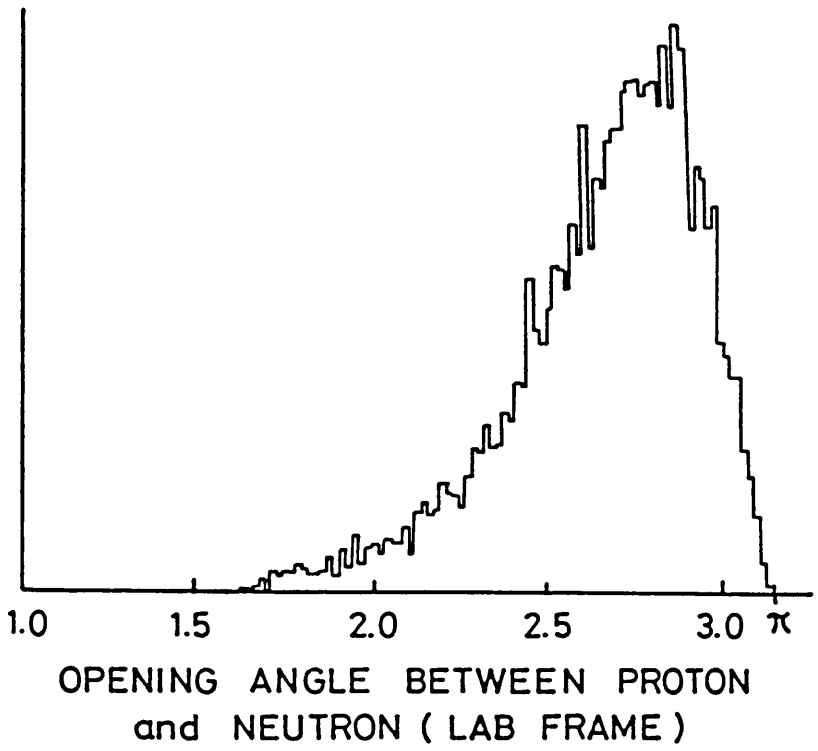

Figure 5.6: Experimental distribution of θ, the opening angle between correlated nucleons in radians, measured in the lab frame.

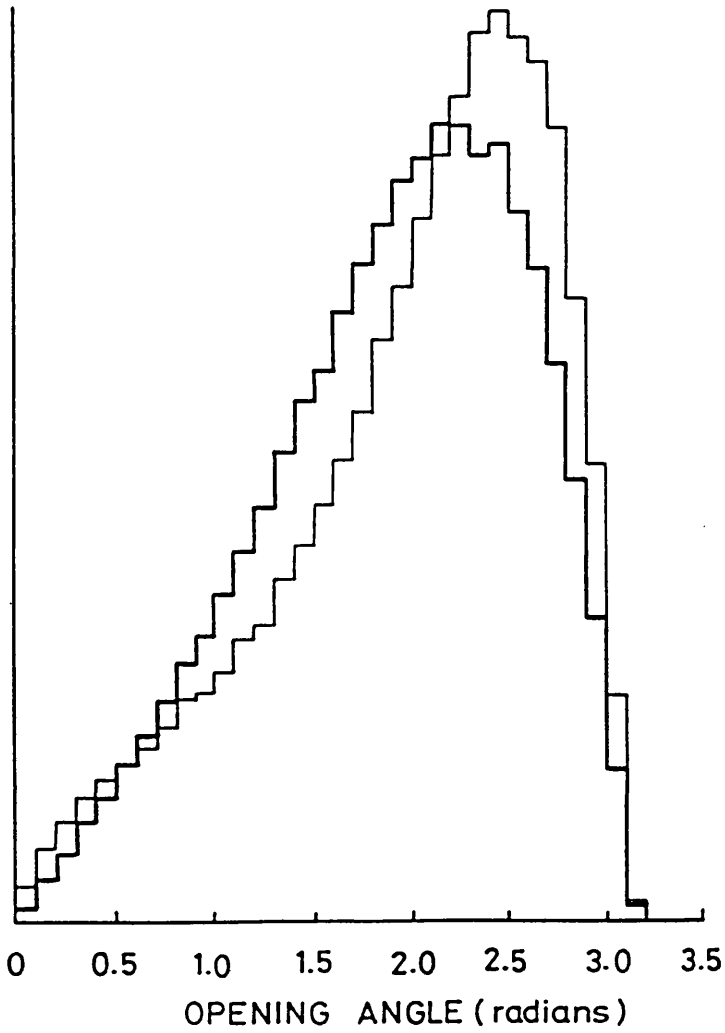

Figure 5.7: Monte Carlo predictions for the distribution in opening angle (radians), without the condition of particles being detected. The thick lines represent PS predictions and the thin lines are QD predictions.

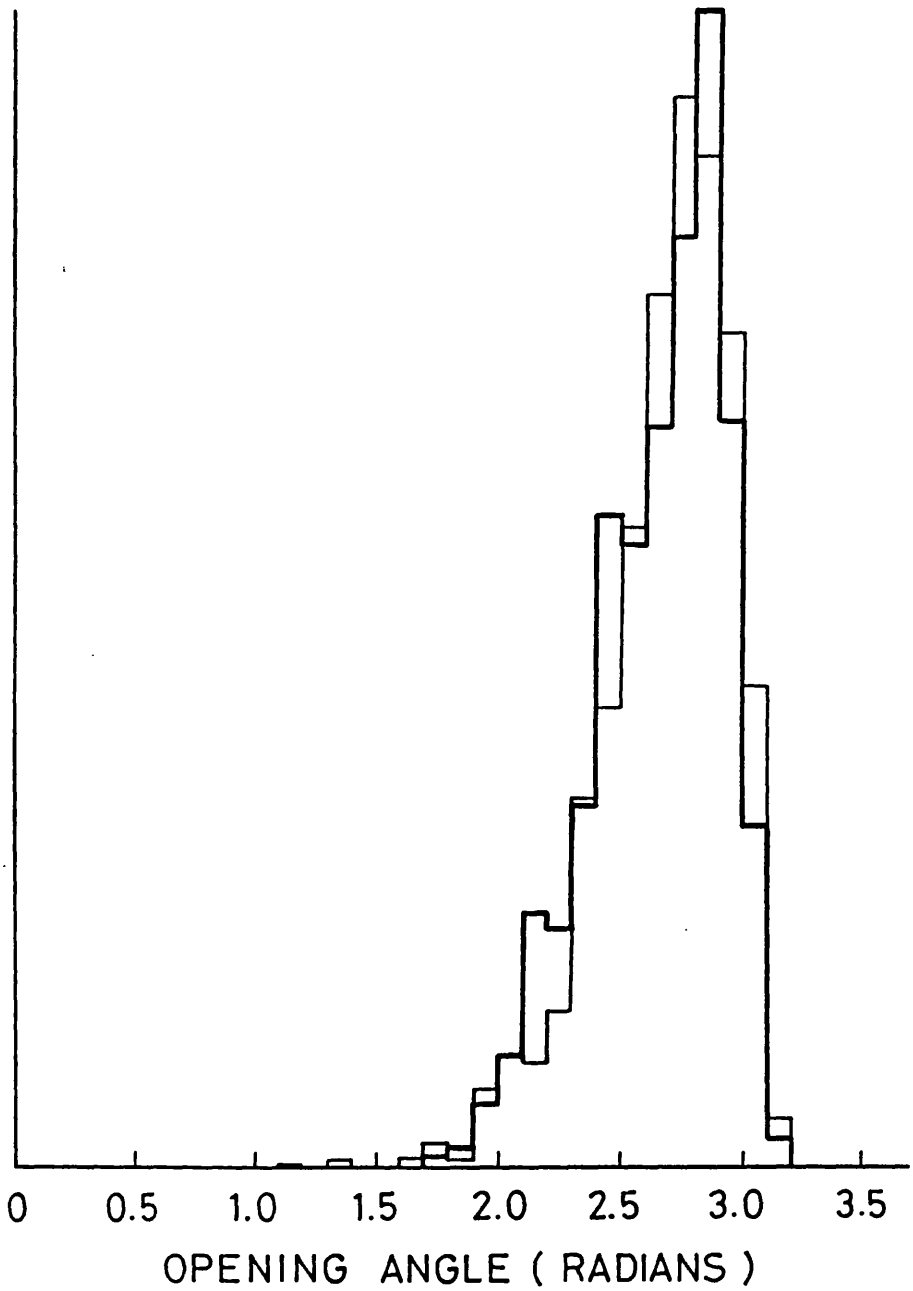

Figure 5.8: Monte Carlo predictions for the distribution in opening angle (radians), with the condition that the particles are detected. The thick lines represent PS predictions and the thin lines are QD predictions.

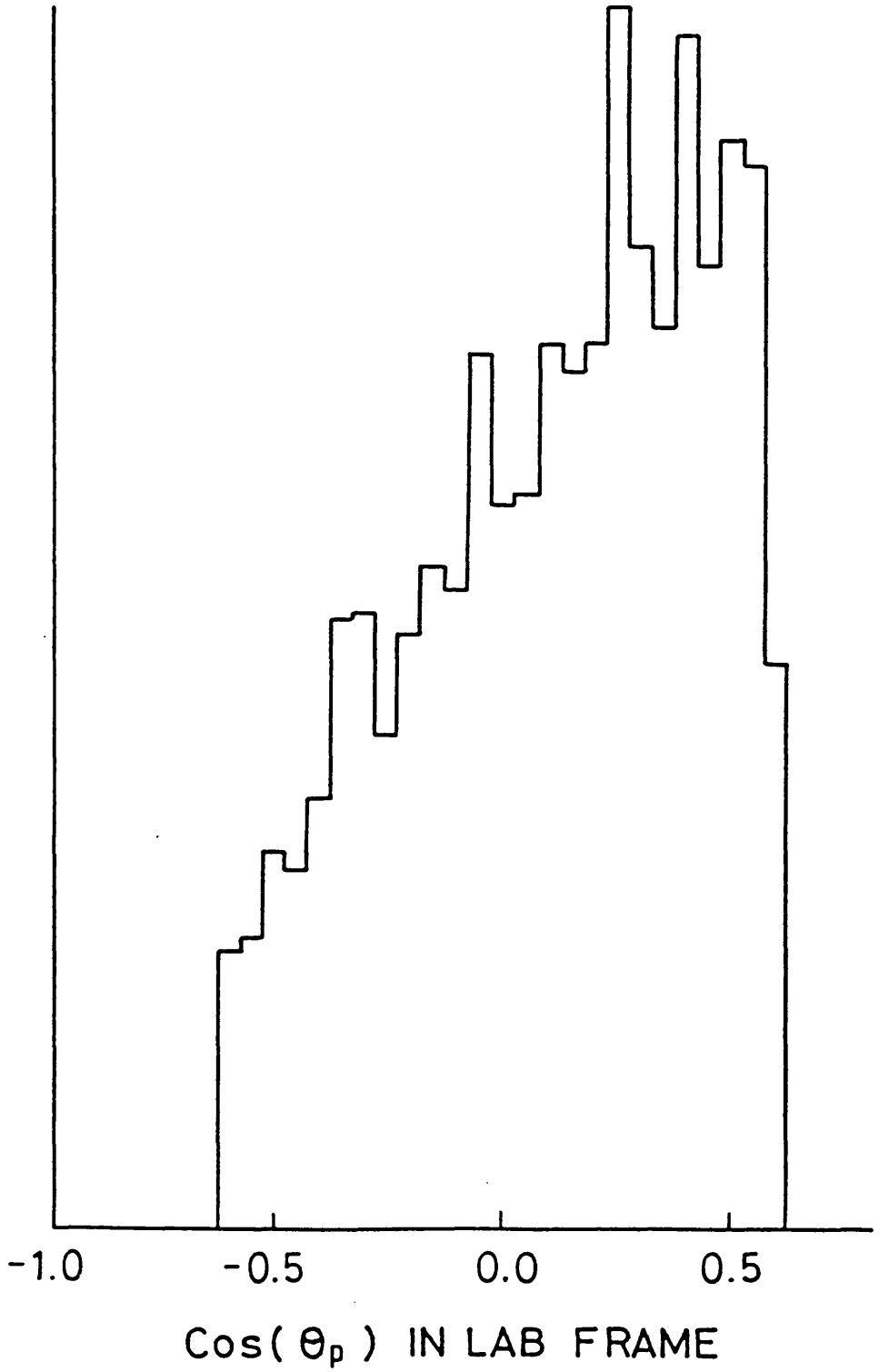

Figure 5.9: Experimental proton angle spectrum for (γ,pn)d and (γpn)pn events. Horizontal axis is the cosine of the proton angle

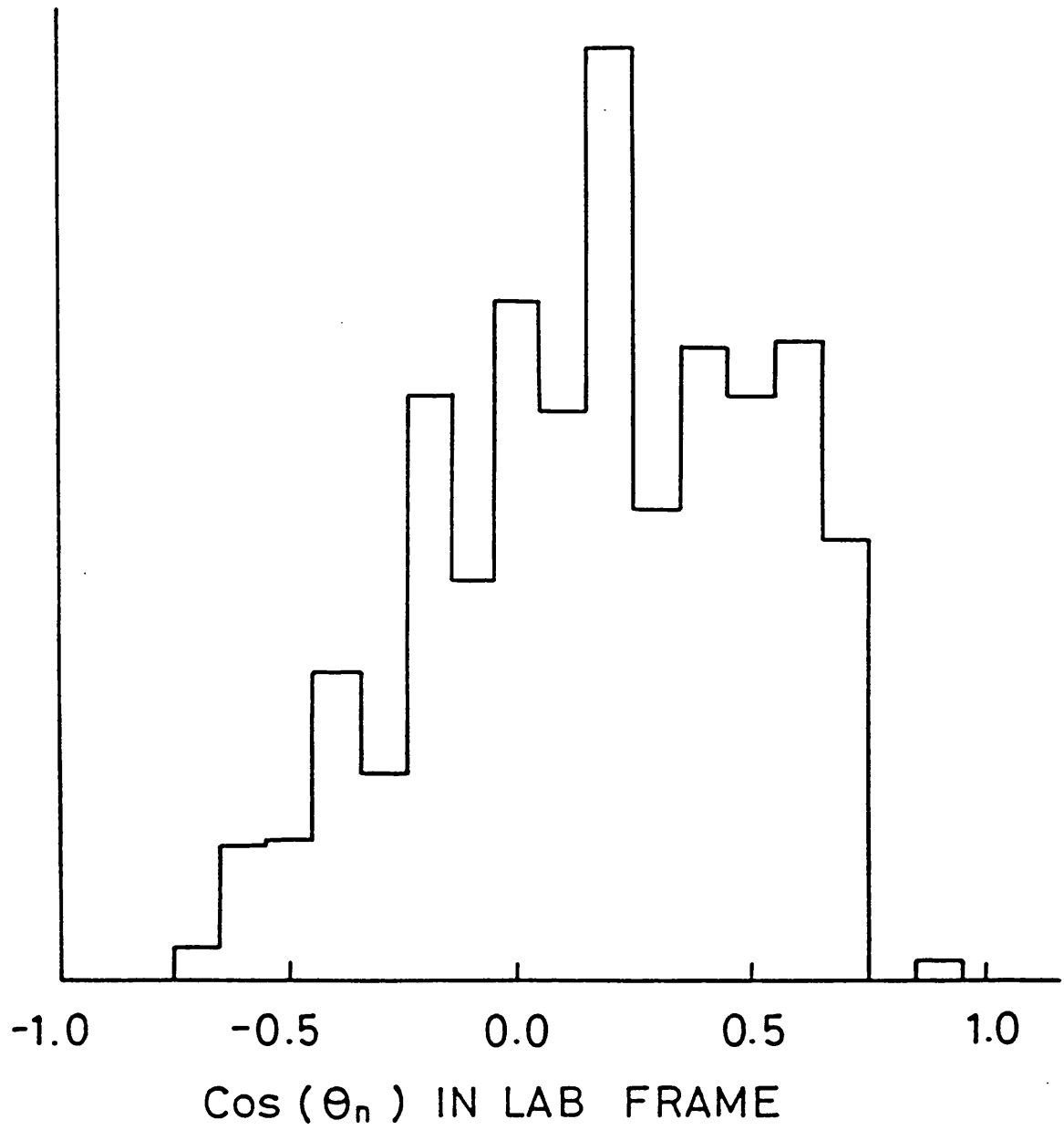

Figure 5.10: Experimental neutron angle spectrum for (γ,pn)d and (γ,pn)pn events. Horizontal axis is cosine of the neutron angle.

which the proton and the neutron leave the target in exactly opposite directions in the (γ + QD) COM frame since it is in this frame that the QD is stationary. Results for the proton QD angular distribution for ^{4}He are shown in figure 5.11. These results suggest that the observed forward asymmetry in figure 5.9 is largely due to frame transformations rather than a feature of QD absorption of photons. This angular distribution is now being calculated for ^{16}O [79] and the results show a strong sensitivity to the reaction mechanism. As yet there are no results for ^{4}He.

5.3 Recoil Momentum

The p-n angular correlation is often cited as qualitative evidence of a quasideuteron mechanism. However a more quantitative test is to examine the momentum distribution of the undetected recoil particle(s). If the quasideuteron hypothesis is correct, and the final state interactions of the outgoing nucleons are small, this distribution should be the same as the predicted momentum distribution of the initial nucleon pair within the nucleus which can be obtained from the nucleon wavefunctions in the initial nucleus.

5.3.1 The (γ,pn)d Recoil Momentum Distribution

Figure 5.12 shows the experimental recoil momentum distribution (thick solid line) for the ^{4}He (γ,pn)d reaction. A cut is made at 35 MeV in the missing energy spectrum to separate (γ,pn)d and (γ,pn)pn events. The experimental distribution is compared with MC predictions for three different reaction models, namely, QD, using SHO wavefunctions and variational wavefunctions, and PS predictions. The thin solid line in the diagram is the QD simple harmonic oscillator prediction, the dotted line is derived from variational wavefunctions by Schiavilla *et.al.* for 3-body

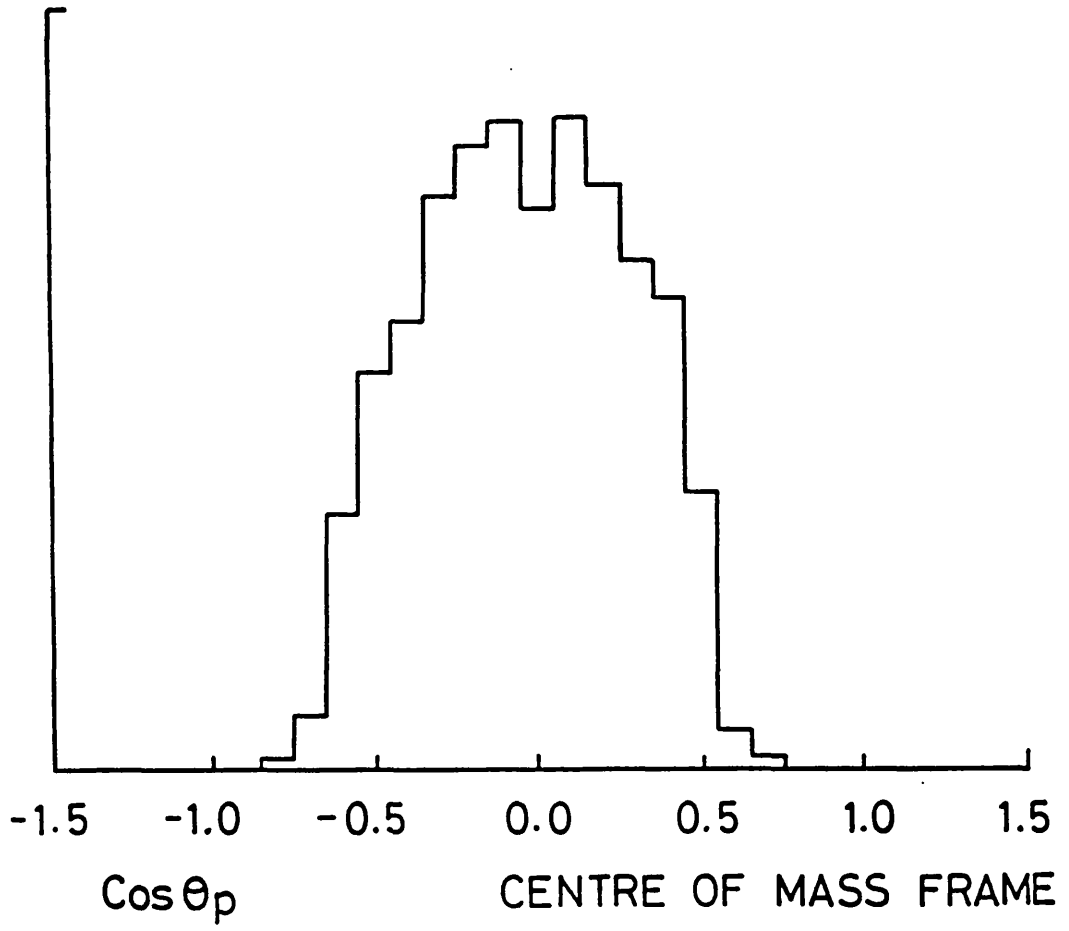

Figure 5.11: The proton angle spectrum for (γ,pn)d events in the (γ+ QD) centre-of-mass frame for the energy range 80-131 MeV. In this frame, the proton and neutron leave the nucleus in exactly opposite directions.

breakup and the dashed line is the PS prediction. The two QD predictions fit the data reasonably well, but the phase space prediction fits the data poorly.

5.3.2 The (γ,pn)pn Recoil Momentum Distribution

Figure 5.13 shows the recoil momentum distribution for 4-body breakup events, that is, events with missing energies above 35 MeV. The thick solid line is the experimental data. The thin solid line is the prediction for QD absorption using simple harmonic oscillator wavefunctions and the dotted line is the prediction for two-proton absorption, using the same wavefunctions. The dashed line is the phase space calculation. In this spectrum, absorption on a p-n pair and the phase space distribution both give acceptable fits, with the model of absorption on a p-n pair giving a slightly better description. However absorption on a p-p pair is not consistent with the data. The p-p absorption model gives a distribution which peaks at higher momentum values than the PS distribution. This is because in the former model the undetected proton receives a much larger share of the incident photon momentum. The results appear to discount significant absorption on p-p pairs, however they do not provide a clear distinction between p-n pair absorption and a phase space distribution. As with missing energy, the results are consistent with a QD mechanism but are not sensitive enough to determine which QD model gives a better fit.

5.3.3 The (γ,pp) Recoil Momentum Distribution

Figure 5.14 shows the recoil momentum distribution for the ^{4}He (γ,pp) reaction shown against the quasideuteron model with simple harmonic oscillator wavefunctions, absorption on a correlated p-p pair and a phase space distribution. All three

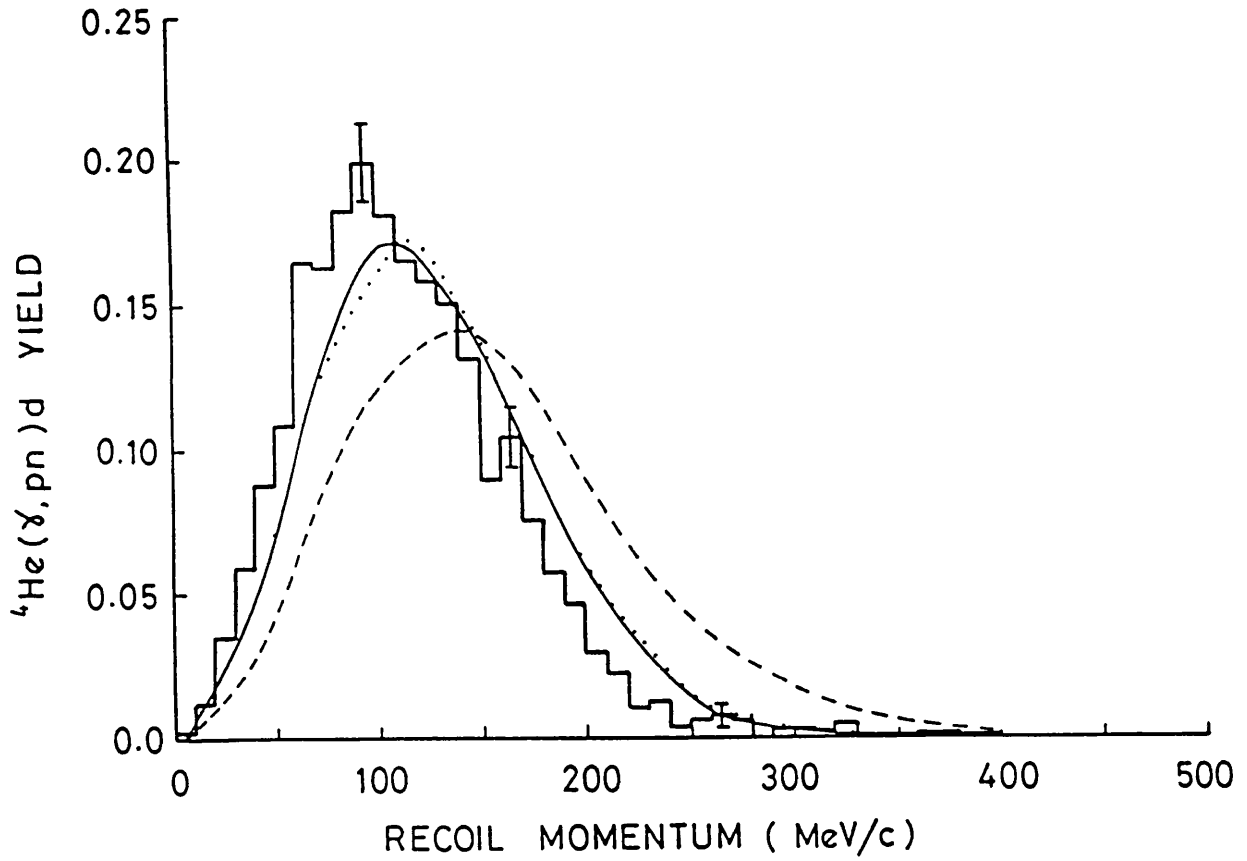

Figure 5.12: Recoil momentum spectrum for the ^{4}He(γ,pn)d reaction channel. The thick solid line is the experimental data. The thin solid line is the prediction of photon absorption on a correlated p-n pair, calculated with harmonic oscillator wavefunctions. The dotted line is the prediction of photon absorption on a correlated p-n pair, calculated with variational wavefunctions for 3-body breakup. The dashed line is the phase space prediction.

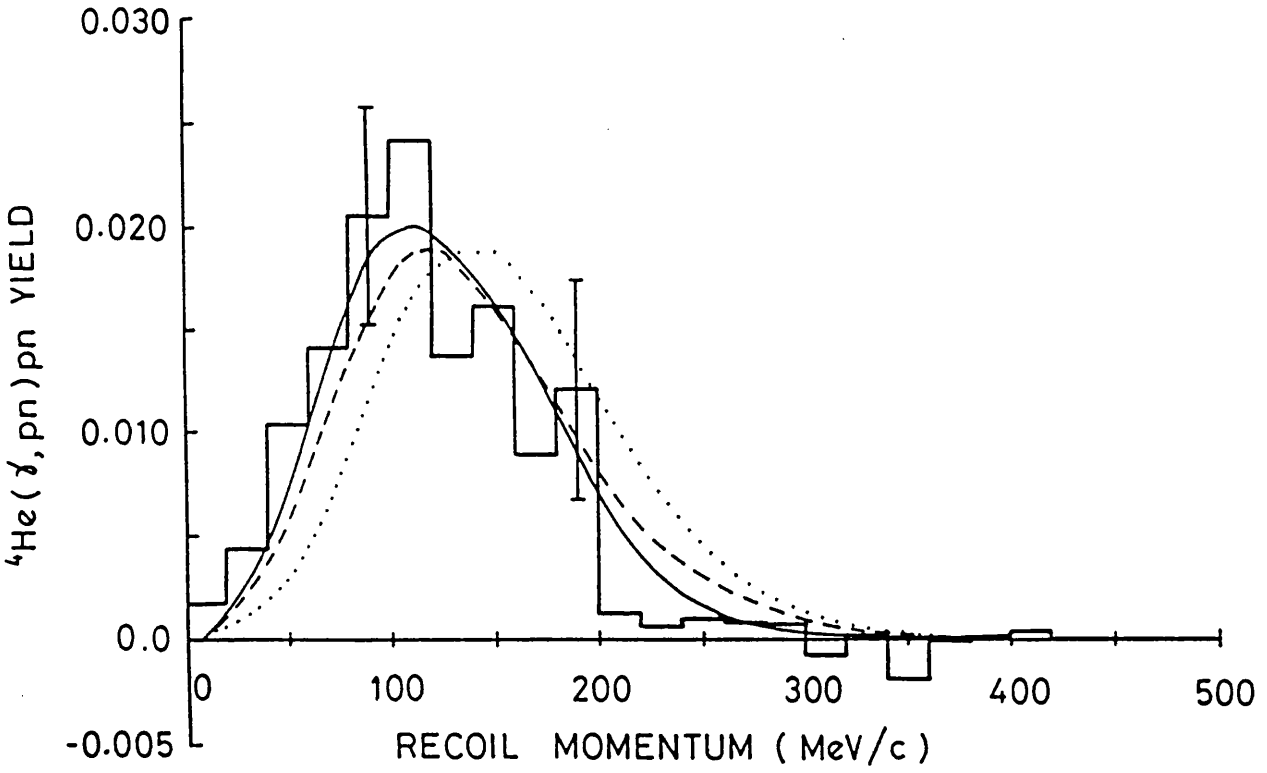

Figure 5.13: Recoil momentum spectrum for the ^{4}He(γ,pn)pn reaction channel. The thick solid line is the experimental data. The thin solid line is the prediction of photon absorption on a correlated p-n pair, calculated with harmonic oscillator wavefunctions. The dotted line is the prediction of photon absorption on a correlated p-p pair with harmonic oscillator wavefunctions. The dashed line is the phase space prediction.

models give a reasonable description of the data. This is due to the very strong suppression of the high recoil momentum events by detector threshold effects. These are larger for (γ,pp) than for (γ,pn) reactions because the protons suffer energy losses in the air and have a higher effective threshold in the TOF detectors. This spectrum does not therefore help to distinguish the reaction mechanism in the 4-body breakup channel.

5.4 Cross-sections

The extraction of total cross-sections for the 3- and 4-body breakup modes required an evaluation of the overall detection efficiencies from the Monte Carlo simulations. However because of the nature of the Monte Carlo simulations, the correction factors applied to obtain the cross-sections were necessarily model dependent.

The data from the 3-body breakup were sufficiently extensive to allow an evaluation of reaction cross-sections for 3 photon energy bins. Figure 5.15 [80] shows the total cross-section for the ^{4}He (γ,pn)d reaction as a function of photon energy assuming a quasideuteron mechanism compared with other data by Gorbunov *et.al.* [40, 41, 81] Arkatov *et.al.* [43, 82] and Balestra *et.al.* [45, 44].

The magnitudes of these cross-sections agree with earlier work for the same energy region, however the present measurement indicates a rising trend with increasing photon energy. This trend is not reflected in previous work, however this could be due to difficulties in previous experiments in distinguishing between 3-body and 4-body breakup. The results obtained using a phase space model are unrealistically high, giving values greatly in excess of any previous measurement. This is further confirmation that the ^{4}He (γ,pn)d reaction proceeds mainly by photon absorption on correlated p-n pairs. The results for the ^{4}He cross-sections are shown

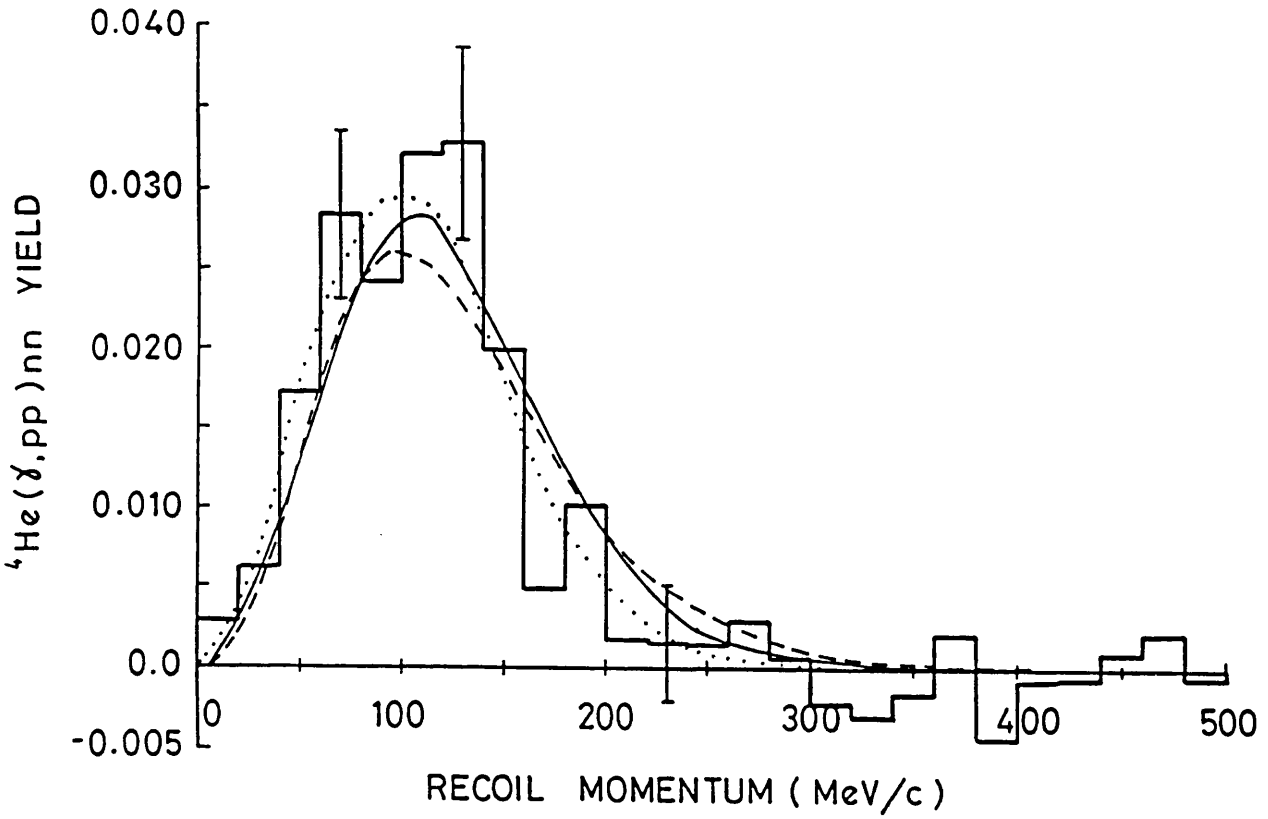

Figure 5.14: Recoil momentum spectrum for the ^{4}He (γ,pp) reaction channel. The thick solid line is the experimental data. The thin solid line is the prediction of photon absorption on a correlated p-n pair, calculated with harmonic oscillator wavefunctions. The dotted line is the prediction of photon absorption on a correlated p-p pair. The dashed line is the phase space prediction.

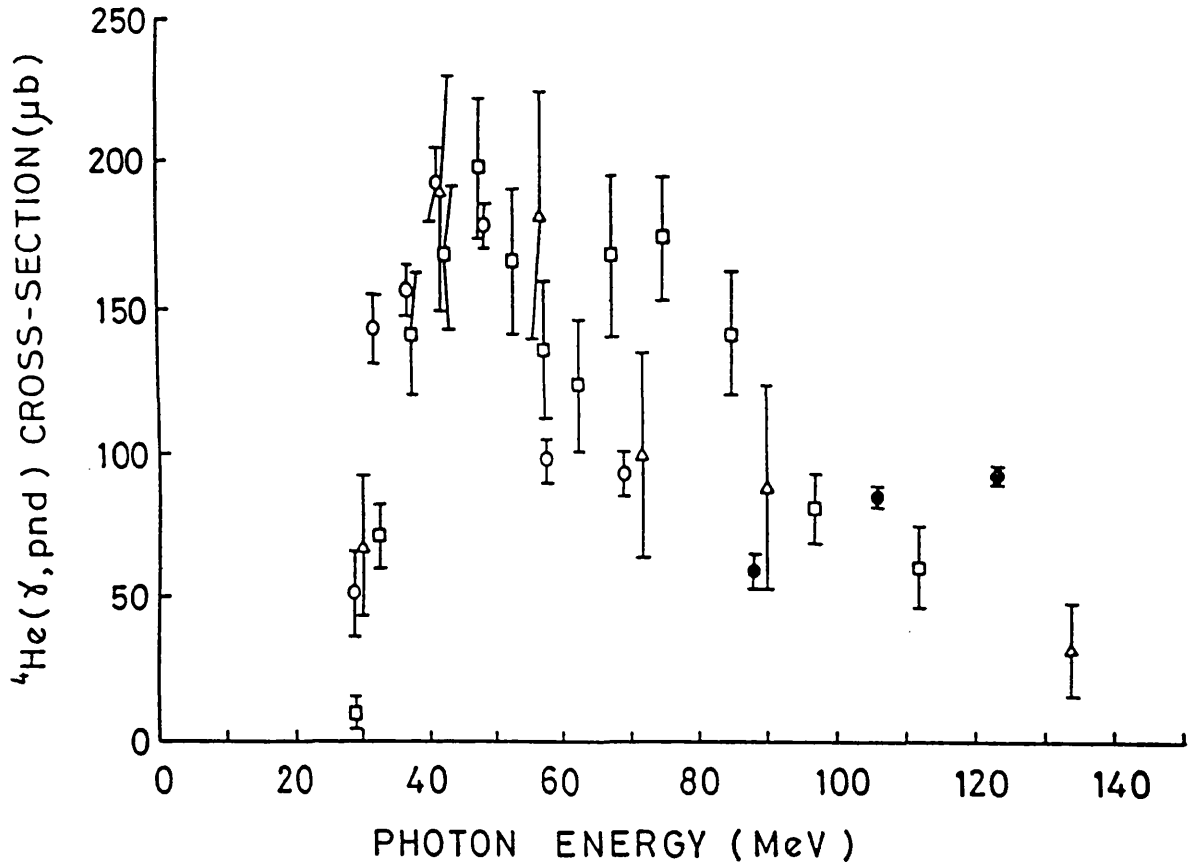

Figure 5.15: The measured total cross-section, derived using the QD model (solid circles), shown against the results from Gorbonov *et.al.* (triangles), Arkatov *et.al.* (squares) and Balestra *et.al.* (open circles). the error bars represent only statistical errors.

Photon energy range (MeV)	Photon absorption on a proton-neutron pair (μb)	Phase space distribution (μb)
80-97	58.6±6.0	228.5±16.3
97-115	84.6±3.4	368.0±14.6
115-131	91.9±3.0	441.6±14.3

Table 5.1: Photonuclear cross-sections for the (γ,pn)d reaction. The errors are statistical only

Quantity	Systematic error (%)
detector efficiencies	10.0
detector thresholds	8.5
tagging efficiency	2.9
target thickness	1.9
tagger multiplicity	0.9
TOF multiplexing correction	0.9
deadtime correction	0.2
total added in quadrature	13.6

Table 5.2: Systematic errors in the experiment.

in table 5.1 for both the quasideuteron and phase space model assumptions. The systematic errors are not included in the graph, but are listed in table 5.2 showing that the main sources of error are the result of detector effects.

For the 4-body breakup channel the average cross-section assuming quasideuteron absorption is 17±5 μb over the photon energy range 80-131 MeV. If absorption on a p-p pair is assumed, where one of the recoil neutrons is detected, this gives a cross-section of 30±9 μb, although significant p-p absorption is unlikely in view of the missing energy and recoil momentum results. The result assuming a phase space distribution is 42±12 μb. The errors are necessarily much larger than for 3-body breakup due to poorer statistics and due to the subtraction method used to obtain the 4-body yields.

The cross-section of deuterium for the (γ,pn) reaction averaged over the photon energy range $E_\gamma = 80 - 131$ MeV is 68.7μb. For ^{4}He the relation

$$\sigma_{QD} = L\frac{NZ}{A}\sigma_D \tag{5.2}$$

simplifies to

$$\sigma_{QD} = L\sigma_D \tag{5.3}$$

Since the overall ^{4}He (γ,pn)d cross-section was 84.6±3.4 in the energy range 97-115 MeV this gives a value for the Levinger parameter L of 1.23±0.05 for this channel.

If the (γ,pn)d and (γ,pn)pn channels are taken together this gives a Levinger parameter of ~1.5-1.7 depending on which mechanism is assumed for the (γ,pn)pn reactions. The present measurement gives lower values for L than the ^{4}He measurements of Homma *et.al.* [83] and the early measurements of Barton and Smith who respectively obtained 4.5±0.7 and 4.2 for the total cross-section for the energy ranges 150-280 MeV and 190-430 MeV respectively. However the data of Homma *et.al.* was taken in a much higher energy region where there is evidence that the QD mechanism at least in the 4-body breakup channel no longer dominates the cross-section. Recent results on other light nuclei such as ^{12}C (L = 3.78±0.23) [19] and ^{16}O (L = 3.3±0.6) [21] have also yielded relatively low values for L. This especially low value for ^{4}He is particularly surprising since ^{4}He has a markedly higher density than other nuclei, which would be expected to enhance the (γ,pn) cross-section.

The 4-body cross-section can also be obtained from the ^{4}He (γ,pp) reaction and this cross-section was evaluated in a similar way to the (γ,pn)pn cross-section. If absorption on a correlated p-n pair is assumed an average cross-section of 36±3 μb, over the photon energy range 80 - 131 MeV is obtained, whereas the phase-space distribution gives a value of 29±2 μb. The higher value from the p-n pair absorption mechanism is understandable as the spectator proton always has a very

low energy and consequently a low detection probability. It will be noted that the 4-body breakup cross-section obtained for the ^{4}He (γ,pp) data are inconsistent with those obtained from the ^{4}He (γ,pn) measurement. One possible explanation is that the 4-body breakup channel proceeds by two mechanisms, partly by absorption on a p-n pair and partly by a more complicated mechanism for which a phase space description of the final state is more appropriate. A cross-section of 7.5$\pm$7.5 μb for absorption on a correlated p-n pair together with a phase space cross-section of 22.5$\mp$7.5 μb would give the correct measured yields for both the (γ,pn) and (γ,pp) reactions. The total cross-section obtained in this way is 30$\pm$3 μb. In this interpretation the phase space contribution dominates that of the pair absorption mechanism. There is existing experimental evidence [47] that the 4-body breakup cross-section at higher photon energies is not due entirely to absorption on correlated p-n pairs but possibly may have a significant contribution from absorption on p-p pairs or on 3-N clusters. The present results provide some evidence for the importance of other mechanisms but in general the results would tend to discount absorption on p-p pairs. The 4-body breakup cross-section value of 30 μb obtained by adding the phase space and pair absorption contributions is compared with previous measurements [40, 41, 43, 44, 45, 46, 47, 80, 82] in figure 5.16. The previous measurements of Gorbunov and Arkatov *et.al.* are not consistent. The present result lies well within the range defined by these previous measurements. It is also reasonably consistent with the upper limit of 26 μb obtained in reference [47] at the higher energy of 155 MeV, given the large error at this point. Taken together the results clearly establish a dip in the cross-section at around 100-200 MeV.

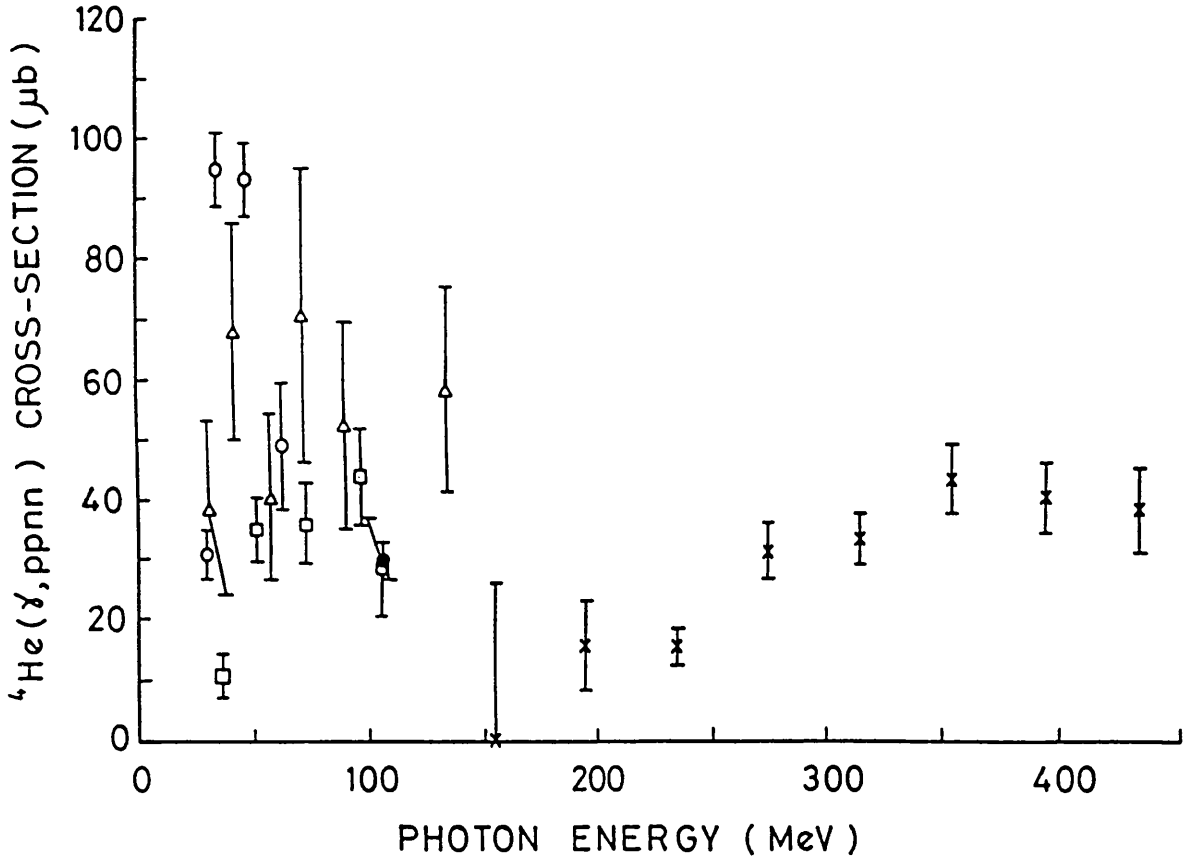

Figure 5.16: The measured ^{4}He (γ,pn)pn total cross-section, shown against the results from Gorbunov *et.al.* (triangles), Arkatov *et.al.* (squares), Balestra *et.al.* (circles) and Emura *et.al.* (crosses).

5.5 Comparisons with Other Nuclei

Figure 5.17 shows (γ,pn) spectra [21] for ^{16}O and ^{12}C for comparison with the ^{4}He results. Both spectra were obtained using the same photon energy range over which ^{4}He data was taken. The ^{16}O (γ,pn) missing energy spectrum in figure 5.17(a) has a broad peak corresponding to low energy excitation of the residual nucleus with a smaller contribution for higher energy excitations, similar to the ^{4}He missing energy spectrum. A similar pattern is also observed for the ^{12}C (γ,pN) spectrum in figure 5.17(b). As with the ^{4}He missing energy spectra the detector acceptances bias the data through suppression of the high missing energy part of the spectrum where the proton and neutron energies are only marginally above the detection thresholds. The ^{12}C case mirrors the ^{4}He missing energy spectrum insofar as a narrow peak of width $\sim$7 MeV is observed at lower missing energies. This suggests a dominant reaction channel for ^{12}C, corresponding in energy to the ejection of correlated p-n pairs, with the residual nucleus left in the ground state. However unlike ^{4}He there is a significant contribution from higher excitations such as 1p1s and 1s1s p-n pairs being ejected. The ^{16}O case also shows more strength from higher excitations than ^{4}He, however this may be due in part to the larger numbers of available final states in the ^{16}O and ^{12}C cases.

Figure 5.18 [20] shows an excitation energy spectrum for ^{6}Li taken at the higher energy range 131-157 MeV. The horizontal axis is equal to the missing energy minus 3.7 MeV, which is the binding energy of the 1p1p p-n pair. This shows significant contributions from 1p1p p-n emission but also from 1p1s and 1s1s excitations which involve disintegration of the tightly bound α-core. The 1s1s channel is analogous to the breakup of ^{4}He, hence the data are expected to show some similarities to the photodisintegration of ^{4}He. A missing momentum spectrum is shown in figure

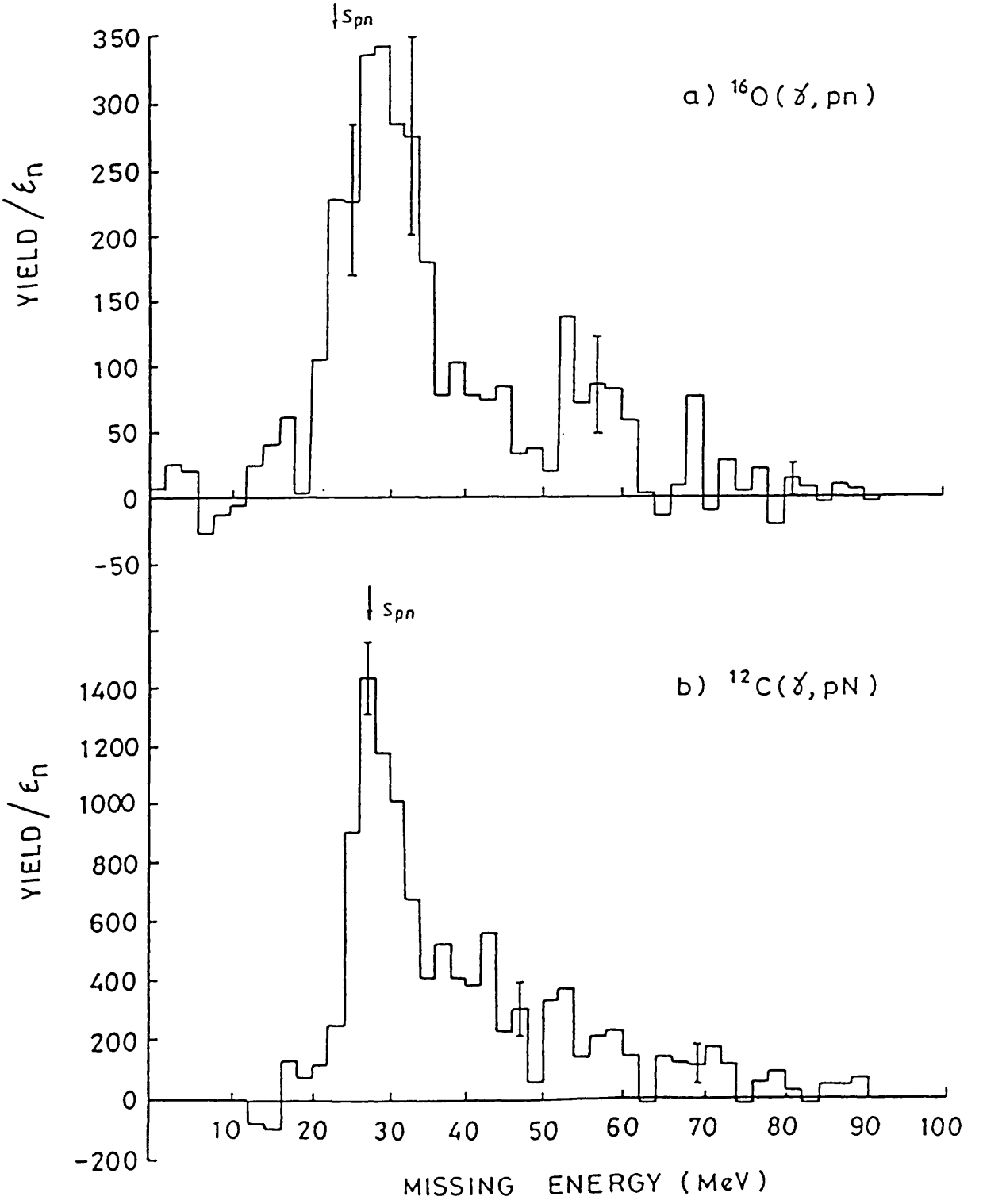

Figure 5.17: (γ,pn) missing energy spectra for ^{12}C and ^{16}O. The solid line represents experimental data. Monte Carlo predictions calculated using a quasideuteron mechanism (dashed line) and a phase space distribution in the final state (dotted line) are also shown.

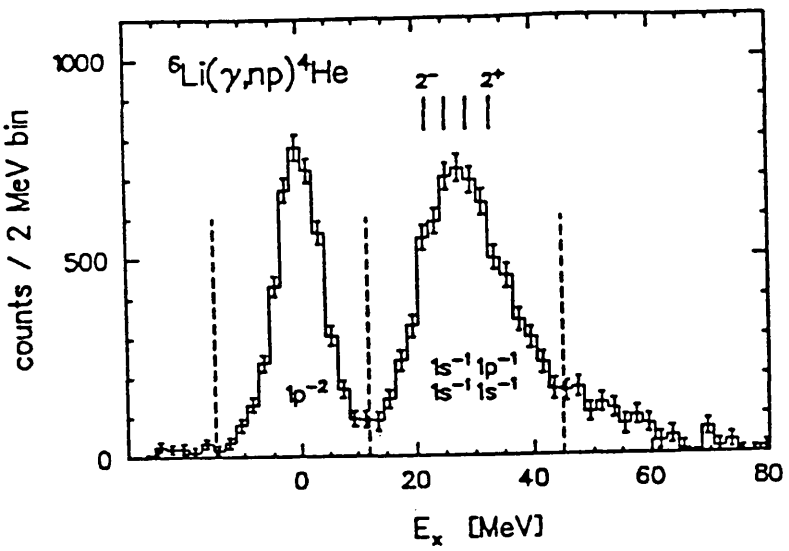

Figure 5.18: The excitation energy distribution for ^{6}Li measured in the range 131-157 MeV

5.19 for the events corresponding to breakup of the α-core. Monte Carlo predictions for the 1p1s and 1s1s channels are shown, which give a good fit to the data. The calculations use a harmonic oscillator parameter $\beta = 0.257$ fm^{-2}, which is smaller than the value $\beta = 0.385$ fm^{-2} appropriate for ^{4}He, and reflects the larger size of the ^{6}Li nucleus. The proportion of 1p1s interactions was taken to be 0.5 of the 1s1s interactions. It is seen that in the photodisintegration of the ^{6}Li α-core the QD model is reasonably successful and that the reaction is dominated by absorption on 1s1s p-n pairs.

The (γ,pn) recoil momentum distribution is shown for ^{16}O in figure 5.20 [21] for events up to 43 MeV missing energy. This spectrum was obtained using the same apparatus and photon energy range as for the ^{4}He data. Also shown on this graph are Monte Carlo predictions based on the quasideuteron model and on a phase space distribution. The quasideuteron model clearly fits the data better than the phase space model, giving further evidence for the dominance of the quasideuteron

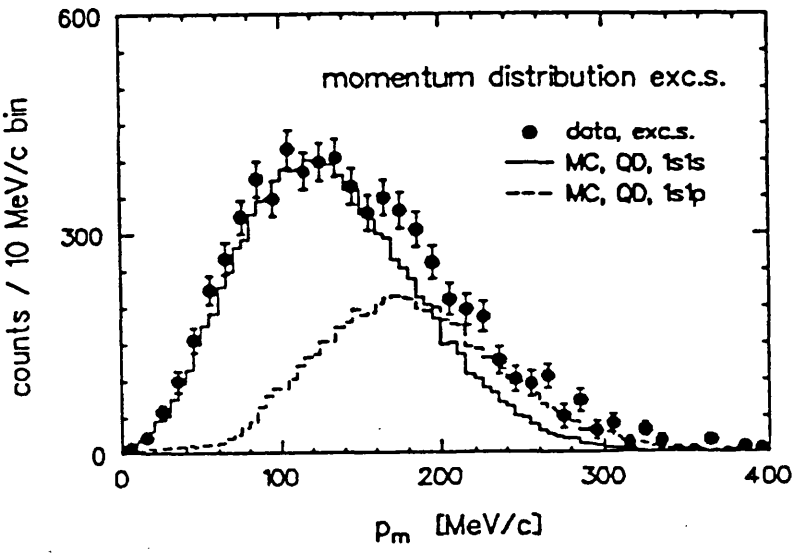

Figure 5.19: The missing momentum distribution for the 1p1s and 1s1s excitations in ^{6}Li measured in the range 131-157 MeV

mechanism in light nuclei at least for low excitations.

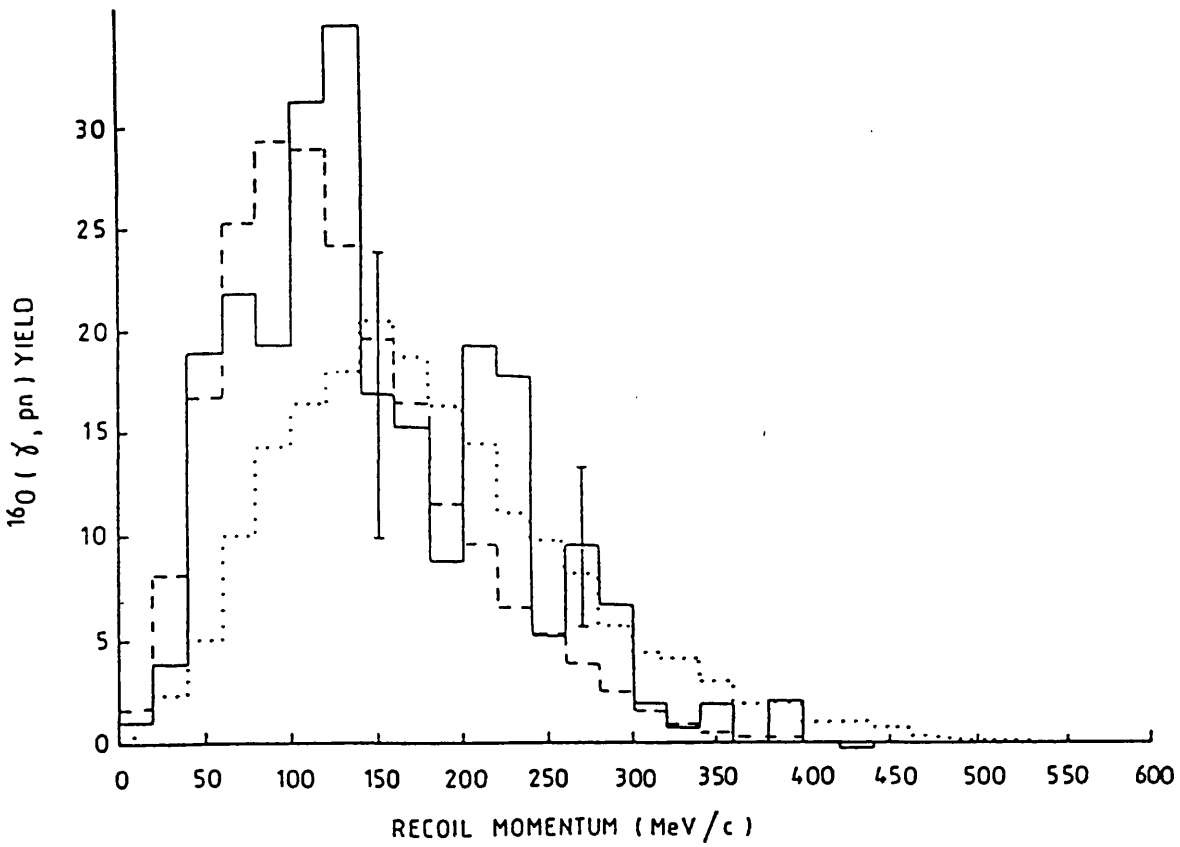

Figure 5.20: The recoil momentum distribution for ^{16}O. The experimental data are shown (solid line) together with Monte Carlo predictions calculated using a quasideuteron mechanism (dashed line) and for a phase space distribution in the final state (dotted line).

do, however, eliminate the possibility of a significant contribution from absorption of photons by correlated p-p pairs.

Consistency between the cross-sections from the (γ,pn)pn and (γ,pp)nn data is obtained if the total cross-section of 30 μb is 75% from a mechanism resulting in a phase space distribution in the final state and 25% from absorption on p-n pairs.

There is a clear need to study these reactions in greater detail, and particularly at higher photon energies. At higher energies, the effects of detector acceptances will be much smaller, allowing greater experimental precision to be obtained. The development of new detection systems for use at the new 855 MeV microtron facility [84, 85] at Mainz should allow a better understanding of the nature of photonuclear reactions at higher missing energies and will extend the data to higher photon energies where Δ-excitation processes begin to contribute to the photonuclear cross-section. In addition, the high beam energy will allow exploration of the photonuclear cross-section over a much broader photon energy range than was possible with the previous facility at Mainz.

It is important for the eventual detailed understanding of the photon absorption mechanism in ^{4}He that a microscopic calculation of the photon reaction channels can be carried out. No such calculation of (γ,NN) reactions has yet been attempted for nuclei of $A > 3$, and the quasideuteron model may be less soundly based for ^{4}He than for heavier nuclei. In particular, the assumption that the residual momentum distributions of the two spectator nucleons are the same as their average distribution in the ^{4}He ground state is brought into question since the selection of a closely spaced p-n pair may effectively select an atypical part of the initial ground state wavefunction.

However, this work has established that in ^{4}He, the quasideuteron model gives

a reasonable fit to the data in the (γ,pn)d reaction channel, and due to the excellent energy resolution available, has provided more accurate cross-sections for the (γ,pn)d and (γ,pn)pn channels than have been possible until now.

Appendix A

Missing Energy Calculations

Two forms of missing energy were calculated in the course of this analysis, one applicable to the case where only one reaction product was observed, which will be called the single-arm missing energy, discussed in section A.1. The other is for the case where two particles were detected, called the double-arm missing energy, and this is discussed in section A.2. The single-arm missing energy was used for detector calibration, and the double-arm missing energy was used for reaction identification. The double-arm missing energy reveals information about the target nucleus as will be seen in section A.2.1.

A.1 The Single-arm Missing Energy, (γ,p)

The primary motivation for evaluating the (γ,p) missing energy for this analysis was to calibrate the E blocks of the ΔE,ΔE,E array.

The single-arm (γ,p) missing energy is defined by

$$E_m = E_\gamma - T_p - T_R \tag{A.1}$$

where E_γ is the photon energy and T_p the energy of the detected proton. T_R is

the difference between the total energy E_R of the recoiling system and its Lorenz-invariant mass m_R.

i.e.

$$T_R = E_R - m_R = E_R - \sqrt{E_R^2 - \boldsymbol{p}_R^2}$$

where by considering energy and momentum,

$$E_R = E_\gamma + m_\alpha - T_p - m_p \tag{A.2}$$

and

$$\boldsymbol{p}_R = \boldsymbol{\omega}_\gamma - \boldsymbol{p}_p \tag{A.3}$$

- 2-body breakup:- If the reaction is ^{4}He(γ,p)t (where t is a triton ^{3}H), then T_R is the kinetic energy of the recoiling triton, and m_R its rest mass.

  By conservation of energy,

  $$E_\gamma + m_\alpha = m_p + m_t + T_p + T_t \tag{A.4}$$

  thus, using A.1, where $T_R = T_t$,

  $$E_m = m_p + m_t - m_\alpha = 19.815 \text{ MeV} \tag{A.5}$$

- 3- and 4- body breakup

  If the recoiling system is not a bound triton, its invariant mass will be greater, i.e. $m_R > m_t$. In fact the minimum possible value of m_R will occur when $m_R = m_n + m_d$, corresponding to the (γ,pnd) reaction, therefore $m_R \geq m_n + m_t$, and by conservation of energy,

  $$E_\gamma + m_\alpha = m_p + m_R + T_p + T_R \tag{A.6}$$

therefore

$$E_m = m_p + m_R - m_\alpha \tag{A.7}$$

therefore

$$E_m \geq m_p + m_n + m_d - m_\alpha \tag{A.8}$$

or

$$E_m \geq 26.1 \text{ MeV} \tag{A.9}$$

A spectrum of E_m will produce a distinct peak corresponding to $m_R = m_t$ and a broad distribution of events for $m_R \geq m_n + m_d$.

This measurement was studied in detail in reference [13] but for the present work was used only for calibration purposes. Since its measurement requires the detection of just the proton and a tagged photon signal, a large number of events can be obtained for only a small part of the data. The $m_R = m_t$ peak can therefore provide a good calibration of the proton detector.

The $\Delta E, \Delta E, E$ array was first calibrated using the D(γ,p)n reaction to obtain an approximate dependence of scintillator detector response with proton energy. The ^{4}He(γ,p)t reaction was used to make small adjustments to this to take account of drifts in the PMT response. The missing energy spectrum for ^{4}He was measured for each of the relevant data files and the calibration parameters were adjusted until a sharp peak at $E_m \approx 19.815$ MeV was obtained.

It is the value of T_p that is measured by the $\Delta E, \Delta E, E$ array once it has been calibrated. It can be shown that T_p can be calculated for the two body peak from the proton angle and photon energy alone. This is done as follows...

By conservation of momentum and energy,

$$\omega = \mathbf{p}_p + \mathbf{p}_t \tag{A.10}$$

and

$$\omega + m_\alpha = E_p + E_t \tag{A.11}$$

thus

$$m_t^2 = E_t^2 - \boldsymbol{p}_t^2 \tag{A.12}$$

$$m_t^2 = (\omega + m_\alpha - E_p)^2 - \left(\omega - \boldsymbol{p}_p\right)^2 \tag{A.13}$$

$$m_t^2 = (\omega + m_\alpha)^2 - 2E_p(\omega + m_\alpha) + m_p^2 - \omega^2 - 2\omega \mid \boldsymbol{p}_p \mid \cos\theta \tag{A.14}$$

or

$$f + gE_p + h \mid \boldsymbol{p}_p \mid = 0 \tag{A.15}$$

where

$$f = (\omega + m_\alpha)^2 + m_p^2 - \omega^2 - m_t^2 \tag{A.16}$$

and

$$g = 2(\omega + m_\alpha) \tag{A.17}$$

and

$$h = -2\omega \cos\theta \tag{A.18}$$

writing $Ep = \sqrt{m_p^2 + \mathbf{p}_p^2}$ it follows that

$$(g^2 - h^2)p_p^2 - 2fhp_p + \left(g^2 m_p^2 - f^2\right) = 0 \tag{A.19}$$

leading to

$$p_p = \frac{fh + g\sqrt{h^2 m_p^2 + f^2 - g^2 m_p^2}}{g^2 - h^2} \tag{A.20}$$

and

$$T_p = -m_p + \sqrt{m_p^2 + \mathbf{p}_p^2} \tag{A.21}$$

Note that there is only one solution to equation A.19 since the other root is non-physical.

A.2 The Double-arm Missing Energy

If a photon of momentum $\mathbf{p}_\gamma$ interacts with an ^{4}He nucleus to produce a proton and a neutron, which are both detected, then the momentum $\mathbf{p}_R$ of the recoiling system is given by

$$\mathbf{p}_R = \mathbf{p}_\gamma - \mathbf{p}_p - \mathbf{p}_n \tag{A.22}$$

where $\mathbf{p}_p$ and $\mathbf{p}_n$ are the momenta of the detected proton and neutron respectively. The total energy E_R of the recoiling system is calculated from

$$E_R = E_\gamma + m_\alpha - T_p - m_p - T_n - m_n \tag{A.23}$$

where m_α is the α-particle rest mass, m_p and m_n are the proton and neutron rest masses and T_p and T_n their kinetic energies. The Lorenz-invariant mass of the recoiling system is

$$m_R = \sqrt{E_R^2 - \mathbf{p}_R^2} \tag{A.24}$$

the quantity T_R is defined by

$$T_R = E_R - m_R \tag{A.25}$$

The double-arm (γ,pn) missing energy is defined in an analogous way to the single-arm missing energy of equation A.1, by

$$E_m = E_\gamma - T_p - T_n - T_R \tag{A.26}$$

or equivalently,

$$E_m = m_p + m_n + m_R - m_\alpha \tag{A.27}$$

The (γ,pn)d Channel

In the case of the 3-body breakup, (γ,pn)d,

$$E_R = T_d + m_d \tag{A.28}$$

where T_d is the deuteron kinetic energy and m_d its rest mass. From equations A.23, A.26 and A.28, one gets

$$E_m = m_p + m_n + m_d - m_\alpha = 26.1\text{MeV} \tag{A.29}$$

The (γ,pn)pn Channel

In the case of the (γ,pn)pn reaction, the Lorenz-invariant mass m_R of the recoil system is at least the sum of the rest mass energies of its components,

i.e.

$$m_R \geq m_p + m_n \tag{A.30}$$

so that from A.23, A.25 and A.26 one obtains

$$E_m \geq 2m_p + 2m_n - m_\alpha = 28.3\text{MeV} \tag{A.31}$$

The maximum missing energy occurs when T_p and T_n are minimal. Suppose then that

$$T_p = T_n = 0 \tag{A.32}$$

using equations A.22, A.23, A.26 and A.27,

$$E_m = \sqrt{(E_\gamma + \epsilon - T_p - T_n)^2 - (\mathbf{p}_\gamma - \mathbf{p}_p - \mathbf{p}_n)^2} - \epsilon \tag{A.33}$$

where

$$\epsilon = m_\alpha - m_p - m_n \tag{A.34}$$

Therefore the maximum theoretical value of missing energy is

$$E_m^{max} = \sqrt{(E_\gamma + \epsilon)^2 - (\mathbf{p}_\gamma - \mathbf{0})^2} - \epsilon = \sqrt{2\epsilon E_\gamma + \epsilon^2} - \epsilon \tag{A.35}$$

Measurement of Missing Energy

The missing energy is calculated from the experimental data using equation A.33 which expresses the missing energy in terms of observable parameters, where T_p and $\mathbf{p}_p$ are derived from the ADC signals in the ΔE,ΔE,E array, T_n and $\mathbf{p}_n$ are calculated from the flight-time of the other detected particle using the TOF array and $\mathbf{p}_\gamma$ is the photon momentum.

The missing energy reveals the Lorenz-invariant mass of the recoiling system, and therefore indicates whether this is a bound deuteron or a free p-n pair.

A.2.1 The Quasideuteron Model Prediction for Missing Energy

The missing energy spectrum for (γ,pn) events consists of a peak for (γ,pn)d events and a distribution of (γ,pn)pn events. If the fraction of (γ,pn) events which undergo 4-body breakup is β, then the missing energy distribution may be represented by

$$\Omega(E_m) = (1-\beta)\delta(E_m - Q_3) + \beta\mu(E_m - Q_4) \tag{A.36}$$

where $Q_3 = m_p + m_n + m_d - m_\alpha$ and $Q_4 = 2m_p + 2m_n - m_\alpha$ and where δ is the Dirac delta function. In practice it is smeared by the experimental resolution. The function μ is related to the energy available to the two undetected particles in their COM frame. It will be shown that μ can be derived from the quasideuteron momentum distribution.

The (γ,pn)pn channel will produce a theoretical distribution of missing energies ranging from $(2m_p + 2m_n - m_\alpha)$, or 28.3 MeV up to $\sqrt{2E_\gamma\epsilon + \epsilon^2} - \epsilon$, where ϵ is given in equation A.34. However the highest observed missing energies will in practice be determined by the detector thresholds. The response function of the detection system will be correlated with E_m, and will be highest for low missing energies and zero for the highest missing energies. The experimental yield for missing energy may be corrected for using a Monte Carlo correction to the data, but a truncation is necessary for the highest missing energies.

Let $\mathbf{p}_p$ and $\mathbf{p}_n$ denote the momenta of the two detected nucleons and let $\mathbf{p}'_p$ and $\mathbf{p}'_n$ denote the momenta of the other two nucleons.

Let

$$\mathbf{p}_{rec} = \mathbf{p}'_p + \mathbf{p}'_n \tag{A.37}$$

and

$$\mathbf{p}_{diff} = \mathbf{p}'_p - \mathbf{p}'_n \tag{A.38}$$

then the kinetic energy of the two recoil nucleons in their COM frame is

$$\begin{aligned} E_A &= 2\tfrac{1}{2m_N}\left(\tfrac{1}{2}p_{diff}\right)^2 \\ &= \tfrac{\mathbf{p}^2_{diff}}{4m_N} \end{aligned} \tag{A.39}$$

where m_N is the nucleon mass. Statistically, the rms value of $\mathbf{p}_{diff}$ is given by

$$\begin{aligned} \langle \mathbf{p}^2_{diff} \rangle &= \langle \left(\mathbf{p}'_p - \mathbf{p}'_n\right)^2 \rangle \\ &= \langle \left(\mathbf{p}'_p + \mathbf{p}'_n\right)^2 \rangle - 4\langle \mathbf{p}'_p \cdot \mathbf{p}'_n \rangle \\ &= \langle \mathbf{p}^2_{rec} \rangle - 4\langle \mathbf{p}'_p \cdot \mathbf{p}'_n \rangle \end{aligned} \tag{A.40}$$

The second term is zero if the momenta of the spectator nucleons are uncorrelated, thus

$$\langle p^2_{diff} \rangle = \langle p^2_{rec} \rangle \tag{A.41}$$

Thus the rms momenta are the same for any nucleon momentum distributions that are isotropic. Thus if their rms values are the same for any isotropic distribution then for a given isotropic distribution of nucleon momenta, the p_{diff} and p_{rec} distributions must be the same. Therefore the distribution of $\mathbf{p}_{diff}$ is the same as the distribution of the recoil momentum. Thus if the recoil momentum distribution is given by a function χ, where $\chi(p_{rec})\,\mathrm{d}p_{rec}$ is the probability of the recoil momentum lying between p_{rec} and $(p_{rec} + \mathrm{d}p_{rec})$ then $\chi\left(p_{diff}\right)$ is the probability of the momentum difference lying between p_{diff} and $\left(p_{diff} + \mathrm{d}p_{diff}\right)$. If $\mu(E_A)\,\mathrm{d}E_A$ is the probability that the available energy is between E_A and $(E_A + \mathrm{d}E_A)$ then

$$\mu(E_A)\,\mathrm{d}E_A = \chi(p_{diff})\,\mathrm{d}p_{diff} \tag{A.42}$$

where $E_A = \frac{p_{diff}{}^2}{4m_N}$

$$\mu\left(\frac{p^2_{diff}}{4m_N}\right)\frac{2p_{diff}}{4m_N}\mathrm{d}p_{diff} = \chi(p_{diff})\,\mathrm{d}p_{diff} \tag{A.43}$$

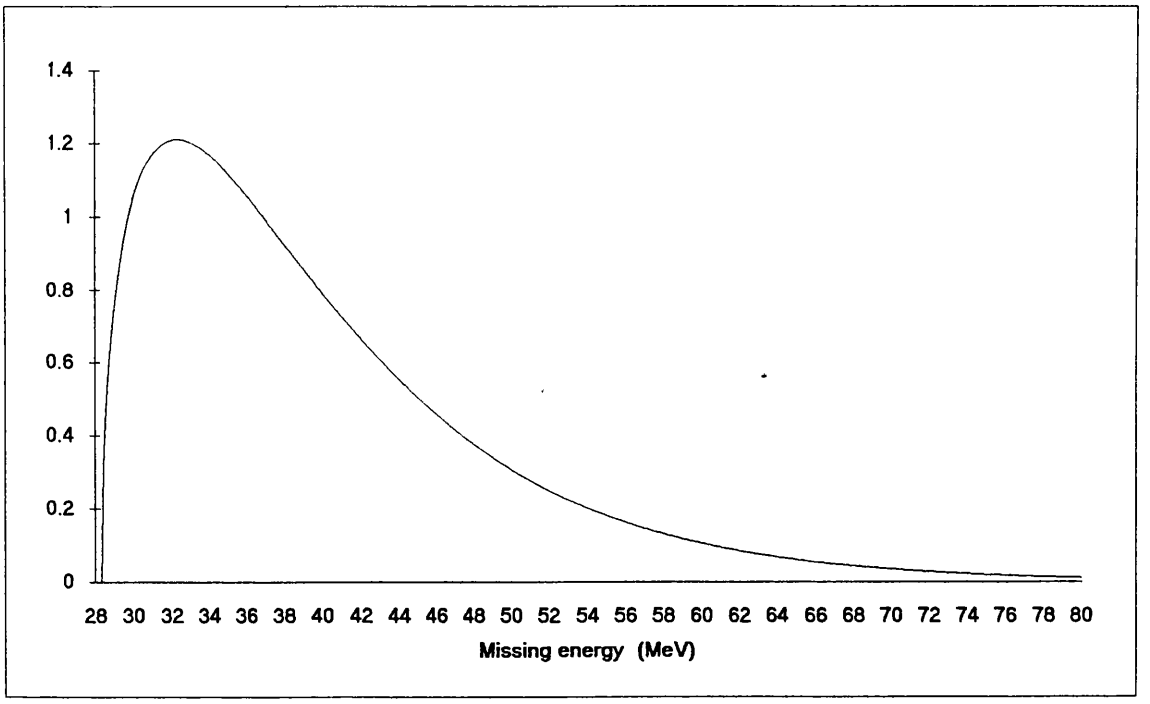

Figure A.1: Theoretical shape of 4-body part of missing energy spectrum

therefore

$$\mu\left(\frac{p_{diff}^2}{4m_N}\right)\frac{p_{diff}}{2m_N} = \chi(p_{diff}) \tag{A.44}$$

or

$$\mu(E_A) = \sqrt{m_N/E_A}.\chi\left(2\sqrt{m_N E_A}\right) \tag{A.45}$$

or

$$\mu(E_A) = 4m_N\sqrt{m_N E_A}.F\left(2\sqrt{m_N E_A}\right) \tag{A.46}$$

since $P^2F(P) = \chi(P)$, where F is the function described in section 2.2.2. Thus the missing energy distribution may be derived from the $F(P)$ distribution once the detector efficiencies have been allowed for. It must be noted, however, that because of the nature of this derivation, this may only be used to obtain the spectral shape. It is not possible to use these formula for a Monte Carlo calculation to determine the values of $\boldsymbol{p}_{rec}$ and $\boldsymbol{p}_{diff}$ for individual events.

The formula above should in theory reproduce the shape of the missing energy spectra. For example, if a simple harmonic oscillator wavefunction is used,

$$F(P) \propto e^{-P^2/2\beta} \tag{A.47}$$

then neglecting detector effects the shape of the 4-body part of the missing energy spectrum should resemble figure A.1.

Appendix B

Energy Loss Corrections

During the beam-on time, protons and deuterons are detected by both the ΔE,ΔE,E telescope and the TOF detectors. The energies of these particles are degraded through electromagnetic interactions (mostly ionisation) as they pass through the target material, the target walls, the detector scintillator and shielding, and the air in the laboratory. These losses are corrected for in the analysis.

The range R (m) of a charged particle of kinetic energy E (MeV) in a given material can be approximated by a relation of the form

$$R = c_1 E^{c_2} \tag{B.1}$$

for constants c_1 and c_2. These constants depend on the stopping material and on the mass and charge of the particle. The values of c_1 and c_2 vary slightly with E, and therefore in the data analysis, different sets of constants are used for different energy ranges. The data analysis concerns particles which lose only part of their energy, and it is necessary to determine their initial energies. If a particle of energy E_i after passing through a material of thickness P, has energy E_f, and if the particle range for the first energy is R_i, then the range for the second energy is

$R_i - P$, where

$$R_i = c_1 {E_i}^{c_2} \tag{B.2}$$

and

$$R_i - P = c_1 {E_f}^{c_2} \tag{B.3}$$

Subtracting the second equation from the first, one gets

$$P = c_1 \left(E_i^{c_2} - E_f^{c_2} \right) \tag{B.4}$$

which may be rearranged to give

$$E_i = \left(E_f^{c_2} + \frac{P}{c_1} \right)^{\frac{1}{c_2}} \tag{B.5}$$

Typical values for protons in NE102A scintillator are $c_1 \sim 0.0024 \text{g/cm}^2$, $c_2 \sim 1.78$. This equation is implemented in the computer software for the data analysis, the parameters were calculated as a function of energy from proton ranges, available in tables in reference [86].

Appendix C

Opening Angle

The relations given in this appendix are elementary. They are generally available in standard textbooks but are included here to illustrate how certain parts of the analysis are carried out.

The centre of mass (COM) opening angle between the outgoing particles is calculated in the COM frame of the photon-helium system. As the helium nucleus is stationary in the laboratory, and the photon has momentum ω, this COM frame is travelling with velocity $c\beta$ relative to the lab, where β is given by

$$\beta = \frac{\omega}{m_\alpha + \mid \omega \mid} \tag{C.1}$$

where m_α is the rest mass of the alpha particle, and c is the speed of light in vacuum. In general, if a frame is moving with velocity $c\beta$ with respect to the laboratory, and a particle has momentum $\mathbf{P}$ in the lab and velocity $\mathbf{P}'$ in this new frame, then the following transformations hold [88]:-

$$E' = \gamma(E - \beta.\mathbf{P}) \tag{C.2}$$

$$\mathbf{P}' = \mathbf{P} + \boldsymbol{\beta}\left(\frac{\gamma^2}{\gamma+1}\right)\boldsymbol{\beta}.\mathbf{P} - \gamma E\vec{\beta} \tag{C.3}$$

where γ is defined by

$$\gamma = \frac{1}{\sqrt{1-\beta^2}} \tag{C.4}$$

The opening angle, θ, is given by

$$\theta = \cos^{-1}\left(\frac{-\mathbf{P}_p.\mathbf{P}_n}{(P_p P_n)}\right) \tag{C.5}$$

Using the above set of equations, the momenta of the outgoing particles may be transformed to this new frame, and the angle between them may be evaluated event by event both in the laboratory frame and in the $(\alpha+\gamma)$ COM frame.

The above transformations were also used to put the centre of mass momenta of the particles in the Monte Carlo into the lab frame.

Bibliography

[1] J. S. LEVINGER: Physical Review **84** (1951) **43**

[2] H. HERMINGHAUS, K. KAISER AND U. LUDWIG: *Nucl. Inst. Meth.* **187** (1981) **103**

[3] J. D. KELLIE *et.al.* : *Nucl. Inst. Meth.* **A241** (1985) **153**

[4] I. J. D. MACGREGOR *et.al.* : *Nucl. Inst. Meth.* **A262** (1987) **347**

[5] J. R. M. ANNAND *et.al.* : *Nucl. Inst. Meth.* **A262** (1987) **329**

[6] S. N. YANG: J Phys G **9** (1983) L115

[7] J. M. LAGET: *J. Phys. G Nucl. Phys.* **14** (1988) **1445**

[8] H. DE VRIES *et.al.* : Atomic Data and Nuclear Data Tables **36** (1987) **495**

[9] K. GOTTFRIED: *Nucl. Phys.* **5** (1958) **557**

[10] P. D. HARTY *et.al.* : *Phys. Rev. C* , in press.

[11] J. M. LAGET: *Nucl. Phys.* **A446** (1985) **489c**

[12] J. M. LAGET: New Vistas in Electronuclear Physics (1986) ed. E Tomusiak, H Caplan and E Dressler (New York: Plenum) pp **361**

[13] H. SCHMIEDEN *et.al.* , to be published

[14] W. WEISE AND M. G. HUBER: *Nucl. Phys.* **A162** (1971) 330

[15] W. WEISE, M. G. HUBER & M. DANOS: Z. Physik **236** (1970) 176

[16] L. R. B. ELTON AND A. SWIFT: *Nucl. Phys.* **A94** (1967) 52

[17] D. FINDLAY, **PhD thesis**, UNIVERSITY OF GLASGOW, 1975

[18] L. BOATO AND M. M. GIANNINI: *J. Phys. G* Nucl. Part. Phys. **15** (1989) 1605

[19] S. N. DANCER, **PhD thesis**, University of Glasgow, 1987

[20] S. KLEIN, **PhD Thesis**, Johannes Gutenberg-Universität, 1990

[21] I. J. D. MACGREGOR *et.al.* : *Nucl. Phys.* **A533** (1991) 269

[22] G. GIUSTI *et.al.* : *Nucl. Phys.* **A546** (1992) 607

[23] J. M. LAGET: *Phys. Rev. C* **35** (1987) 832

[24] B. L. BERMAN, S. C. FULTZ AND P. F. YERGIN: *Phys. Rev. C* **10** (1974) 2221

[25] M. DÖRR, *et.al.* : *Nucl. Phys.* **A445** (1985) 557

[26] M. STEINACHER *et.al.* : *Nucl. Phys.* **A517** (1990) 413

[27] G. BACKENSTOSS *et.al.* : *Phys. Rev. Lett.* **59** (1987) 767

[28] A. C. ODIAN, P. C. STEIN, A. WATTENBERG AND B. T. FELD: Phys Rev **102** (1956) 837

[29] P. C. STEIN, A. C. ODIAN, A. WATTENBERG AND R. WEINSTEIN: *Phys. Rev* **119** (1961) 348

[30] M. Q. BARTON AND J. H. SMITH: Phys Rev **110** (1958) **1143**

[31] J. GARVEY, B. H. PATRICK, J. G. RUTHERGLEN, I. L. SMITH: *Nucl. Phys.* **70** (1965) 241

[32] I. R. VAN HISE, R. A. MAYER, J. P. HUMMEL, *Phys. Rev* **139** (1965) **B554**

[33] I. L. SMITH, J. GARVEY, J. G. RUTHERGLEN, G. R. BROOKES: *Nucl. Phys.* **B1** (1967) 483

[34] B. T. FELD, R. D. GODBOLE, A. C. ODIAN *et.al.* : PHYS REV **94** (1954) 1000

[35] J. W. WEIL AND B. D. MCDANIEL: PHYS REV **92** (1953) **391**

[36] H. MYERS, A. ODIAN, P. C. STEIN AND A. WATTENBERG: PHYS REV **95** (1954) **576**

[37] M. Q. BARTON AND J. H. SMITH: PHYS REV **95** (1953) **573**

[38] J. M. REID AND B. LALOVIC: PROCEEDINGS OF THE PHYSICAL SOCIETY, LONDON **76, 487** (1960) **65**

[39] A. N. GORBUNOV: *Sov. Journal Phys.* J.E.T.P. **34** (1958) 600

[40] A. N. GORBUNOV: *Proceedings of the P N Lebedev Phys. Inst.* **71** (1974) 1

[41] M. L. RUSTGI AND J. S. LEVINGER: *Phys. Rev* **106** (1957) 530

[42] YU A. ARKATOV *et.al.* : *Soviet Journal of Nucl. Physics.* **10** (1970) **639**

[43] F. BALESTRA *et.al.* : *Il Nuovo Cim.* **38A** (1977) **145**

[44] F. BALESTRA *et.al.* : *Il Nuovo Cim.* **49A** (1979) **575**

[45] T. EMURA *et.al.* : *Phys. Lett.* **B267** (1991) 460

[46] T. EMURA *et.al.* : *Phys. Lett.* **B286** (1992) 229

[47] J. L. FRIAR AND B. FROIS: *Lecture Notes in Physics* **260** Springer-Verlag, (1986) pp 81,
C. MARCHAND: *Lecture Notes in Physics* **260** Springer-Verlag, (1986) pp 338

[48] S. N. DANCER *et.al.* : *Phys. Rev. Lett.* **61** (1988) 1170

[49] P. D. HARTY *et.al.* : *Phys. Rev. C* **37** (1988) 13

[50] J. AHRENS: *Nucl. Phys.* **A446** (1985) 229c

[51] P. J. CARLOS: *Rapport DPh-n/SACLAY* **2476** (09/1987) *Les Fonctions de Réponse du Nucléon au Noyau Journées d'études énergies intermédiaires*

[52] M. J. LEITCH *et.al.* : *Phys. Rev. C* **31** (1985) 1633

[53] R. O. OWENS, J. L. MATTHEWS AND G. S. ADAMS: *J. Phys. G* **17** (1991) 261

[54] C. CIOFI DEGLI ATTI: 1986 *Research Program at* CEBAF, *Report of the 1985 Summer Study Group p 8-1*

[55] G. H. BERTHOLD, A. STADLER AND H. ZANKEL: *Phys. Rev. C* **41** (1990) 1365

[56] J. HEIDMANN: *Phys. Rev* **80** (1950) 171

[57] J. S. LEVINGER: *Phys. Lett.* **82B** (1979) 181

[58] O. A. P. TAVARES *et.al.* : *Il Nuovo Cim.* **27** (1980) 358

[59] A. LEPRÊTRE *et.al.* : *Nucl. Phys.* **A367** (1981) 237

[60] A. LEPRÊTRE *et.al.* : *Nucl. Phys.* **A472** (1987) 533

[61] R. JASTROW: PHYSICAL REVIEW **98** (1955) **1479**

[62] G. RICCO: *Lecture Notes in Physics* **61** Springer-Verlag, pp 223-274 (1977)

[63] M. FINK *et.al.* : *Nucl. Phys.* **A186** (1972) 353

[64] M. GARI *et.al.* : PHYS. REP. **72C** (1981) 1

[65] H. DE VRIES, C. W. DE JAGER AND C. DE VRIES: Atomic Data and Nuclear Data Tables **36** (1987) **495**

[66] R. SCHIAVILLA, V. R. PANDHARIPANDE AND R. B. WIRINGA: *Nucl. Phys.* **A449** (1986) **219**

[67] D. H. PERKINS, *Introduction to High Energy Physics,* pp 130-132, Addison-Wesley Publishing Co. Inc, 1982.

[68] N. D'HOSE *et.al.* : *Phys. Rev. Lett.* **63** (1989) **856**

[69] A. E. THORLACIUS, H. W. FEARING: *Phys. Rev. C* **33** (1986) **1830**

[70] D. DRECHSEL *et.al.* : *Phys Blätter* **46** (1990) NR. 9 **351**

[71] H. HERMINGHAUS *et.al.* : *Nucl. Inst. Meth.* **138** (1976) **1**

[72] W. E. BURCHAM: *Elements of Nuclear Physics, Longman, 1979.*

[73] C. NOGUCHI AND F. PRATS: *Phys. Rev. Lett.* **33** (1974) **1168**

[74] R. A. CECIL *et.al.* : *Nucl. Inst. Meth.* **161** (1979) **439**

[75] D. F. MEASDAY AND C. RICHARD-SERRE, Loss of Protons by Nuclear Reactions in Various Materials, CERN - Report 69-17 (1969) 1

[76] R. O. OWENS: *Nucl. Inst. Meth.* **A288** (1990) 574

[77] H. SCHMIEDEN: Institut Für Kernphysik, Johannes Gutenberg - Universität, D-6500 Mainz, *private communication.*

[78] J. RYCKENBUSCH *et.al.* : University of Ghent *private communication (1992)*

[79] S. M. DORAN *et.al.* : *Nucl. Phys. A* , IN PRESS.

[80] A. N. GORBUNOV *et.al.* : *Sov. Journal Nucl Phys* **10** (1969) 268

[81] YU A. ARKATOV *et.al.* : J.E.T.P. Letters **9** (1969) 278

[82] S. HOMMA: *Report, Institute for Nuclear Study* University of Tokyo, INS-REP 547, July 1985

[83] I. J. D. MACGREGOR: *Proceedings of the Workshop in Future Detectors for Photonuclear Experiments,* Edinburgh, May 1991, Ed. D Branford, pp 232

[84] P. GRABMAYR *et.al.* : *Proceedings of the Workshop on Future Detectors for Photonuclear Experiments,* Edinburgh, May 1991, Ed D Branford, pp 225

[85] J. F. JANNI: *National Technical Information Service, US Dept. Commerce* (1966) Tech. Rep. AFWL-TR-65-150

[86] T. J. GOODING AND H. G. PUGH: *Nucl. Inst. Meth.* **7** (1960) 189

[87] H. MUIRHEAD: *Special Theory Of Relativity, MacMillan* (1973) 65